

POLITECNICO DI TORINO

MASTER OF SCIENCE IN ELECTRICAL ENGINEERING

MASTER'S DEGREE THESIS



**Politecnico
di Torino**

**Preliminary Design and Simulation of
a Superconducting Synchronous
Machine for Aircraft Applications**

Supervisors:

Prof. Alberto TENCONI
Prof. Andrea CAVAGNINO
Prof. Francesco LAVIANO
Prof. Silvio VASCHETTO
Eng. Marco BIASION

Candidate:

Giacomo GALANTINI

A.Y. 2021/2022

“We don’t rise to the level of our expectations, we fall to the level of our training.”
Archilochus.

Abstract

Nowadays, there is a major international motivation driving towards the electrification of the aviation industry to reduce its impact on climate change. One of the most promising possibilities for achieving this ambitious goal involves the use of superconducting electrical machines featuring a high power density.

This thesis investigates the preliminary design of an air-core superconducting synchronous machine for future aircraft applications.

After introducing superconductivity from a macroscopic point of view, the state of the art of superconductors for electrical machine applications is presented. Then, some of the most commonly used modeling methods for the simulation of superconductors are analyzed. Two simple case studies are introduced to understand whether it is necessary to consider specific formulations for the analysis of superconductors in electrical machines. The T-A formulation is first implemented as a benchmark, and it is demonstrated that an alternative approach considering an equivalent constant current density in the superconductor provides similar results, at least from a macroscopic viewpoint. The behavior of air-core synchronous machines is presented afterward. This analysis is useful to have analytical expressions of the field in the machine for the preliminary design. In this work, an already-existing sizing procedure is considered and refined to improve its applicability in the design of air-core synchronous machines.

After acquiring the necessary knowledge, the electromagnetic design of a 2.61 MW, 2500 rpm air-core synchronous machine with HTS field windings is carried out. It is proved that, under appropriate assumptions, the well-known sizing equation can be applied even for the design of this type of machine. Moreover, it is shown that the analytical results match well with the ones obtained from FEM simulations.

Contents

List of Figures	4
List of Tables	8
1 Introduction	9
1.1 Road to Net-Zero Emission	9
1.1.1 Hybrid-Electric Architectures	10
1.2 Superconducting Electrical Machines	12
1.2.1 General Characteristics of Superconducting Synchronous Machines	13
1.2.2 Examples of Superconducting Synchronous Machines	17
1.3 Thesis Goal	20
2 Superconductors	21
2.1 Definition of Superconductivity	21
2.1.1 Consequence of Near-Zero Resistivity	22
2.1.2 Superconducting State and Critical Region	23
2.2 Classification of Superconductors	26
2.2.1 Classification by Critical Temperature	27
2.2.2 Classification by Magnetic Field	28
2.3 HTS Materials for Electrical Machine Applications	30
2.3.1 BSSCO	31
2.3.2 YBCO	32
2.3.3 MgB2 Magnesium diboride	34
3 Numerical Modeling of High Temperature Superconductors	35
3.1 Constitutive Relationship: Power Law	35
3.1.1 Definition of J_c	36
3.2 Modeling of HTS Tapes	38
3.2.1 Modeling of a Single Tape	38
3.2.2 Modeling of a Stack of Tapes	41
3.3 FEM Implementation	43
3.3.1 H Formulation	43
3.3.2 A Formulation	44
3.3.3 T-A Formulation	45
3.4 Case Studies	49
3.4.1 Introduction to the case studies	49
3.4.2 Magnetic Circuit	50
3.4.3 Windings in Air	52

CONTENTS

3.4.4	Conclusion from Case Studies	55
4	Preliminary Design of an Air-Core Synchronous Machine	58
4.1	From Iron-Core to Air-Core Machines	58
4.1.1	Rotor Topologies	58
4.1.2	Stator Topologies	60
4.2	Design Approach for Air-Core Synchronous Machines	61
4.2.1	Analysis of field in the Air	63
4.2.2	Design Formulas	68
4.3	Preliminary Design of the machine	72
4.3.1	HTS Synchronous Motor Design	73
4.3.2	HTS Field Winding Design	76
4.3.3	Stator yoke design	79
4.3.4	Validation of the Analytical Design by FEM	80
5	Conclusions and Future Works	85
5.1	Conclusions	85
5.2	Future Works	86
5.2.1	Experimental validation of Superconducting tapes	86
5.2.2	Thermal studies	86
5.2.3	Mechanical studies	87
A	Comsol Modeling of an Electrical Machine	88
A.1	Available data of the Machine	88
A.2	Simulation Set Up	90
A.2.1	Comsol Interface	90
A.3	Results Validation	92
A.3.1	No-Load Simulation	93
A.3.2	Simulation at Load	95
B	10 MW Wind Turbine HTS Generator	98
B.1	Magnetostatics	99
B.2	No-Load phase voltage	100
B.3	Load Simulation	100

List of Figures

1.1	Parallel Hybrid-Electric Propulsion [5].	10
1.2	Turbo-Electric Propulsion [5].	10
1.3	Turbo-Electric Distributed Propulsion [7].	11
1.4	Different Electric Aircraft architectures proposed by NASA [5].	12
1.5	Specific power comparison between all the possible technologies for aircraft propulsion [4].	14
1.6	Size comparison between HTS and conventional synchronous motor for ship propulsion [8]	15
1.7	Fig.a) Loss distribution of a 6000 hp,3600 rpm induction motors at full load [8]; Fig.b) Efficiency map for different types of electrical machines[9].	15
1.8	Fig.a) Air core rotor of a superconducting synchronous machine;1-HTS coil;2-torque tube;3-Electromagnetic shield;4-Turbine and shaft;5-collector end shaft;6-Transfer coupling [9]; Fig.b) Rotor with ferromagnetic core of an SC synchronous machine;1-HTS coil;2-Rotor Body;4-Electromagnetic shield [9].	17
1.9	Illustration of a wound field synchronous machine with a superconducting field winding for ship propulsion applications [8].	17
1.10	Schematic of homopolar alternator with Superconducting field windings [8].	18
1.11	Axial flux synchronous machine for electric aircraft applications [17].	18
1.12	1.5 kW fully superconducting synchronous motor prototype proposed by Nasa [4].	19
1.13	Single-aisle turbo-electric aircraft STARC-ABL proposed by NASA [6].	20
2.1	Falling of Resistance with temperature in Superconductors [19].	22
2.2	Diamagnetic Behaviour of SC [9].	23
2.3	Surface Induced current in a SC Bulk [9].	23
2.4	Superconducting region [14].	24
2.5	Power Law.	24
2.6	Dependence of J_c with operating temperature.	25
2.7	Dependence of J_c with the applied Magnetic field.	26
2.8	Fig. a) Magnetic Flux density component with respect to the surface of the Superconductor [20]; Fig.b) Variation of the critical current with respect the two component of magnetic flux density applied to a SC surface [20].	26
2.9	Discovery of HTS material. Circled in red, some of the most important HTS superconductors [22].	28

LIST OF FIGURES

2.10	Transition from SC state to dissipative state of Type I superconductors [19].	29
2.11	Flux pinning in the mixed state of type II Superconductors [19].	30
2.12	Mixed state in type II Superconductors, the dark regions represent the normal state [19].	30
2.13	Flux pinning in the mixed state of type II Superconductors.	30
2.14	First Generation Superconductor composition [14].	31
2.15	Composition of YBCO tape [26].	32
2.16	Performance Comparison in High Magnetic Field of YBCO and BSCCO SC [14].	33
2.17	Structure and composition of a multifilamentary MgB2 wire [23].	34
2.18	HVDC MgB2 power cable developed by ASG Superconductors [27].	34
3.1	Power Law.	36
3.2	YBCO tape composition [26].	38
3.3	Mesh building for a 0,1 mm thick tape.	38
3.4	HTS tape as an equivalent line.	39
3.5	HTS tape as an equivalent bulk.	39
3.6	Stack of tapes as an equivalent homogeneous bulk: Homogenization.	42
3.7	T-A implementation to the domains.	46
3.8	Superconducting Layer with z-axis current density.	47
3.9	Circulation of the current vector potential T over the superconducting layer.	48
3.10	Boundary conditions to implement in Comsol Multiphysics for T-A formulation.	49
3.11	Fig.a) Linear ramp of the transportation current Fig.b)Distribution of current density and magnetic field in a stack of tapes in steady-state conditions with T-A Formulation.	50
3.12	Fig.a) Distribution of current density(J/J_c) along the tape with T-A formulation; Fig.b) Magnetic Flux density map with T-A formulation.	51
3.13	Fig.a) Magnetic Flux density with equivalent line and constant J; Fig.b) Magnetic Flux density map with T-A formulation.	51
3.14	Fig.a) Magnetic Flux density with equivalent bulk and constant J; Fig.b) Magnetic Flux density map with T-A formulation.	52
3.15	Magnetic Flux density comparison with different simulation methods along the column.	52
3.16	Fig.a) Distribution of current density (J/J_c) along the tapes, T-A formulation; Fig.b) Magnetic Flux density map with T-A formulation.	53
3.17	Fig.a) Magnetic Flux density with equivalent line and constant J; Fig.b) Magnetic Flux density map with T-A formulation.	53
3.18	Fig.a) Magnetic Flux density with equivalent bulk and constant J; Fig.b) Magnetic Flux density map with T-A formulation.	54
3.19	T-A implementation in Comsol Multiphysics.	54
3.20	Fig.a) Rectangle over which the magnetic flux density is registered during the machine's simulation; Fig.b) Control rectangle in which the magnetic flux density is applied as a Dirichlet boundary condition when simulating Superconducting tapes alone.	56

LIST OF FIGURES

3.21	Magnetic Flux density along the vertical boundary of the "control rectangle" with the three different methods.	56
3.22	Magnetic Flux density along the horizontal boundary of the "control rectangle" with the three different methods.	57
4.1	HTS Machine with warm rotor core [35].	59
4.2	HTS Machine with cold rotor core [35].	59
4.3	Different stator topologies of HTS machines,a) Conventional stator,b) Non-Magnetic teeth, c) Slotless stator.	61
4.4	Fig.a) Flux lines patterns in a conventional machine with iron-core rotor and magnetic teeth [36]; Fig.b) Distribution of flux lines in an Air-Core machine.	62
4.5	Generalized Machine Structure [38].	63
4.6	Flux lines distribution in air with different pole pairs [38].	64
4.7	Generalization of the 2-pole machine.	66
4.8	Parametrization of a p pole machine.	68
4.9	Fig.a) General structure of a "pancake" used in HTS field windings [40]; fig.b) 2D view of the HTS field windings modeled as homogenized bulk in the machine.	69
4.10	Correction Factor for Fmm evaluation.	70
4.11	Distance between HTS coils.	70
4.12	Air-core Machine schematization from [32].	72
4.13	Schematic of the Synchronous Motor with HTS field windings [37].	74
4.14	YBCO tape composition [26].	76
4.15	Insulation YBCO tape.	76
4.16	Critical Current for a 4 mm wide YBCO Tape as a function of the perpendicular component of the external magnetic flux density [26]. The YBCO tape of interest is the one indicated with a white square.	77
4.17	Schematization of the HTS tapes in the rotor of the machine.	78
4.18	Magnetic characteristics of FeCo, in red the operation point.	79
4.19	2.61 MW HTS Synchronous motor for Aircraft Application.	80
4.20	Magnetic Flux density map of the 2.61 MW Synchronous motor.	80
4.21	Magnetic Flux distribution at mean armature stator windings radius.	81
4.22	Magnetic Flux distribution at mean armature stator windings radius without correction factor.	82
4.23	No-Load Phase voltage of the HTS Synchronous motor.	83
4.24	Magnetic flux density map at load.	83
4.25	Electromagnetic Torque as a function of the mechanical angle.	84
A.1	Finalized geometry of the Machine.	90
A.2	Winding sequence for a pole pair of machine.	90
A.3	Electrical circuit implemented in Comsol.	91
A.4	Mesh on one pole pair of the machine.	92
A.5	Detail of the mesh in the air-gap.	92
A.6	Magnetic Flux Density Map from Comsol.	93
A.7	Comparison between Magnetic Flux Density distribution to the Air-Gap	93

LIST OF FIGURES

A.8	Fig.a) No-Load characteristics comparison between Comsol and flux; Fig.b) No-Load Characteristics comparison between Flux and experi- mental results [44].	94
A.9	Electrical circuit implemented in Comsol [43].	95
A.10	Fig. a) Magnetic Flux Density Map for WP2 simulated with flux [43]; Fig. b) Magnetic Flux Density Map for WP2 simulated with Comsol. .	96
A.11	Torque comparison between Flux and Comsol with different size and discretization of the mesh.	96
B.1	Fig. a)Magnetic flux density distribution from [37] ;Fig. b) Magnetic Flux density distribution obtained through design formulas 4.2.2	99
B.2	Fig. a) Magnetic Flux distribution at mean armature stator windings radius from Comsol; Fig. b) Magnetic FLux density distribution from [37].	99
B.3	No-Load phase Induced Voltage obtained with Comsol Multiphysics 4.2.2.	100
B.4	Electromagnetic torque evaluated from Comsol	101
B.5	Rotor Surface that has been selected for the Torque evaluation.	102

List of Tables

2.1	Comparison of BSCCO and YBCO for electrical machine applications [14].	34
4.1	Radial distribution of magnetic flux density with different pole pairs.	65
4.2	Basic Design Parameters of the Synchronous HTS Motor.	73
4.3	Operation parameters and dimension chosen for the motor.	75
4.4	YBCO Tapes parameters.	78
4.5	Fast Fourier Transform of the stator magnetic flux density	81
4.6	Fast Fourier Transform of the stator magnetic flux density	82
A.1	Specifications of the Machine.	88
A.2	Geometry dimensions of the Machine.	89
A.3	Stator and rotor windings characteristics.	89
A.4	Working points suggested by the company to calibrate the FEM model [43].	92
A.5	Working points suggested by the company to calibrate the FEM model [43].	95
A.6	Torque Comparison between Comsol, Flux and experimental results.	97
B.1	Basic Design parameters of HTS Wind-Turbine Synchronous Generator [37].	98
B.2	Physical Dimensions and design parameters [37].	98
B.3	Torque Comparison obtained through Comsol and from theoretical Sizing equation.	102

Chapter 1

Introduction

To start, a brief introduction to the motivations that are pushing the scientific community and the industry towards electrification of the aeronautical sector is provided. Following, an overview of the beneficial effects of employing a superconducting electrical machine will be given. Lastly in this chapter, some examples of applications that have been employed in the past are discussed.

1.1 Road to Net-Zero Emission

The impact of the aviation industry on total global emissions is going to be more relevant in the next years. Since these emissions are directly expelled at high altitudes, they have a very strong effect on the shielding upper layer of the atmosphere [1]. To minimize the emissions, an ambitious program was prepared by the European Commissions, together with leading companies in the sector. According to the roadmap FlightPath 2050 [2] the final goals of this program are the following:

- 75% reduction of the CO_2 ;
- 90% reduction of the NO_x ;
- 65% reduction of the perceived noise;

With respect to the capabilities of typical aircrafts that are operating nowadays [3].

Although it is still possible to reduce emissions through further refinement of aircraft engines, simply improving the traditional turbine technology won't lead to the complete achievement of these goals [4]. That's why electric propulsion will be necessary for the future.

Electric propulsion could bring to the aviation industry several benefits [5]:

- Low emissions
- Less atmospheric heat release
- Quieter flight

- Better energy conservation due to improved efficiency
- More reliable systems

Since the energy density and power density values of the battery are not enough to think about a fully electrical architecture, the most promising alternative is a hybrid-electric architecture that employs Hydrogen fueled gas turbine and electric motors/generators. It is shown in figures 1.1,1.2 in its different version: Parallel and Turbo-Electric; It can be used for propelling from small to large size aircraft [5]

1.1.1 Hybrid-Electric Architectures

Generally speaking, there are two types of hybrid-electric system architectures that could be used for the propulsion of the next generation of aircraft, and they are synthesized just below:

- **Parallel Hybrid-Electric**

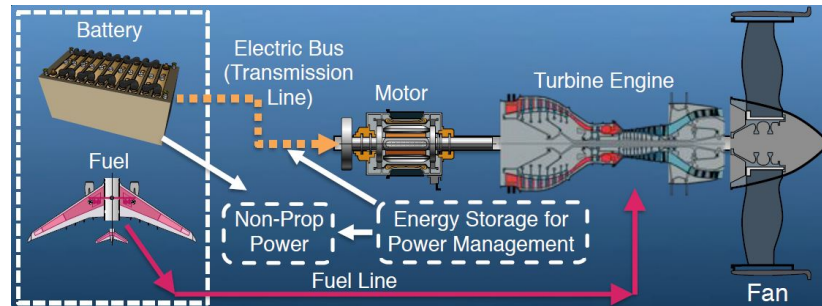


Figure 1.1: Parallel Hybrid-Electric Propulsion [5].

Parallel hybrid concept uses a battery that provides a fraction of the power needed for the run, however, the main part of the power required is given by the fuel, Hydrogen in this case, which is used to supply a turboengine directly connected to the fan. This architecture, can reach over a 60% efficiency improvements with respect to a baseline aircraft [6] and this hybrid-electric concept can be used for aircraft capable of transporting up to 150 Pax like presented in [5].

- **Turbo-Electric Propulsion**

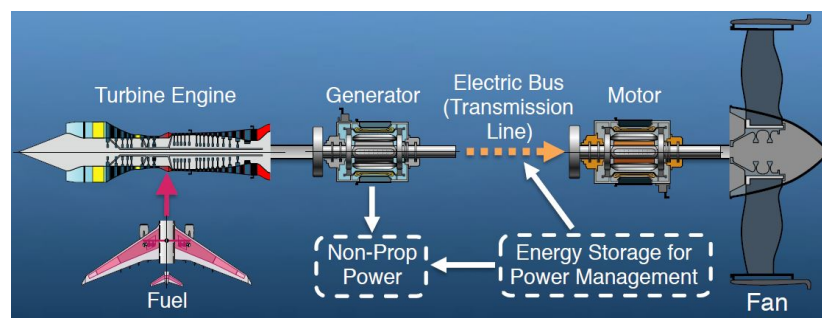


Figure 1.2: Turbo-Electric Propulsion [5].

The turbo-electric architecture uses Hydrogen as a fuel of a turbine engine directly connected to a generator. This last produce the power needed by the motor to move the Fan. According to [6] with an efficiency of the electrical machines of 96%, it is possible to achieve a 7-12 % reduction of fuel consumption. Even this architecture is optimal for medium scale aircraft with 150 Pax.

- **Turbo-Electric Distributed Propulsion**

For the biggest aircraft concept, it is also possible to exploit the beneficial effect of using more electric motors supplied by a single generator. This last configuration, called turbo-electric distributed propulsion (figure 1.3), will allow to supply even the more advanced concept of aircraft like, for example, the N3-X concept (figure 1.4) from NASA [3], capable of transporting up to 300 Pax. Obviously, this will require the greatest amount of specific power from the hybrid- electric propulsion system.

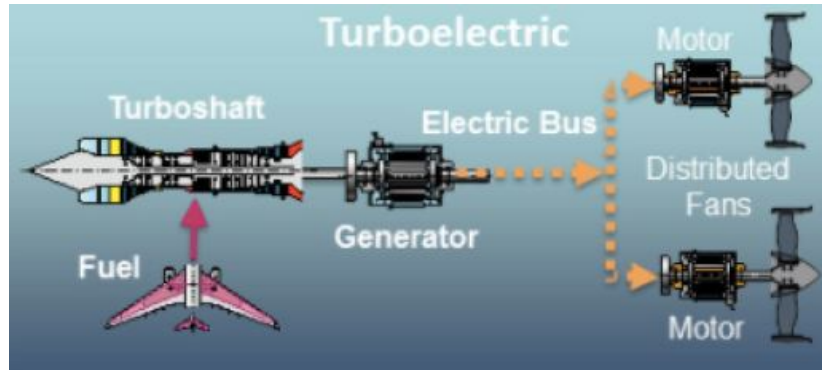


Figure 1.3: Turbo-Electric Distributed Propulsion [7].

The main problem of implementing a HEPS (Hybrid Electric Propulsion System), with the current technology, is the value of specific power that the conventional rotating electrical machine can provide. It varies approximately in a range of $0.5-2.5 \text{ kW/kg}$, with some exception of 5 kW/kg [4] depending on the speed. These values are far below the specific power needed for the medium and long-range aircraft [4].

Therefore, to meet the stringent requirements of specific power, here the superconducting machines emerge among the possible solutions. Thanks to the superconductor's characteristics of having near-zero DC resistivity at cryogenic temperature, an electrical machine with superconductors can increase the specific power up to 20 kW/kg or even more [4].

A roadmap for different concepts of future electric aircraft has been studied by NASA [5]. In figure 1.4 it is clear how the superconducting technology will be needed as long as the number of passengers increases, and so the power needed. Therefore, the number of cryogenic devices will be increased in the near future.

Moreover, we can see the N3-X concept which will require a propulsive system capable of delivering 30 MW of electric power. The N3-X concept, is the ultimately long range aircraft that will allow a reduction of the 70% of the total emission with respect to a conventionally powered design. The technological feasibility of this concept highly

depends on the availability of very light-weight electric machines and components.

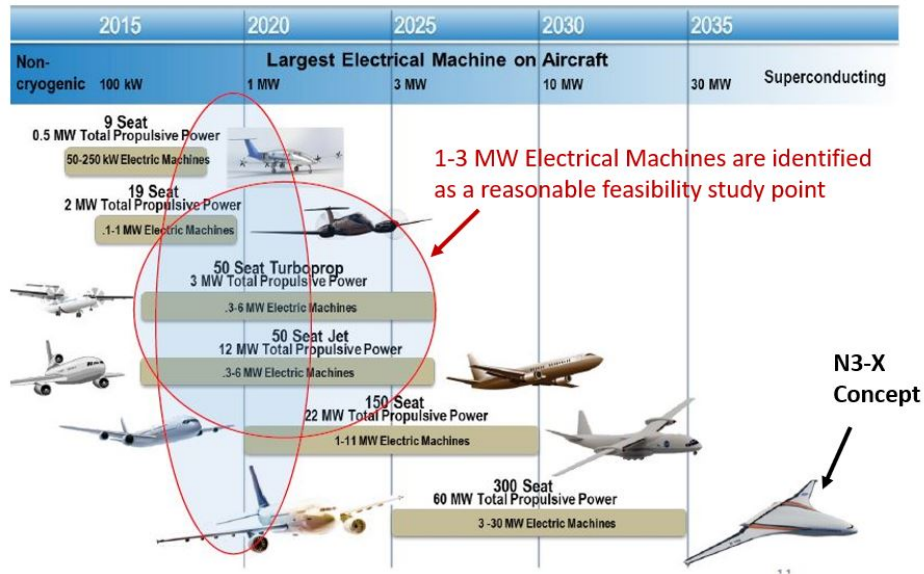


Figure 1.4: Different Electric Aircraft architectures proposed by NASA [5].

1.2 Superconducting Electrical Machines

Before going into more detail about superconducting machines, it must be said that superconductors are divided into two main categories: LTS (Low-Temperature Superconductors) and HTS (High-Temperature Superconductors), which are distinguished by the temperature at which they can work. The detailed information will be reported in chapter 2. However, even if LTS were used in the first attempts of implementation of the superconducting technology to electrical machines, the one of interest for the superconducting electrical machines (SEM) are HTS.

There are two types of SEM that differ from where they actually employ SC in the machine. Let's explain better:

- Partially Superconducting Machines (PSCM):**
 Which are manufactured employing both superconductors and conventional conductors (copper) and permanent magnets. In the case of synchronous machines, HTS field windings are used in the rotor. In PSCM, a cryostat is usually used to keep the HTS windings at the desired temperature [8];
- Fully Superconducting Machines (FSCM):**
 Which employ SC wire both in stator and rotor. Such machines are usually completely submerged in a cryogenic environment.

1.2.1 General Characteristics of Superconducting Synchronous Machines

Challenges and Opportunities

With their ability to carry high currents, superconducting windings will allow increasing significantly the performance of EM (Electrical Machines). For instance, a first advantage of using SC wire in synchronous machines is the neglect of the Joule losses RI^2 in the field windings. Further, the magnetic flux density produced by HTS field windings can be increased by $2x$ or even $3x$ with respect to a conventional machine. This is one of the most interesting features of employing superconductors in EM. Moreover, the conventional limits given by the saturation of the ferromagnetic teeth can be overcome because it is possible to build a stator with no ferromagnetic material (see chapter 4), leading to light-weight and high power density machines. Synchronous machines with HTS winding show the following general advantages [9][8]:

- Higher power density with respect to classical machines [4][3];
 - Reduced mass and volume [4][3];
 - Increased efficiency thanks to the reduction of Joule losses in all of the operating range [10][8];
 - Low synchronous reactance, small load angle and improved stability [8];
 - Lower harmonic content of induced voltage due to the nonmagnetic teeth part and a larger air gap [8];
 - Reduced acoustic noise [5];
 - Less maintenance: No re-winding or re-insulation required [8],[9];
- **High power density**

Both partially and fully superconducting electrical machine could be used in the future in the aviation industry [11]. Several studies have been done in the literature about the requirement for the specific power of the new aircraft (fig.1.4). It has been concluded in [3] that for the hybrid-wing-body concept aircraft N3-X shown a PTW (Power to weight ratio) of $12.7kW/kg$ is needed. This target is only feasible with a fully superconducting machine [3]. Unfortunately, due to the high ac losses of the HTS (High-Temperature Superconductor) armature windings, fully superconducting technology is not feasible yet. Further research work has to be done for reducing losses in HTS when operated with ac current and therefore subjected to ac fields [12] [1]. In the meantime, it is possible to push through electrification of the aviation industry using both conventional electrical machines and partially superconducting electrical machines. Indeed, PSCM can reach a specific power up to $10kW/kg$ [3] and this is good enough for medium-size 150 Pax aircraft indicated by NASA in figure 1.4. In the following picture (1.5) is shown how the specific power density reachable by an HTS machine can be greater than the turbo engine used nowadays. As it is possible to see, conventional electrical machines have too low power density values compared

to the gas turbine engine that is in use nowadays in aircraft applications. While from power size from 1 MW, the size indicated as a starting point for the studies by NASA [5], partially superconducting machines, (HTS homopolar alternator in figure 1.5), and fully superconducting machines can even overcome the power density requirements for the most common used aircraft nowadays.

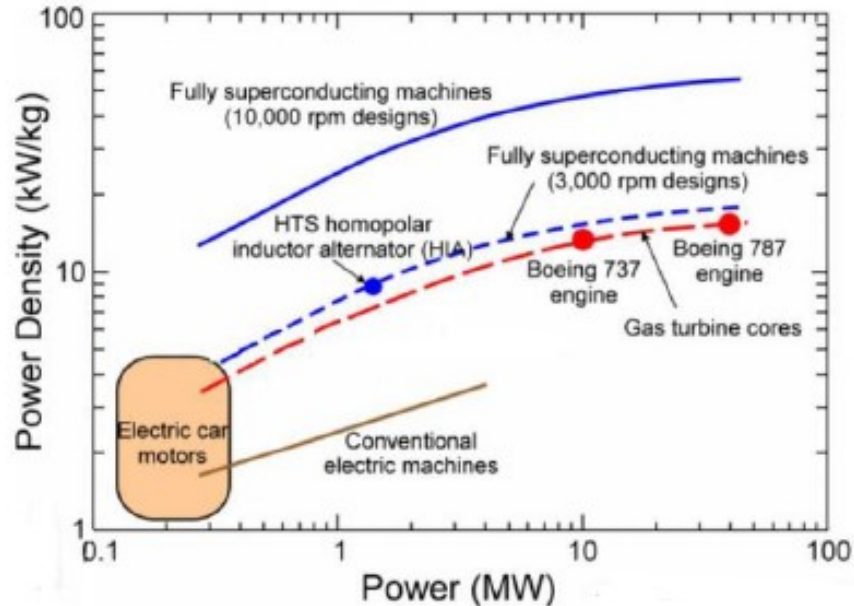


Figure 1.5: Specific power comparison between all the possible technologies for aircraft propulsion [4].

These power density improvements results in a reduction of the overall volume of the machines and an example of the entity of this reduction is shown in the following figure (1.6), where two synchronous ship propulsion machines are presented. Wound field synchronous machines were identified as ideal candidates for ship propulsion applications [8]. In this field, several prototypes have been constructed during the early stage [10],[13]. In fact, this is one of the sectors in which the development of superconducting machines is more promising and close to an implementation [13].

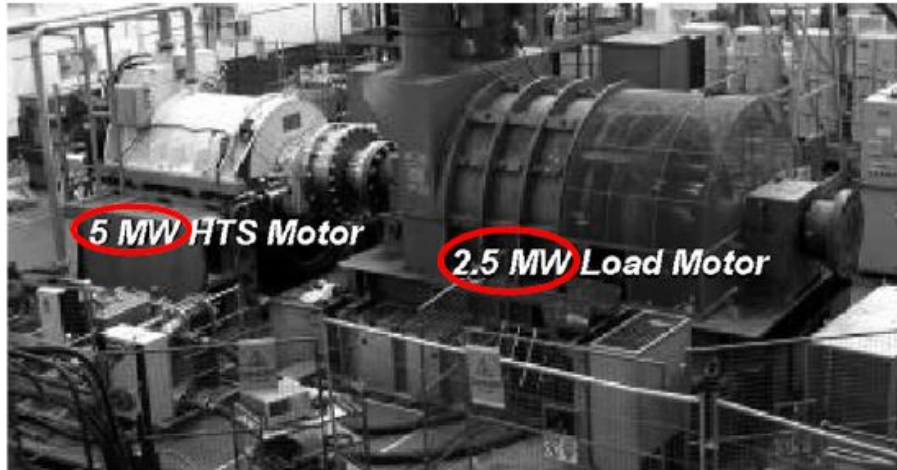


Figure 1.6: Size comparison between HTS and conventional synchronous motor for ship propulsion [8]

- **High Efficiency at all loads**

Two important characteristics of superconducting synchronous machine must be mentioned. Firstly, the overall losses decrease thanks to the elimination of Joule losses and the iron losses (figure:1.7a). Secondly, the higher efficiency resulting from lower losses is maintained throughout the whole operating range of the machine (figure: 1.7b). Regarding superconducting machines, as long as the non-ferromagnetic structure is used, most of the losses related to a conventional machine are drastically reduced. From figure 1.7a, it is possible to note that another type of loss emerges, the one related to the cryocooler for maintaining the working temperature. However, the important thing is the overall reduction of losses, with a consequent increase in efficiency, that it is possible to obtain employing superconductors. In figure 1.7 two different machines, with the same rated power, for ship propulsion are compared in terms of losses components. It is possible to see how the superconducting synchronous machine, despite the cryocooler, is more efficient.

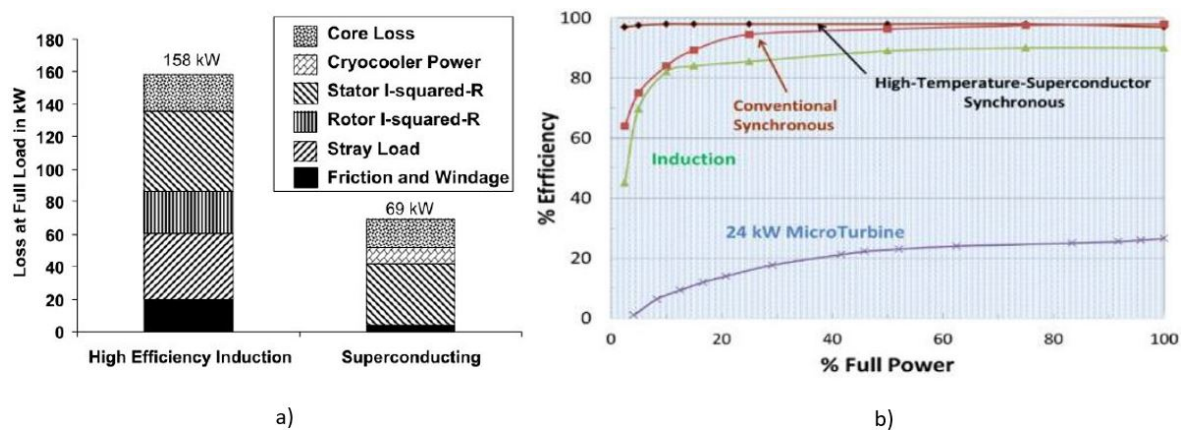


Figure 1.7: Fig.a) Loss distribution of a 6000 hp,3600 rpm induction motors at full load [8]; Fig.b) Efficiency map for different types of electrical machines[9].

The advantages that can be exploited employing superconducting electrical machines are worth it, however, there are three main disadvantages, that are slowing down the development and the use of such machines:

1. High cost of production of superconductor [14],[9];
2. Complex cooling system [14],[15];
3. Intrinsic operating problems on the use of superconductors, chapter 2;

All of them are related to the utilization of superconductors: High cost of production is probably the most limiting one because it doesn't allow the increase in the demand of this technology; Complex cooling and redundant system are needed for the operation of SC in electrical machines. Lastly, there are also some problems regarding the physical feature of SC which complicate their development on large scale. Indeed, as will be explained in detail in chapter 2, superconductors need to work under specific conditions that must be kept constant.

Anyway, it is predictable that further works of the entire scientific community will succeed in the near future.

Construction Characteristics

There are two possibilities on the construction of SC synchronous machines [9]:

- **With Coreless Rotor** (Air-Core Machine) figure 1.8a;
- **With Ferromagnetic-Core Rotor** figure 1.8b;

The Air-Core configuration shown in fig.1.8a presents a non-ferromagnetic rotor in which there are HTS field windings, without the limit of saturation, in this type of machine it is possible to obtain the highest values of TTW (Torque to Weight ratio), and so the PTW (Power To Weight ratio) because the magnetic flux density can be pushed up to very high values, even 5T. Later in this thesis work will be shown that depending on the diameter of the machine, this value will be more realistically near to 2-2.5 T, (see chapter 4). The main drawbacks of using an Air-Core rotor are two: The electromagnetic force is applied directly on SC wire causing mechanical concerns; This type of rotor configuration requires the largest amount of SC material, making air-core machines more expensive than the one with ferromagnetic core. This option is the best suited rather for low and medium - speed machines [9].

On the other hand, with a ferromagnetic rotor core configuration (fig.1.8b), the amount of SC material is significantly lower because of the high permeability of the steel with respect to the air, and the speed of the machine can be increased up to 15000 rpm, however, the saturation of the steel part limits the magnetic flux density, and therefore limits the beneficial effect of using SC, resulting in TTW values not so far from the conventional EM.

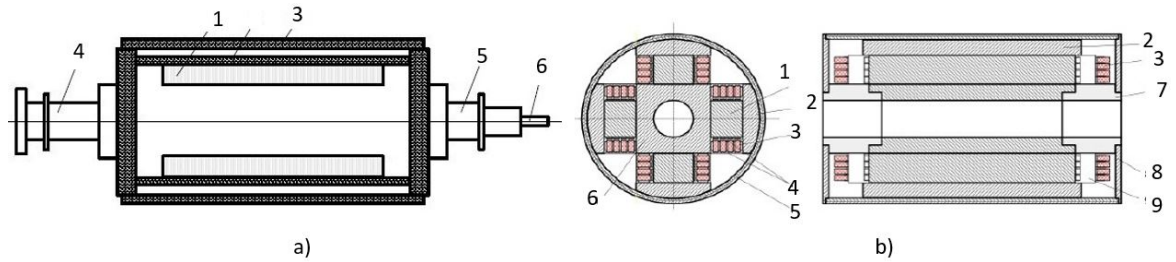


Figure 1.8: Fig.a) Air core rotor of a superconducting synchronous machine;1-HTS coil;2-torque tube;3-Electromagnetic shield;4-Turbine and shaft;5-collector end shaft;6-Transfer coupling [9]; Fig.b) Rotor with ferromagnetic core of an SC synchronous machine;1-HTS coil;2-Rotor Body;4-Electromagnetic shield [9].

1.2.2 Examples of Superconducting Synchronous Machines

According to the construction characteristics presented before, it is possible to build different combinations of superconducting synchronous machines to exploit the feature of SC to carry extremely high levels of current with near-zero resistivity. In the past, several prototypes have been constructed, especially for marine applications [10]. An example of the common structures of such machines is shown in figure 1.9, thanks to the relatively slow rotational speed and high torque required, such synchronous machines are ideal candidates for their employment in ship propulsion applications.

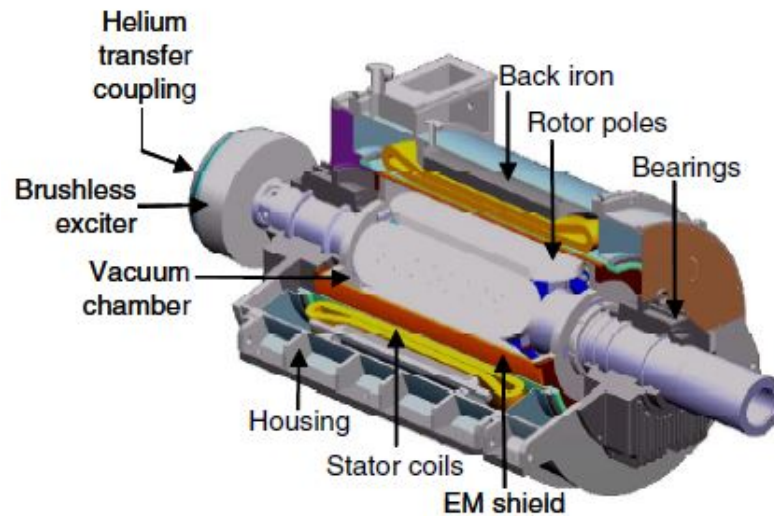


Figure 1.9: Illustration of a wound field synchronous machine with a superconducting field winding for ship propulsion applications [8].

In applications in which the specific power requirement are stringent, one interesting possibility of using the partially superconducting machine is the utilization of Homopolar machine configuration, shown in figure 1.10, which consist of a fixed HTS winding carrying a DC current and a ferromagnetic core which guide the flux lines [16]. In this machine, the required power is achieved thanks to the extremely high rotational speed that it is possible to exploit. Moreover, this layout simplifies the design of the

cryostat since it has fixed parts only. The superconducting field coil can produce higher magnetic flux density in the air gap compared to a conventional structure. The use of a single-piece rotor, shown in figure 1.10, allows to exploit very high rotational speeds with a simplified mechanical support and electrical connections [8]. An accurate design of the rotor's shape makes that the stator winding experiences an alternating magnetic field. However, these types of machines are larger in size compared to an equivalent Superconducting machine with air-core structure [8]. One of the main applications of the homopolar machine concept can be found in electric generators coupled with high-speed gas turbines for electric aircraft [8].

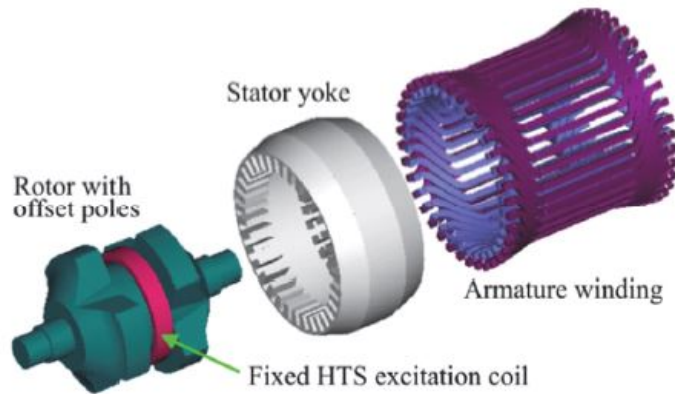


Figure 1.10: Schematic of homopolar alternator with Superconducting field windings [8].

Another configuration of partially superconducting synchronous machine includes an axial structure employing copper in the stator windings and superconducting coils that produce the field on the rotor. Moreover, there are superconducting coils that act as shields to modulate the field in such a way that it interacts with that created by the stator for the production of torque. In figure 1.11 a 50 kW prototype that can rotate up to 5000 rpm is shown. These machines have the potential to be used for both ship and aircraft application.

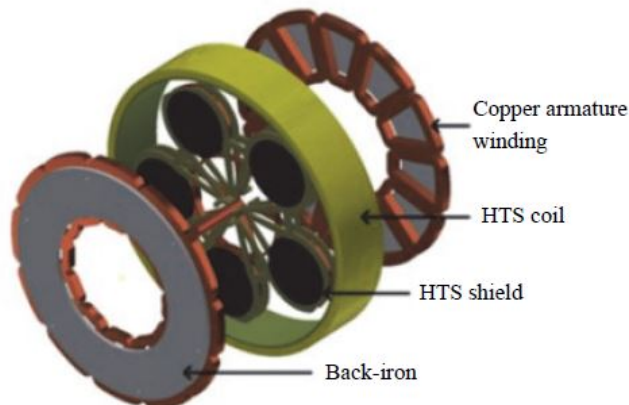


Figure 1.11: Axial flux synchronous machine for electric aircraft applications [17].

However, one of the most promising possibilities is the wound field synchronous machine that employs an air-core structure. In this type of machine, superconductors are

made to work in the best conditions, carrying a DC transport current, that allows achieving extremely high magnetic flux density and medium-high rotational speed as proposed in [1], which could fit for the medium size aircraft concept proposed by NASA [18]. A general review of the specification of all of these machines with respect to the requirements of the sector is summarized in [11].

Lastly, in the recent years, prototypes of fully superconducting machines employing air-core rotor and iron stator yoke have been constructed by NASA [4], their popularity is expected to grow as long as there are developments in ac losses reduction [12]. An example, is provided in figure 1.12, in which a 1.5 kW motor prototype is shown.

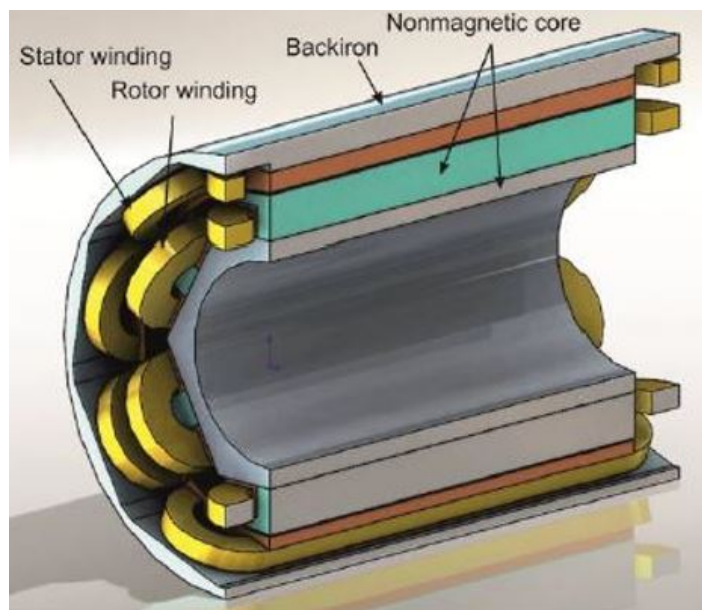


Figure 1.12: 1.5 kW fully superconducting synchronous motor prototype proposed by Nasa [4].

1.3 Thesis Goal

According to what has been said so far, it is clear that the several benefits of superconducting machines constitute a solid motivation to continue scientific research on developing lighter, more efficient, and more reliable machines. In this context, this thesis fits in with the purpose of being a starting point for electrical engineers who are approaching the world of superconductors and the design of superconducting air-core synchronous machines for the first time. In particular, in this thesis work, it will be presented the macroscopic behaviour and the general characteristics of the most common superconducting material in use nowadays, as well as their classification in terms of electromagnetic and thermal response. This is the scope of chapter 2. Following, superconductors are treated more in detail in chapter 3 in which some of the most important modeling methods are explained, at the end of this chapter, explanatory simulations will be provided through two simple case studies. The aim is to acquire sufficient knowledge about the distribution of current density in SC, and the external effect in terms of magnetic flux density, which is one of the most important parameter for the electromagnetic design of a machine with SC. The ultimate goal of the thesis is to provide a preliminary design of a superconducting synchronous machine, which respond to the specifications and requirement of the aviation industry. In particular, the 2.61 MW, 2500 rpm HTS motor expressed in [6],[18], which is the motor that directly moves the fan of the single-aisle turbo-electric aircraft STARC-ABL shown in figure 1.13. At the beginning of chapter 4, a collection of the general laws which govern the behavior of fields in the air is shown, successively, these equations are used to purpose a possible design approach of an air-core synchronous machine with an iron stator yoke. The actual design and simulation of the aircraft's machine are done at the end of chapter 4, in this section, the match between the theoretical results and the results provided by the FEM software is checked. Finally, in chapter 5 , some final considerations together with suggestions for possible future works are drawn.



Figure 1.13: Single-aisle turbo-electric aircraft STARC-ABL proposed by NASA [6].

Chapter 2

Superconductors

In this chapter, the macroscopic behavior and the general characteristics of superconductors are presented. Firstly, the near-zero DC resistivity concept and its consequences will be introduced, subsequently, a classification of superconductors based on temperature and magnetic field will be provided to better understand these materials. In the end, some of the most commonly used superconducting materials for electrical machine applications will be presented.

2.1 Definition of Superconductivity

Superconductivity was first discovered in 1911 by *Heike Kamerlingh Onnes*, a Dutch Physicist who was working on Hg samples at 4.2 K [19]. Superconductivity is a phenomenon that can be explained only with Quantum Mechanics, in this thesis work, it will be treated from the point of view of an electrical engineer who is only interested in macroscopic effects.

Superconductivity is a phenomenon occurring in certain elements and alloys, generally called Superconductors (SC), which exhibit a **Near-Zero DC Resistivity** when operating in their superconducting State. However, if subjected to an ac field, Superconductors exhibit significant losses.

This feature is one of the main problems in their use of electric machines [12], reduction of ac losses is the hottest research topic in the scientific community [12] because it will allow the development of FSCM with an extraordinary Power-To-Weight ratio, which is crucial for the aviation industry as already said in the chapter (1). For this reason, at the moment, to take the best out of superconductors it is necessary to make them work under DC conditions and under an electromagnetic shield that protects them from ac fields.

In figure 2.1 it is possible to appreciate the behaviour of superconducting materials with the temperature. Under a specific temperature called *Critical Temperature*, the resistivity of the superconductor drops to "near-zero", where near-zero means a value that is not easily measurable experimentally.

As a matter of fact, there is no correlation between the performance of Superconductors above and under the critical temperature [19]. Indeed, their resistivity at ambient temperature is very high with respect to the copper.

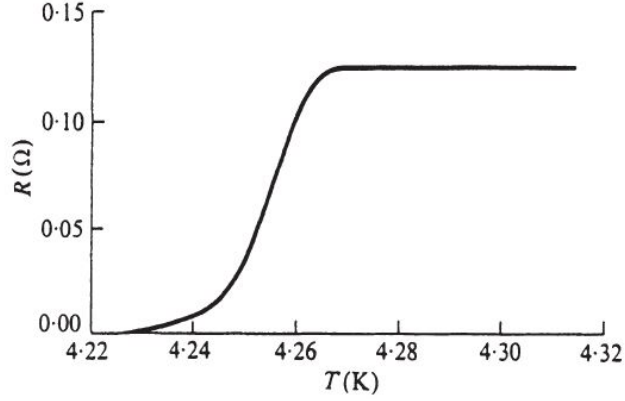


Figure 2.1: Falling of Resistance with temperature in Superconductors [19].

2.1.1 Consequence of Near-Zero Resistivity

There are several implications due to a Non-Measurable Resistivity that are well explained in [9]. The first is the possibility of carrying extremely high DC with no power losses, which is the main benefit from an electrical Engineer point of view, but there is another important effect that is a direct consequence of zero resistivity: The Meissner Effect.

Meissner Effect

Let's consider a ring of superconducting coil in short circuit in which is circulating a current i . The equation that describes the state variables is the 2.1:

$$u = Ri + L \frac{di}{dt} = 0 \quad (2.1)$$

Where R is the resistance of the superconductor, i is the current which is flowing and L is the inductance of the coil loop. If $R=0$ the equation becomes:

$$L \frac{di}{dt} = 0 \implies \frac{d\Lambda}{dt} = 0 \quad (2.2)$$

This leads to the conclusion that $\Lambda = \text{constant}$. This is a very important result because it means that the magnetic field is *Memorized* and the SC can be used as a field source when it is in the superconducting state.

Consequently, the Meissner Effect can be expressed as the expulsion of the magnetic field from a superconductor, this concept is illustrated in figure 2.2.

Since the initial flux state of the SC must be maintained, when an external magnetic field H_a is applied to the superconductor, currents are induced in the SC to create an internal opposing magnetic field H_i as expressed in equation 2.3.

$$H_{sc} = H_a + H_i = 0 \quad (2.3)$$

Where H_{sc} is the sum of the external applied magnetic field and H_i the internal magnetic field produced by the SC to keep its initial state.

The illustration of the currents that are induced to counteract the external applied magnetic fields are shown in figure 2.3.

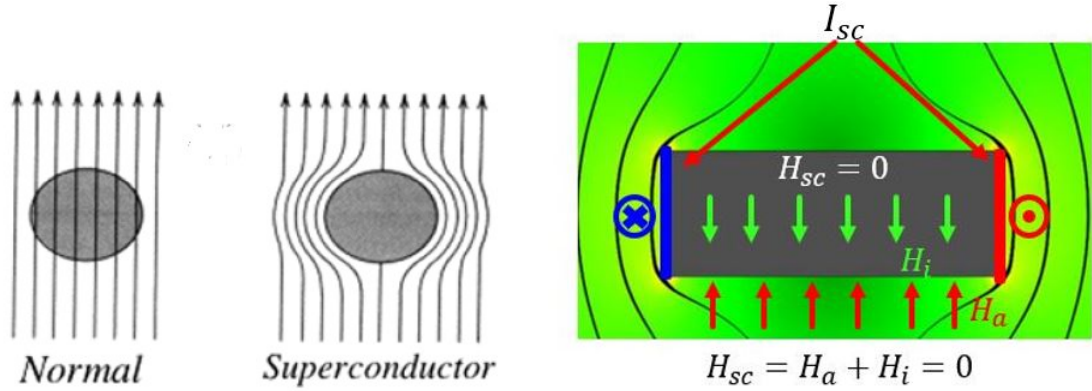


Figure 2.2: Diamagnetic Behaviour of SC [9]. Figure 2.3: Surface Induced current in a SC Bulk [9].

2.1.2 Superconducting State and Critical Region

Superconducting State is characterized by three fundamental parameters [14]:

- Critical Current Density J_c ;
- Critical Temperature T_c ;
- Critical Magnetic Field H_c ;

Whenever one of these parameters is exceeded, the material leaves superconductivity and loses the characteristic of Near-Zero resistivity. It is important to mention that these parameters are not constant.

The transition to the normal state of the SC is called *Quenching* and it is very dangerous because in the normal state the resistivity drastically increases so the losses in the SC increase, and consequently the heat production increases. This process leads to local hot-spots and destruction of devices [14]. Moreover, since SC is not a good conductor at ambient temperature, this can be a serious problem for the reliability of the application that employs superconductors.

To maintain its characteristics, the working point of the SC must be always inside the superconducting region shown in figure 2.4.

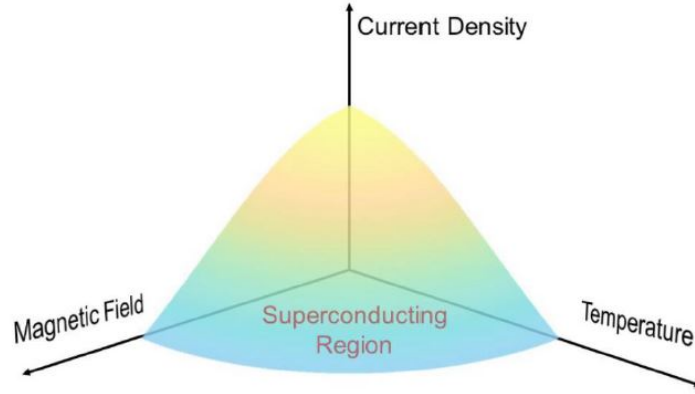


Figure 2.4: Superconducting region [14].

A Superconductor is characterized by the E-J curve, called **Power Law**, which describes the electrical field as a function of the current density, or rather, the voltage drop along the length of the SC as a function of its current [14]. So the resistivity itself of the SC:

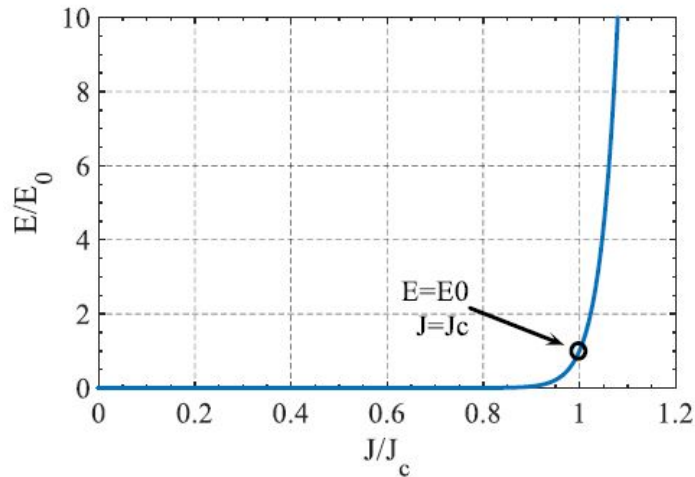


Figure 2.5: Power Law.

Power Law can be described analytically as follow:

$$E = E_0 \left(\frac{J}{J_c} \right)^n \quad (2.4)$$

Where n is an index value and depends on the material: A higher n -value produces a sharper transition in the E-J curve and indicates the quality of a superconductor [14]. While the critical electric field $E_0 = 1 \frac{\mu V}{cm}$, shown in figure 2.5 has been decided conventionally and it represents the electric field produced in the superconductor when there is the critical current density J_c , and so when it is carrying the critical current. While J is the actual current density in the superconductor. In this context, the Power Law is useful to understand how the critical parameters can

change with the operating condition of the SC. This is important because it allows taking some safe margin in the operating conditions in order to stay in the superconducting region of figure 2.4.

Dependence of the J_c on the operating Temperature

Let's consider a SC that is carrying a DC current with an operating current density $J < J_c$:

- If the operating temperature increases, J_c decreases;
- If the operating temperature decreases, J_c increases;

In particular in fig. 2.6 it is possible to see that there are different "power Law" curve at different temperatures, with a reduction of J_c .

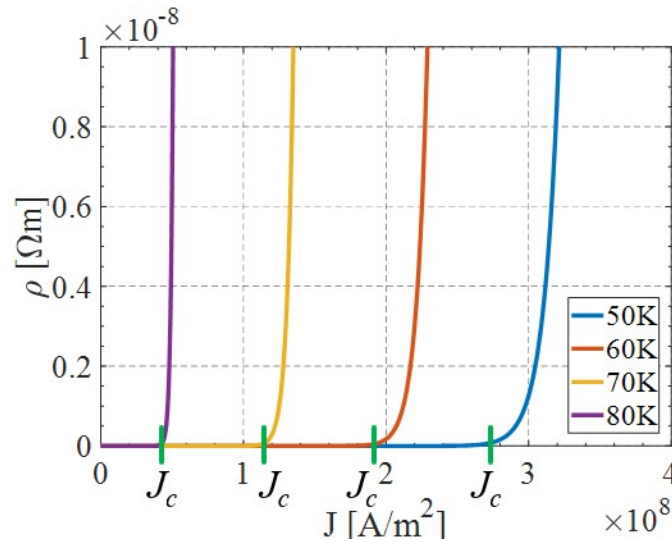


Figure 2.6: Dependence of J_c with operating temperature.

Dependence of the J_c on the applied magnetic field

The same situation can be repeated with the applied magnetic field:

- If the applied magnetic field increases, J_c decreases;
- If the applied magnetic field decreases, J_c increases;

The reduction of J_c due to an increase of the applied Magnetic field can be equally important with respect to the one as a function of the temperature, it can be seen in fig 2.7.

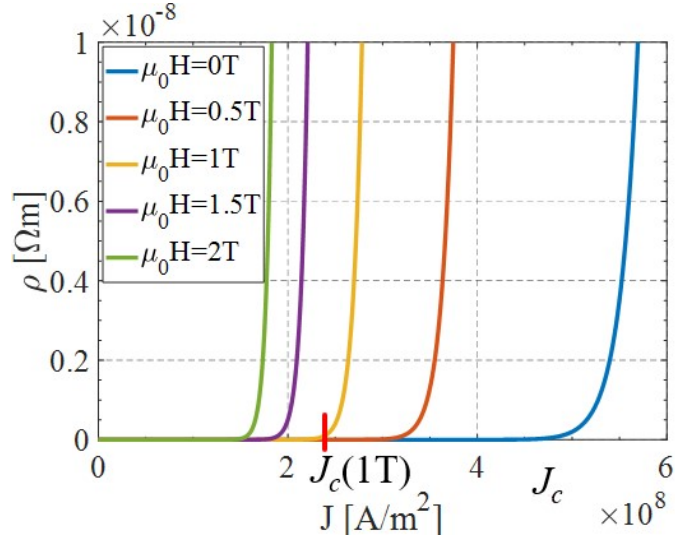


Figure 2.7: Dependence of J_c with the applied Magnetic field.

The reduction of the critical current density J_c is strongly affected by the perpendicular component of the magnetic flux density with respect to the SC surface. The parallel component to the surface has limited effect [20]. An illustration of this concept is proposed in figure 2.8.

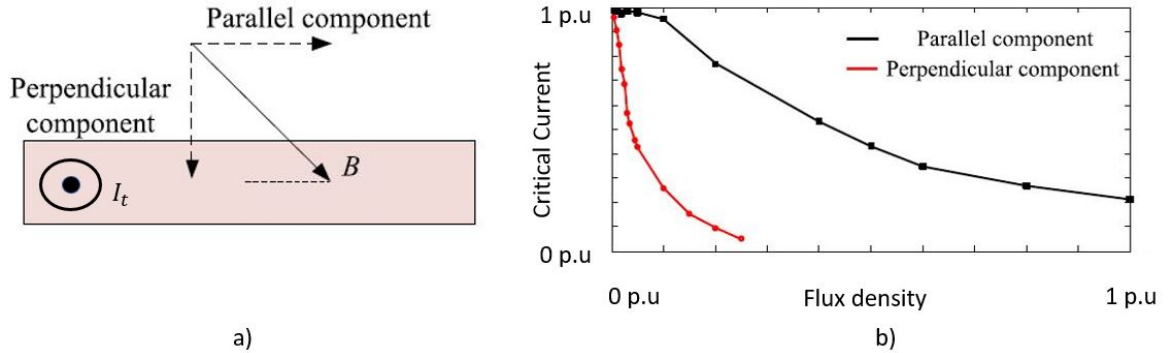


Figure 2.8: Fig. a) Magnetic Flux density component with respect to the surface of the Superconductor [20]; Fig.b) Variation of the critical current with respect the two component of magnetic flux density applied to a SC surface [20].

When employing superconductors in electrical apparatus, all of these aspects must be taken into account in order to have a proper level of reliability.

2.2 Classification of Superconductors

Before moving on to a more detailed classification of Superconductors, there is to say that superconductors can be made in the form of tape or bulk. In particular, tapes are usually used as "wire", while bulks can be used as shields or field sources. In this thesis work, the focus will be on the tape, which can be used as field windings in wound

field synchronous machines. For a more detailed discussion about bulks, the reader is referred to [21].

2.2.1 Classification by Critical Temperature

Superconducting material can be classified on the basis of their *Critical Temperature* T_c , or rather, the temperature at which the electrical resistivity of the material drops to zero as shown in figure 2.1, Therefore:

- **LTS** Low Temperature Superconductors;
- **HTS** High Temperature Superconductors;

LTS Low Temperature Superconductor

As suggested in [9], materials with a $T_c < 30$ K are usually considered Low-Temperature Superconductors.

LTS has been, and they are nowadays, in use successfully for scanner MRI applications and other high magnetic field applications like Particle Accelerators and Magnetic Fusion devices [14]. The most common used superconducting material that works at low temperatures are the following:

- *NbTi* Niobium-Titanium
- *Nb₃Sn* Niobium-tin

Both must operate with a temperature below 4.2 K, therefore liquid Helium is used as a coolant for LTS. Since they are not any more of interest for electrical machine (EM) Applications, no further consideration will be made in this thesis work. Indeed, the reasons are easily understood, cooling at 4.2 K the SC material inside an EM environment is quite a challenge. It requires too big and expensive cooling systems and the cooling efficiency is very low. All of these technical requirements of LTS has discouraged their use in electrical machine.

HTS High-Temperature Superconductor

The material with a $T_c > 30$ K, goes under the name of High-Temperature Superconductors. HTS cuprate-perovskite ceramic materials were discovered in 1986 (fig.2.9) and immediately resurrected interest in developing superconducting electrical applications like motors, generators, transformers, fault current limiter, and power cables, [8],[14]. The use of cuprates (copper oxides) allows for more friendly thermal properties. For instance, at 77 K (Temperature of Liquid Nitrogen) cryogenics become 40 times more efficient than at 4.2 K and Nitrogen is a much cheaper resource than Helium. For this reason, the room-temperature electric power required to operate a 77 K refrigerator is less than $\frac{1}{10}$ that required for a 4.2 K refrigerator [14].

In short, HTS has made it possible to significantly reduce the cost and size of cooling

systems opening up to the possibility of developing electrical devices using superconductors on a large scale. In figure 2.9 below, an overview of the critical temperature and the year of discovery of the most common superconducting material is presented. Circled in red are some of the most interesting for power electric equipment applications [9].

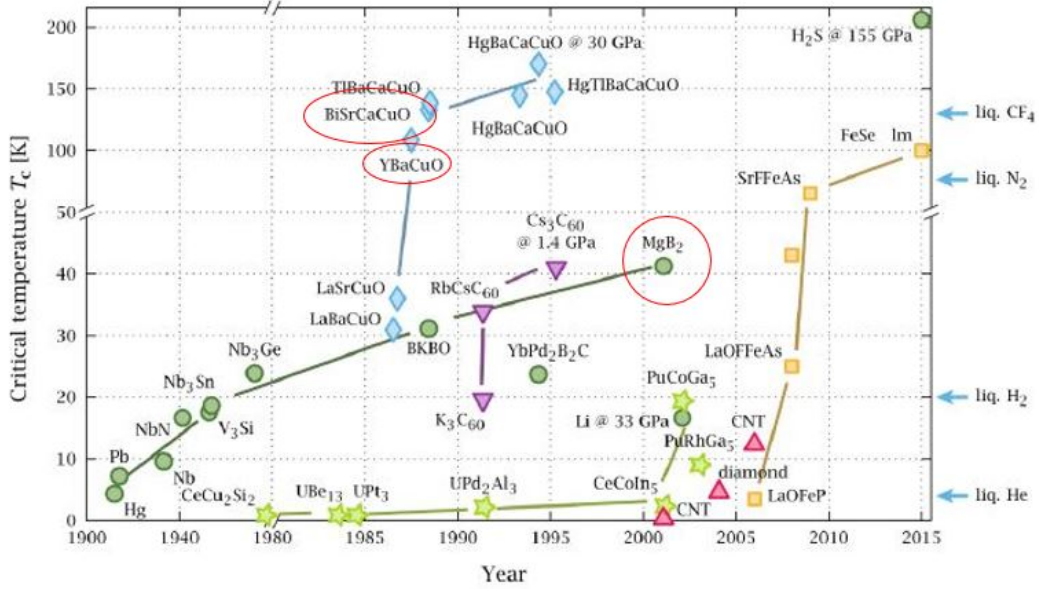


Figure 2.9: Discovery of HTS material. Circled in red, some of the most important HTS superconductors [22].

Most of these HTS materials have a critical temperature greater than >90 K, so they can be cooled, in principle, with liquid nitrogen. However, it is a good engineering practice to operate SC at around $T \leq 50\%T_c$ with an operating current density around $(0.3-0.8) J_c$, in order to keep a safe margin in the superconducting region. Moreover, as shown in previous section 2.1.2 the performance of an SC can be significantly increased if operated at far below their critical temperature. For this reason, it is possible to cool down HTS material at 20 K, the temperature of Liquid Hydrogen [3].

2.2.2 Classification by Magnetic Field

Two different classes of SC can be recognized based on their transition from superconducting to normal (dissipative) state when subjected to an external magnetic field:

- **Type I** Superconductors;
- **Type II** Superconductors;

Type I Superconductors

Superconductors behave like perfect diamagnets for values of magnetic field lower than H_c . This means that they cannot be penetrated by any magnetic field $H \leq H_c$. In Type I SC there is a sudden transition from SC state to the normal state, their behavior is very close to the theory presented so far and they follow the already mentioned Meissner Effect. They expel the magnetic field up to the point the superconductivity is spontaneously destroyed at the critical field H_c . According to figure 2.10 it is possible to see how the magnetization M increases linearly with the external applied magnetic field, up to the point the critical field H_c is reached.

These superconductors have generally low critical fields, for this reason, they are hardly useful for applications [19].

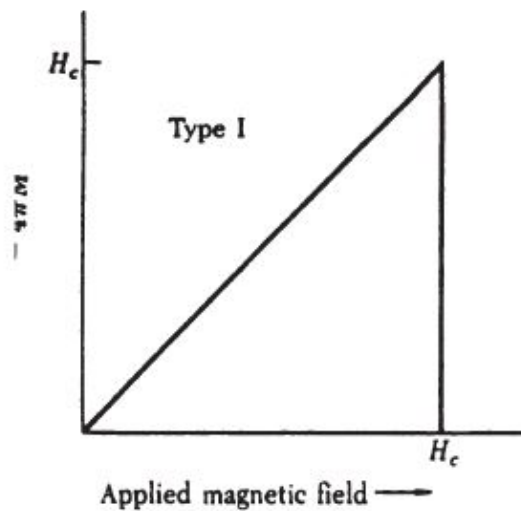


Figure 2.10: Transition from SC state to dissipative state of Type I superconductors [19].

Type II Superconductors

Type II superconductors present a perfect diamagnetic behavior up to a critical field H_{c1} and enter in a mixed state, also known as "Vortex state" for $H_{c1} \leq H \leq H_{c2}$ in [19]. In the mixed state, the external magnetic field partially penetrates the material, but some regions still present a superconducting behavior [19]. Superconductivity is lost for $H \geq H_{c2}$ when another transition from mixed state to normal state appears. The Magnetization M which contrast the external applied magnetic field is shown in figure 2.11, as it is possible to see, the M field, in the mixed state is lower than the applied magnetic field, this is consistent with the penetration of the field inside the superconductor. In the mixed state, the material appears with some "flux tubes" or "vortices" in which there is no superconducting state. The alternation of superconducting behavior (outside the tubes) in which there is no penetration and normal state (inside the tubes) creates a matrix [19] that can be appreciated in figure 2.12:

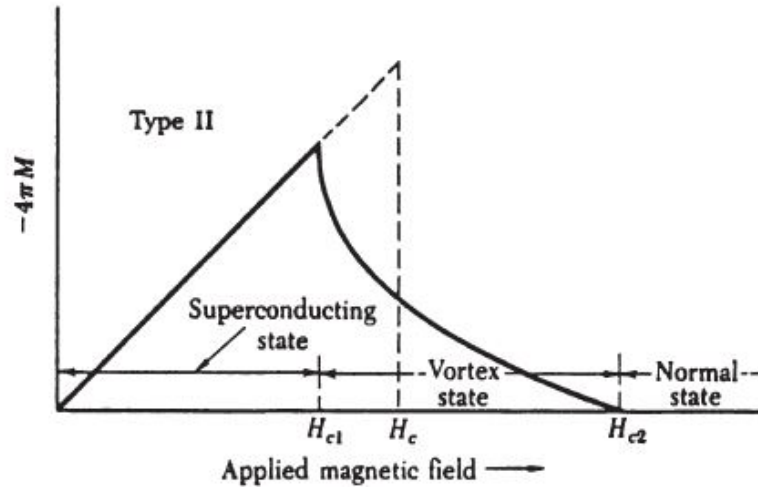


Figure 2.11: Flux pinning in the mixed state of type II Superconductors [19].

In type II superconductors the flux tubes are *pinned* by micro-structural defects and grain boundaries. As long as the flux tubes remain stuck the material shows superconductivity. This situation is protracted up to the point that the magnetic field is such that the vortices ruck up and overcome the pinning forces [19]. A visualization of the flux tubes is presented in figure 2.13.

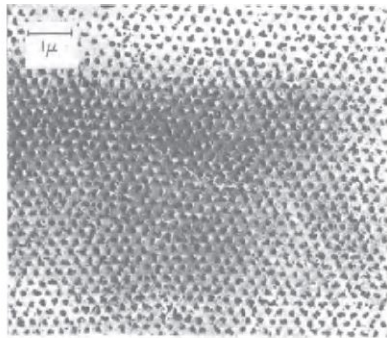


Figure 2.12: Mixed state in type II Superconductors, the dark regions represent the normal state [19].

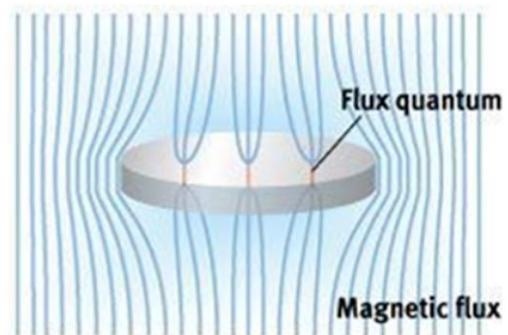


Figure 2.13: Flux pinning in the mixed state of type II Superconductors.

2.3 HTS Materials for Electrical Machine Applications

HTS materials have been identified as the ones which will allow the development of light-weight superconducting electrical machines. Currently, the main challenges in developing such machines are two:

- Reduction on the manufacturing cost of HTS;
- Reduction of ac losses;

They are both crucial for the future expansion of this type of electrical machine, many advances have been made, but many others are needed yet. The emergence of an economy of scale will be important, indeed, one key point on the reduction of manufacturing costs is the increase of the demand for this technology that is expected for years to come. On the other hand, reduction of ac losses is an important challenges on the development of light-weight electrical machines. One of the most promising techniques to reduce the ac losses of the SC is to make them under the shape of multifilament wire [23], in this way it is possible to twist the filament and therefore reduce the losses. In [12] a detailed analysis of ac losses in HTS materials is done. However, ac losses are out of the scope of this thesis, and the important thing to remember is that if the superconductors are made to work in DC and protected by a magnetic shield, they work in optimal conditions.

The four main HTS materials are BSCCO-2212, BSCCO-2223, YBCO-123 and MgB₂. However, only BSCCO-2223 and YBCO-123 wires have achieved widespread application for manufacturing practical electric power equipment [14]. In last years, even MgB₂ SC has started to be used thanks to the development of its manufacturing process.

2.3.1 BSSCO

BSSCO represent the first generation (1G) of HTS in multifilamentary tape conductors, they had several superconductor filaments embedded in silver alloy matrix which completely wound the superconducting filament:

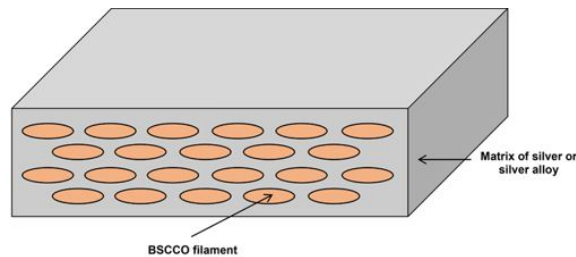


Figure 2.14: First Generation Superconductor composition [14].

There are two versions of this HTS material:

- **BSSCO-2212** $T_c = 90K$
- **BSSCO-2223** $T_c = 110K$

BSSCO-2212 has a very low current-carrying capacity in a magnetic field at 77 K. It was the first HTS material used for making superconducting wires. It can be made in the form of round wire, flat tape, cast bulk rods, blocks, and a large variety of shapes and dimensions [14],[8]. Unfortunately, Its performances are quite limited in the temperatures of interest in electrical machines. Therefore it was replaced by the 2223 version.

BSSCO-2223 HTS has a critical temperature of about 110 K. It has been manufactured in a flexible multifilament composite conductor by many manufacturers [24] in

what is named first-generation (1G) HTS. The highest value of I_c reached was 150 A in self-field at 77 K in 4mm wide tapes [14]. The first manufacturing process was successfully implemented in industrial production and was capable of producing one hundred meters length tapes. These 1G HTS tapes have become very popular in the first stages of superconducting electrical machine, here some examples [10] [25]. This material has been used for several prototypes in the past though they have some drawback which can be improved with other SC materials.

- Poor mechanical properties (bending radius)[14],[9];
- High cost[14],[9];
- High AC losses [14],[9];

All of these problems were directly related to the large amount of silver used for its manufacturing process.

2.3.2 YBCO

YBCO-123, with a critical temperature $T_c=92$ K, represents the second generation (2G) of coated superconductors. It is a material based on thin films of a yttrium barium copper oxide $YBa_2Cu_3O_7$ and it is usually made in tapes with a thickness of 0.1 mm and with of 4, 8 and 12 mm [9] [14]. The 2G wire has a significantly different architecture compared to the 1G wire. Indeed, the 2G wire does not employ expensive metal like silver and this is a crucial difference in terms of cost, and in the reduction of ac losses. It is made by several layers (fig.2.15) between which: A metal alloy substrate of 50-75 μm thick [14], Buffer layer 0-2-0.5 μm thick; A protective silver layer of a few μm and thicker copper protection and stabilization [14]. The effective superconducting layer is very thin because it has a thickness of 1 μm [14], despite this, it is responsible for the entire current carried by the tape, under specific conditions this current can be greater than 500 A.

Further in this work it will be presented the detailed characteristics of the SuperOx YBCO tape, the one used for the design of the machine [26].

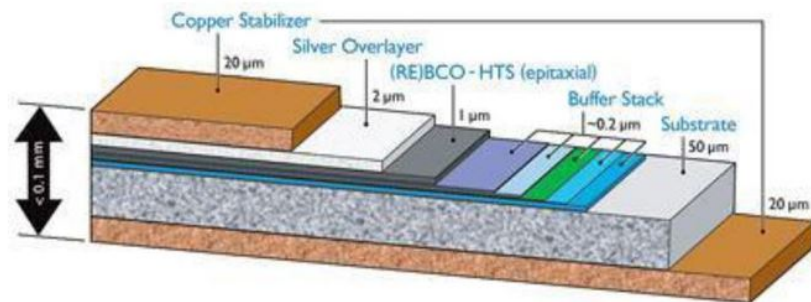


Figure 2.15: Composition of YBCO tape [26].

2G HTS YBCO tape has several advantages compared to the first generation Superconductors:

- Excellent mechanical capacity [14],[9];
- Possibility to build up to 200 m tapes[14],[9];
- Reduced manufacturing cost due to reduction of Silver[14],[9];
- Significant reduction of ac losses [14],[9];
- Possibility to sustain high current density in high magnetic field (fig.2.16)[14],[9];

In figure 2.16, an idea of the better performance of YBCO in a high magnetic field is provided, it should be remembered that in case it was used at a temperature of 20 K its performance would increase considerably. For these reasons, YBCO tapes are nowadays one of the most common used in wound field Synchronous machine [4].

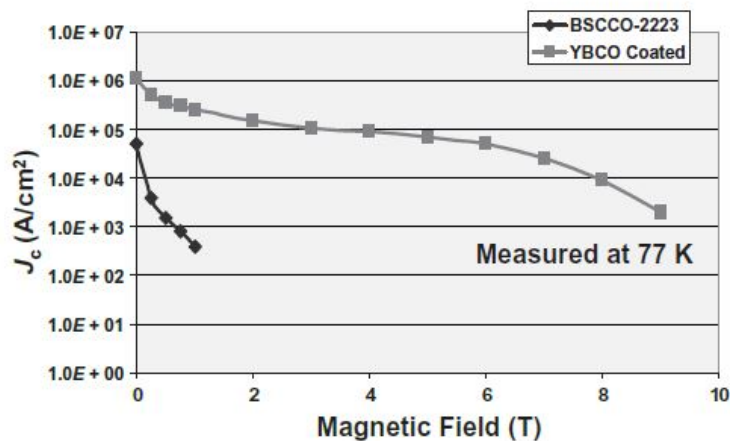


Figure 2.16: Performance Comparison in High Magnetic Field of YBCO and BSCCO SC [14].

In conclusion, a comparison of the two generation SC wire is proposed, to clarify, the engineering critical current density J_e is the critical current of the wire divided by the cross sectional area of the entire wire, including both superconductor and other metal materials. It is a parameters conventionally used by manufacturer for classifying different types of HTS materials. From table 2.1 it is possible to see the benefit of using 2G YBCO tapes with respect to 1G HTS, among which: Significant savings in purchase and so economic viability; Reduced cooling requirement in case of operating YBCO at 77 K with liquid nitrogen; Reduction of AC losses; Less wire needed for the same ampère-turns; Improved tensile strain [14].

Property	BSCCO	YBCO
Cost	\$ 50 kA/m	≤ \$10kA/m
Optimal operating Temperature	20-30 K	20- 77 K
AC loss minimization	Low	Moderate
Engineering current density J_e	10- 18 kA/cm ²	≥ 40kA/cm ²
Critical Strain	0.15% – 0.2%(adequate)	0.3%-0.5% (good)

Table 2.1: Comparison of BSCCO and YBCO for electrical machine applications [14].

2.3.3 MgB₂ Magnesium diboride

Magnesium diboride has a critical temperature $T_c=39$ K and must be operated at the temperature of liquefied Hydrogen (20 K). This HTS has been recently discovered and can be produced in multifilament form [14], (fig.2.17). This feature, together with the fact that The raw material for the fabrication is very cheap, creates a combination of advantages that can be exploited in almost all electric power equipment applications. Moreover, MgB₂ will be a valid substitute for the current LTS material involved in MRI scanner application and nuclear fusion application.

The first obvious advantage of having a low-cost superconductor is that it simplifies and accelerates the process of building prototypes, with the consequence of an increase of the demand and an economy of scale a little closer. Moreover, the particular shape allows the twisting of the filaments and this procedure drastically reduces the AC losses [23]. For this feature, MgB₂ is nowadays one of the most commonly used for the armature winding of synchronous machines [4]. A recent development from Nasa [4] uses an air-core structure with iron stator yoke, employing YBCO for the field winding and MgB₂ in armature winding, both operated at 20 K, cooled with liquid Hydrogen [4]. Further development of this HTS will allow the possibility of designing always more efficient and light-weight fully superconducting machine, that are crucial for the electrification of aviation industry (chapter 1).

Lastly, the development of multi-filamentary wire, add the possibility for SCs to be used also for HVDC transmission line, as shown in fig.2.17.

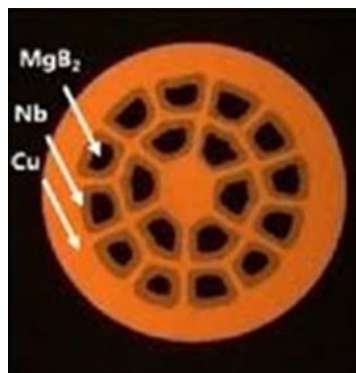


Figure 2.17: Structure and composition of a multifilamentary MgB₂ wire [23].



Figure 2.18: HVDC MgB₂ power cable developed by ASG Superconductors [27].

Chapter 3

Numerical Modeling of High Temperature Superconductors

Numerical Modeling of HTS is a powerful method for predicting SC performance in terms of electromagnetic and thermal behavior. In the last years, an expansion of this activity is started and, predictably, numerical modeling through FEM simulation will gain always more value and attention. Since HTS could be of interest for several electric power equipment applications, the importance of having useful tools for predicting their performance is crucial [28]. Numerical modeling of superconductors allows predicting their behavior even in complex geometries for which it would be difficult to study an analytical solution [29]. Moreover, depending on the level of accuracy that someone wants to reach, computational time could become too high, because of the highly non-linear relation between the electric field and the current density [30]. A general review on the most common methods for modeling HTS is presented, in this chapter, especially, it will be explained how to implement the T-A formulation [31]. It must be said that these methods can be used for general-purpose, calculating AC losses in different working conditions (Sinusoidal, linear ramp transportation current), estimation of the produced magnetic field, and for current density distribution [30]. However, the goal of this chapter is to understand which is the most effective way to simulate superconductors considering different options. In particular, the more accurate T-A formulation will be implemented in the FEM software COMSOL on two case studies; The first regards the simulation of a simple magnetic circuit, the second regards the simulation of superconducting windings in air. The results of the T-A formulation will be compared to results coming from two simplified simulations in which a constant current density is implemented in equivalent structures: Equivalent lines and equivalent bulk. On the basis of the results obtained through the case studies, it will be provided the most effective way to simulate superconductors in the electrical machine proposed in chapter 4.

3.1 Constitutive Relationship: Power Law

Independently of the adopted numerical method, mathematical formulation, or software implementation, one has to select a proper constitutive relationship between the electric field E and the current density J for describing the superconductor's electrical

behavior [28]. In this chapter, a continuous **Power Law** relationship will be used [28].

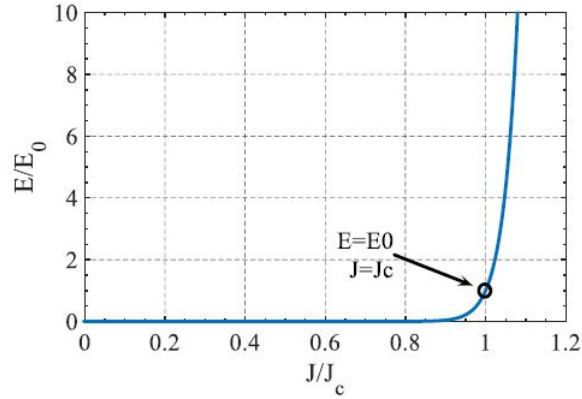


Figure 3.1: Power Law.

Described by:

$$E = E_0 \left(\frac{J}{J_c} \right)^n \quad (3.1)$$

The Power Law has a strong non-linear behavior and it is crucial for modeling HTS. This non-linearity is a problem in terms of computational time, moreover, it is necessary to take into account also the dependence of the J_c from other parameters like amplitude and orientation of the magnetic Field, as well as the temperature. These operations drastically increase the computational time, for this reason, it is necessary to do find a compromise between accuracy and computational time needed. In the following, an overview of the detailed electromagnetic-thermal modeling of HTS is provided.

3.1.1 Definition of J_c

Electromagnetic Modeling

There are several models which describe the critical current density as a function of the applied magnetic field. Firstly, let's consider the parameter J_{c0} as the critical current density estimated at 0 K and without external applied Magnetic field to the SC, so J_{c0} (0 K, self-field). Here are reported the most commonly used in the field of the electrical machine:

- **Bean Model**

In the Bean model, the easiest to understand but also the most approximated one, the dependence from the applied magnetic field of the critical current density is neglected, so it is assumed that the critical current density of the SC material

is constant and equal to the one provided by the manufacturer, under the specific conditions mentioned above.

$$J_c = J_{c0} \quad (3.2)$$

- **Kim Model**

The Kim model is the most consolidated for electrical applications, it is the best compromise between accuracy and calculation times. To follow:

$$J_c(B_{sc}) = \frac{J_{c0}B_0}{B_0 + |B_{sc}|} \quad (3.3)$$

Where B_0 is the field that halves the critical current density J_{c0} , its value is constant and depends on the material, while B_{sc} is the total magnetic field experienced by the SC (sum of the applied magnetic fields and the self-field). To remember that equation 3.3, can be expressed also in terms of magnetic field H , since the permeability of the superconductor is assumed to be $\mu_r = 1$.

- **Modified Kim Model**

There's another version of the Kim model that explicit the different contribution to the J_c of the parallel and perpendicular component of the magnetic field to the SC surface, expressed as a function of magnetic flux density (Relative permeability of SC is 1):

$$J_c(B) = \frac{J_{c0}}{1 + \frac{\sqrt{k^2 B_{//}^2 + B_{\perp}^2}}{B_0}} \quad (3.4)$$

where k is a constant depending on the material.

Thermal Modeling

The dependence of the critical current density from the temperature is described by the following equation:

$$J_{c0}(T) = J_{c0}(0K) \left[1 - \left(\frac{T}{T_c} \right)^2 \right]^{\frac{3}{2}} \quad (3.5)$$

Where $J_{c0}(0K)$ is the reference value provided by the manufacturer, estimated at 0 K, or to another reference temperature, for example 77 K, while T is the operating temperature of the SC.

Based on what has been said so far, it is possible to merge the thermal modeling along with the Kim model to have a general characterization of the critical current density as a function of the operating conditions, so $J_c(B, T)$.

However, Modeling completely the J_c as a function of the operating condition requires large computational time. In a time-dependent study, **for each time step**, the solver has to acquire both the value of the operating temperature T and the internal magnetic field and adjust the value of J_c before applying the power law. This procedure can become time demanding, and sometimes it is not worth it depending on what the focus of the study is.

It is possible to make some hypotheses that can simplify the model. For instance, if the hypothesis to cool down the SC constantly and uniformly is reasonable, it is possible to neglect the dependence of the critical current density from the temperature. In the same way, if an efficient shield protects the SC from an externally applied magnetic field, it is possible to neglect even the dependency from magnetic field. While the feasibility of the self-field is intrinsic to the definition of J_c

3.2 Modeling of HTS Tapes

In this section, a review of the different methods to simulate tapes with FEM is provided. Then, the two case studies will be discussed in order to define the most suitable strategy to model SC in EM environment, on the basis of their macroscopic effect.

3.2.1 Modeling of a Single Tape

For the modeling of the SC, it has been decided to use the Finite Element software Comsol Multiphysics. YBCO tapes have been used for the case studies (figure 4.14). Unfortunately, Modeling a 0.1 mm thick tape with several layers in the inside is a big problem for the meshing. As it is possible to understand from figure 3.3, employing such a mesh involves too many elements and this means that the computational time drastically increase. For this reason, some modeling strategy are needed.

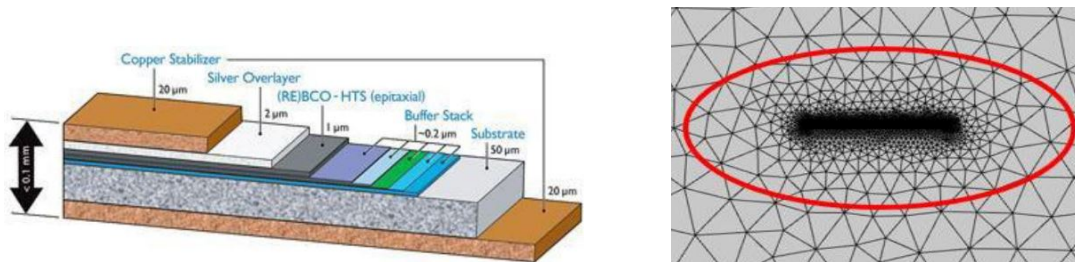


Figure 3.2: YBCO tape composition [26]. Figure 3.3: Mesh building for a 0,1 mm thick tape.

There are two commonly accepted methods for modeling and simulating a single HTS tape. In general, when speaking about modeling of HTS tape, only the superconducting layer is considered because when there is the superconducting state, the resistance of the SC layer is much smaller than the resistance of the "surrounding

layer", in this way $R_{surrounding} \gg R_{HTS}$. The first method aims to model the superconducting layer as an equivalent line (figure 3.4), with equivalent resistivity and current density. These two equivalent parameters are obtained imposing the same current and losses of the equivalent line and the real superconducting layer. The second method, similarly, aim to substitute the SC layer as an equivalent bulk (figure 3.5) while maintaining the same losses and the current carried. In this second case, the equivalent current density will coincide with the engineering current density J_e . In figure 3.4, ρ' stands for the resistivity of the equivalent thin layer, while $j[\frac{A}{mm}]$ is the equivalent current density of the thin layer. In figure 3.5 the terms ρ'' is the resistivity of the equivalent bulk with which the real superconducting layer is modeled and $J'[\frac{A}{mm^2}]$ is the equivalent current density of the bulk.

1. Modeling of HTS tape as an equivalent line with ρ' and $j[\frac{A}{mm}]$

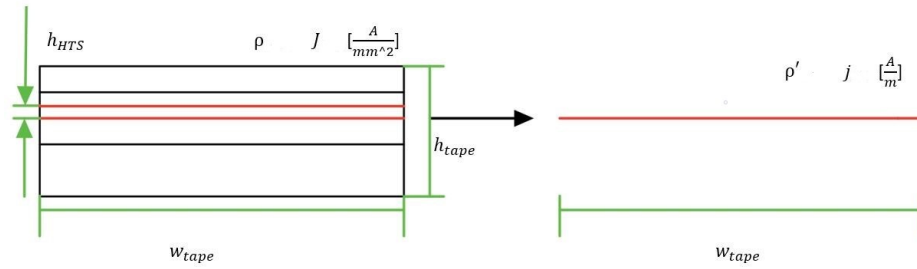


Figure 3.4: HTS tape as an equivalent line.

2. Modeling of HTS tape as an homogenized bulk with ρ'' and $J'[\frac{A}{mm^2}]$

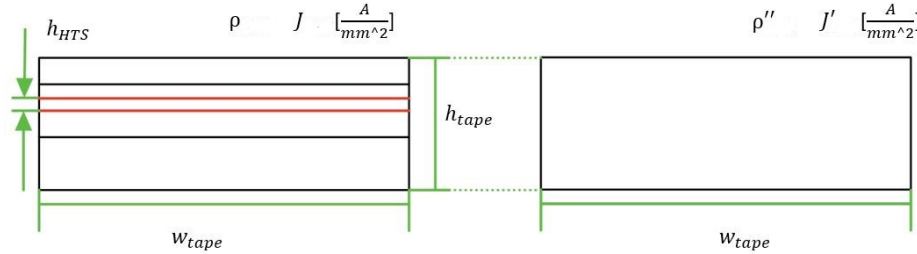


Figure 3.5: HTS tape as an equivalent bulk.

Firstly, the calculation for obtaining the parameters for the equivalent thin layer are shown in the following procedure:

With reference to figure 3.4, the cross section of the superconducting layer is the following:

$$S_{HTS} = w_{tape} h_{HTS} \quad (3.6)$$

Where h_{HTS} is the thickness of the real superconducting layer.

As mentioned before, the equivalent parameters are obtained assuming equal the total transportation current and the losses. The current carried by the real superconducting

layer can be expressed as follow:

$$I_{HTS} = JS_{HTS} \quad (3.7)$$

While the total transportation current of the equivalent thin layer is expressed in equation 3.8.

$$I_{HTS} = jw_{tape} \quad (3.8)$$

Where j is the current density of the equivalent thin layer.

Assuming equal the two currents, it is possible to evaluate the expression of the equivalent current density of the thin layer:

$$I_{HTS} = J w_{tape} h_{HTS} = j w_{tape} \quad (3.9)$$

$$j \left[\frac{A}{mm} \right] = J h_{HTS} \quad (3.10)$$

Where J is the current density of the real superconducting layer.

The equivalent resistivity is obtained assuming equal the losses. Again, the losses of the real superconducting layer (equation 3.11) and of the equivalent thin layer (equation 3.12) can be expressed as follow:

$$P_{HTS} = \rho J^2 w_{tape} h_{HTS} l_{HTS} \quad (3.11)$$

$$P_{HTS} = \rho' j^2 w_{tape} l_{HTS} \quad (3.12)$$

Where, w_{tape} is the width of the entire tape and l_{HTS} is the length of the tape.

Assuming equal the losses, and substituting the expression of the current density of the equivalent thin layer, calculated in equation 3.10, in equation 3.12, the resistivity of the equivalent thin layer can be calculated:

$$P_{HTS} = \rho J^2 w_{tape} h_{HTS} l_{HTS} = \rho' j^2 h_{HTS}^2 w_{tape} l_{HTS} \quad (3.13)$$

$$\rho' = \frac{\rho}{h_{HTS}} \quad (3.14)$$

The same procedure is applied for the modelization of the real superconducting layer as an equivalent bulk.

With reference to figure 3.5 Let's assume again the transportation current of the superconducting layer $I_{HTS} = JS_{HTS}$, and its cross section $S_{HTS} = w_{tape} h_{HTS}$, the total current carried by the equivalent bulk can be expressed as follow:

$$I_{HTS} = J' w_{tape} h_{tape} \quad (3.15)$$

Where h_{tape} is the thickness of the entire tape and J' is the current density of the equivalent bulk, which is the objective of the calculation.

Imposing the currents to be the same, it is possible to obtain the following result:

$$I_{HTS} = J w_{tape} h_{HTS} = J' w_{tape} h_{tape} \quad (3.16)$$

$$J' = J \frac{h_{HTS}}{h_{tape}} \quad (3.17)$$

Lastly, the losses of the real superconducting layer are expressed in equation 3.11, while the losses of the equivalent bulk are:

$$P_{HTS} = \rho'' J'^2 w_{tape} h_{tape} l_{HTS} \quad (3.18)$$

Where ρ'' is the resistivity of the equivalent bulk.

Imposing to be equal the losses, and substituting equation 3.17 in equation 3.18, it is possible to obtain the expression of the resistivity of the equivalent bulk ρ'' :

$$P_{HTS} = \rho J^2 w_{tape} h_{HTS} l_{HTS} = \rho'' \left(J \frac{h_{HTS}}{h_{tape}} \right)^2 w_{tape} h_{tape} l_{HTS} \quad (3.19)$$

$$\rho'' = \rho \frac{h_{tape}}{h_{HTS}} \quad (3.20)$$

The results of the calculation needed for the estimation of the equivalent parameters are shown in the following tables:

- Modeling of HTS tape as an equivalent line;

Real Tape	tape as a thin layer	Eq. parameters
$I_{HTS} = JS_{HTS}$	$I_{HTS} = j w_{tape}$	$j = J h_{HTS}$
$P_{HTS} = \rho J^2 w_{tape} h_{HTS} l_{HTS}$	$P_{HTS} = \rho' j^2 w_{tape} l_{HTS}$	$\rho' = \frac{\rho}{h_{HTS}}$

- Modeling of HTS tape as an homogenized block;

Real Tape	tape as a bulk	Eq. Parameters
$I_{HTS} = JS_{HTS}$	$I_{HTS} = J' w_{tape} h_{tape}$	$J' = J \frac{h_{HTS}}{h_{tape}}$
$P_{HTS} = \rho J^2 w_{tape} h_{HTS} l_{HTS}$	$P_{HTS} = \rho'' J'^2 w_{tape} h_{tape} l_{HTS}$	$\rho'' = \rho \frac{h_{tape}}{h_{HTS}}$

3.2.2 Modeling of a Stack of Tapes

Homogenization

Once the model for a single tape is built, the model for a stack of tapes is obtained repeating over space the same procedure [32].

Similarly to the case of the single tape, due to the thickness of the SC layer, for the modeling and simulation of the stack, anything that is not the superconductor is part of the "surrounding".

There are several methods for modeling a stack of tapes, all aiming to reduce computational time while maintaining acceptable accuracy [30]. In this section, the focus will be on one of the most common: **Homogenization**.

Homogenization consists on the transformation of a set of tapes into a bulk with an "equivalent" current density applied to all the surfaces shown in figure 3.6. There are some conditions to be respected to apply Homogenization:

- Evenly distributed tapes;
- Identical tapes;
- Constant permeability;

It is important that the distribution of tapes along the "equivalent homogeneous bulk" is uniform, because otherwise, the external effect in terms of magnetic field would be wrong and far from the reality. Moreover, the permeability of a superconductor is generally assumed equal to $\mu_r = 1$. the stack of tapes is transformed into a homogeneous bulk with isotropic properties. [33].

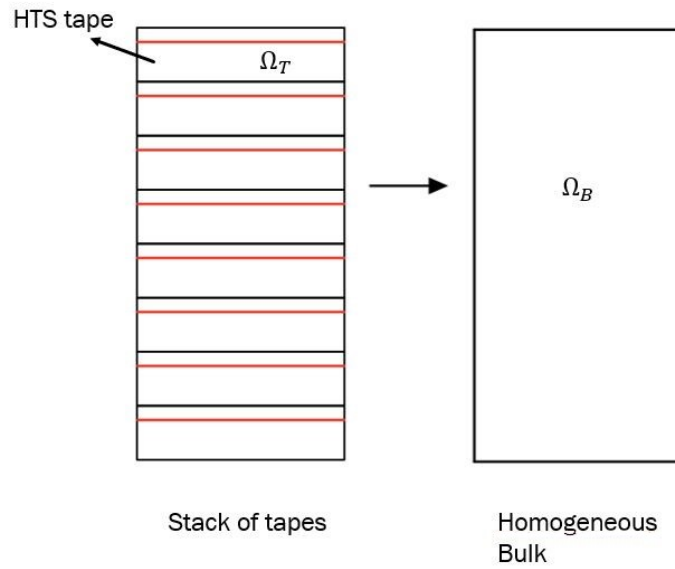


Figure 3.6: Stack of tapes as an equivalent homogeneous bulk: Homogenization.

The equivalent current density to impress to the homogenized bulk is given by the constraint to the transportation current (the current that is carrying each tape), which obviously must be equal to the sum of all the transportation currents of each tape.

$$N_T I_T = N_T \iint_{\Omega_T} J_T d\Omega_T = I_B = \iint_{\Omega_B} J_B d\Omega_B \quad (3.21)$$

3.3 FEM Implementation

In this section, some of the most common numerical models based on FEM are proposed, all of them use different forms of *Maxwell equations* with different state variable. The general aim is to reduce the overall computational time while maintaining the best accuracy possible. This is particularly important for the evaluation of the distribution of the current density in the tapes. This section aims to present some of the methods and to implement one of them: the T-A formulation, that is reasonable to expect will play an important role in the near future [31].

3.3.1 H Formulation

The H Formulation is the most consolidated and largely accepted formulation for simulating HTS material up to the point that is considered as the reference for the development of other formulations. When a new formulation is studied, a comparison between the new and the H is done for the validation [30] [31]. As the name says, The magnetic field \mathbf{H} is used as the state variable. The transportation current is applied through the integration of the current density over the cross-section of the superconductor (equation 3.25) [31].

The governing equations are the maxwell equations expressed as a function of H:

$$\nabla \times [\rho \cdot \nabla \times H] = -\mu_0 \frac{dH}{dt} \quad (3.22)$$

$$J = \nabla \times H \quad (3.23)$$

$$\nabla \cdot B = 0 \quad (3.24)$$

The transportation current is obtained through integration:

$$I_t = \iint_{\Omega} J d\Omega \quad (3.25)$$

For convergence in Comsol simulation, there is one important thing to take into consideration, the solver runs all of these equations for calculating the parameter of interest, in the case of H Formulation the output from Maxwell equations is the current density J. It is necessary to implement in Comsol the following version of the Power Law: General Power Law expression:

$$E = E_0 \left(\frac{J}{J_c} \right)^n \quad (3.26)$$

Power Law expressions needed for Comsol convergence:

$$\rho(J) = \frac{E_0}{J_C + eps} \left(\frac{J}{J_c}\right)^{n-1} \quad (3.27)$$

$$E = \rho J \quad (3.28)$$

The motivations for this change are two, the first is due to the nature of the equation, the output from the Maxwell eq. is J , so it must be the input for the power law. The electrical field is calculated subsequently through equation 3.28. The second change is the addition of a very small number of the order of 10^{-5} called *eps* that aims to avoid numerical problems during the calculation.

3.3.2 A Formulation

All of the considerations done up to now about H Formulation can be repeated for the A formulation, indeed they only differ from the state variable used for calculating the same parameters of interest for the tape: J , E , ρ . This formulation is less used for the FEM simulation of the superconductors through the power law, indeed, as explained in [29], the H Formulation is more reliable than the A Formulation since many attempts to implement A formulation have proved to be not accurate. However, A-formulation works very good for simulation of electrical machines environment. The governing equation of this formulation is the following [31];

$$\nabla \times \frac{1}{\mu_0} \nabla \times A = J \quad (3.29)$$

$$B = \nabla \times A \quad (3.30)$$

$$\nabla \cdot B = 0 \quad (3.31)$$

As regards the implementation of the Power Law with A Formulation, the only difference with H-formulation is the order in which the same parameters of interest are calculated. From The Vector Potential, the Electric Field is the first parameter that is calculated, for this reason, the resistivity of the SC material must be explicitated as a function of E . The actual current density J is calculated subsequently through the equation 3.33:

$$\rho(E) = \frac{E_0}{J_c + eps} \left(\frac{E}{E_0}\right)^{\frac{n-1}{n}} + eps \quad (3.32)$$

$$J = \sigma E \quad (3.33)$$

Also in this case, a small value ϵ is added to the expression for avoiding numerical problem due to the inversion of $\sigma = \frac{1}{\rho}$.

An interesting application of this formulation is explained in [29], in which the possibility of combining the two formulations, H and A in a superconducting electrical Machine model is evaluated. **The H-A formulation** is very interesting because it allows to divide the region where there are SC, in which the H formulation works optimally, and another region in which there is iron, copper, and air, this type of environment is easy to implement with the A-form. The possibilities of this method are great but require an accurate study of the boundary condition that must be implemented to ensure continuity of the perpendicular component of the magnetic field. Anyway, in this section, the H-A formulation won't be treated in more detail, since another method has been used for HTS simulation in the case studies.

3.3.3 T-A Formulation

The T-A Formulation is a relatively new and promising technique that allows the reduction of the overall computational time with respect to the other formulations, moreover, it has also proved to be versatile for more in-depth analyses, for example for the evaluation of losses [30][31]. It can be used both for simulating single or even stack of tapes through homogenization technique. [29] [33].

Through the T-Formulation, the current density distribution of the tape can be evaluated, subsequently, this current density distribution can be used as an input for the A-Formulation [34].

In particular, the current vector potential \mathbf{T} is defined in the superconductors and used as a state variable to calculate the current distribution along the tape, while the magnetic vector potential \mathbf{A} is defined in all domains, so both in SC and in Non-SC regions, and solved through the A Formulation like shown in figure 3.7:

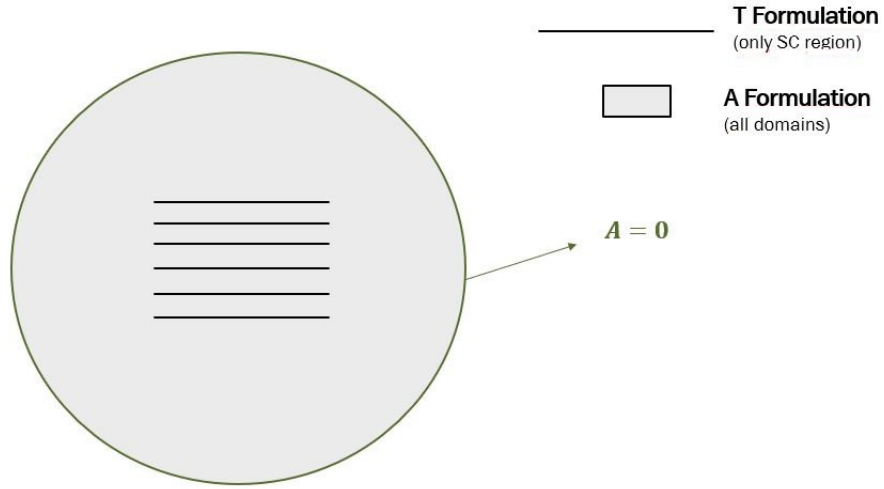


Figure 3.7: T-A implementation to the domains.

The governing equations of each of the indicated regions are the following:

- **T Formulation:**

$$J = \nabla \times T \quad (3.34)$$

$$\nabla \times [\rho \cdot \nabla \times T] = -\frac{\partial B}{\partial t} \quad (3.35)$$

where ρ is the resistivity of the superconductor.

- **A Formulation:**

$$\nabla \times \nabla \times A = \mu_0 J \quad (3.36)$$

Usually, the relative permeability of SC tapes is assumed to be $\mu_r = 1$.

The procedure is the following: The surface current density is calculated from T and it is used in the equation 3.36. Then B, obtained from equation 3.36, is used as a source term for T in equation 3.35 [31].

Theory for implementation

For the implementation, once indicated to the software which is the state variable in each region, the only important thing is to put the right constraint and the appropriate boundary conditions. In this case, the T-A formulation is implemented by imposing a set of boundary conditions through the variable T on the edges of the SC modeled as an equivalent line. Let's consider the superconducting layer of figure 3.8, the only component of the current density different from zero is the one on the z -axis. Under the hypothesis of uniform current density over the thickness of the superconductors, J_z can be evaluated as follow:

$$J_z = \frac{dT_y}{dx} - \frac{dT_x}{dy} \quad (3.37)$$

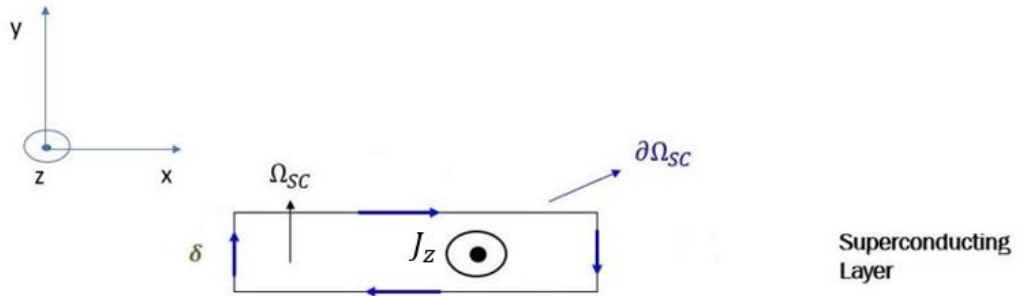


Figure 3.8: Superconducting Layer with z -axis current density.

At this point, the boundary condition to apply on the equivalent line in the FEM model, are evaluated starting by imposing the integral of the current density J_z on the cross-section of the superconducting layer equal to the transportation current:

$$i_t = \iint_{\Omega_{sc}} J_z d\Omega_{sc} \quad (3.38)$$

Substituting the equation 3.34 in J , it is possible to obtain the following expression:

$$i_t = \iint_{\Omega_{sc}} J_z d\Omega_{sc} = \iint_{\Omega} \nabla \times T d\Omega_{sc} \quad (3.39)$$

Applying the Stokes theorem, the transportation current become equal to the circulation of the potential vector T over the edge of the superconducting layer:

$$i_t = \iint_{\Omega_{sc}} J_z d\Omega_{sc} = \iint_{\Omega} \nabla \times T d\Omega_{sc} = \int T d\gamma \quad (3.40)$$

Where γ is the edge of the surface of the SC Ω_{sc} .

At this point, with reference to figure 3.9, the circulation can be explicitated in the following way:

$$i_t = \int T d\gamma = \delta[T_y(x=0) - T_y(x=w)] + w[T_x(y=\delta) - T_x(y=0)] \quad (3.41)$$

Thanks to the hypothesis of uniform distribution of current density across the thickness, $T_x(y = 0) = T_x(y = \delta)$, so equation 3.41 becomes:

$$i_t = \int T d\gamma = \delta(T_y(x = 0) - T_y(x = w)) = \delta(T_L - T_R) \quad (3.42)$$

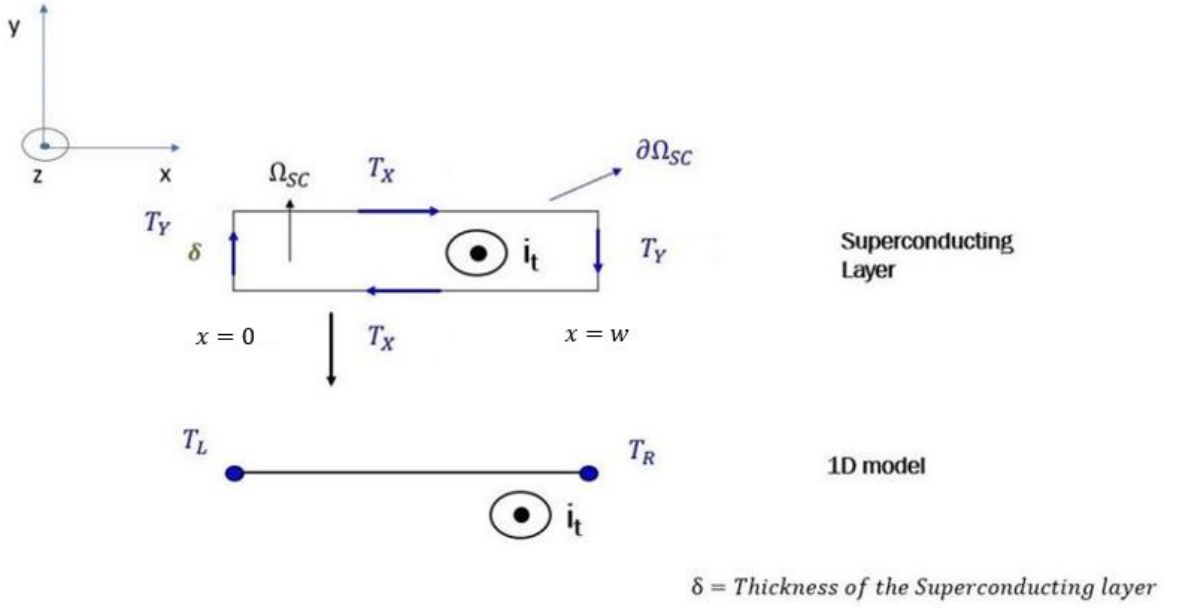


Figure 3.9: Circulation of the current vector potential T over the superconducting layer.

At this point, imposing that $T_y(x = 0) = 0$ and $T_y(x = w)$ (related to the total current carried by the tape):

$$T_y(x = 0) = T_L = 0 \quad (3.43)$$

$$T_y(x = w) = T_R \quad (3.44)$$

Substituting equations 3.43 and 3.44 in equation 3.42:

$$i_t = -\delta T_R \quad (3.45)$$

$$T_y(x = 0) = T_L = 0 \quad (3.46)$$

Consequently, $T_R = -\frac{i_t}{\delta}$ and $T_L = 0$.

At this point it is possible to implement the constraints in the equivalent line. In figure

3.10 are shown the two boundary conditions applied to the edges from T-formulation, and the equivalent current density applied along the line, calculated before in equation 3.10:

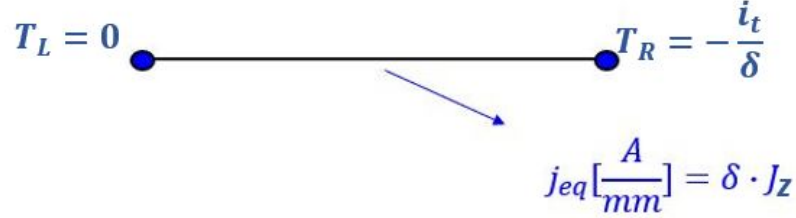


Figure 3.10: Boundary conditions to implement in Comsol Multiphysics for T-A formulation.

3.4 Case Studies

This thesis investigates superconducting electrical machines, but before doing this, it is necessary to go into detail in the simulation of superconductors and this is done through two simple case studies. The reasons are two: The first is to understand which is the best method to simulate superconductors with respect to the final objective, that is the macroscopic behavior of the magnetic flux density distribution. The second one is related to the necessity to familiarize with the magnetic field produced by superconducting windings in air.

3.4.1 Introduction to the case studies

The general principles governing conduction in superconductors differ from the ones of the ohmic conductors, the fundamental characteristic is the non-uniform distribution of current density along the superconductors and this happens both in bulk or tapes. It was crucial to understand, in the first stage, how these characteristics can affect the results in the machine and which simulation method was more accurate while maintaining reasonable computational time. For each of the following case studies, regarding a simple magnetic circuit and windings in air, it has been simulated the same transportation current with three different methods:

- Equivalent line modeled with T-A formulation;
- Equivalent line modeled with a constant current density J_{eq} ;
- Equivalent bulk modeled with a uniform current density J_B

The T-A Formulation has proven to be the fastest, among the already mentioned H and A formulation, with acceptable accuracy [31]. While simulating SC with a constant current density is a simplification that allows a drastic reduction of computational time. The first object of interest is to understand the distribution of current density along with the tape in the case of a linear ramp that saturates at 1 (figure 3.11a), in order to simulate a very fast transient and then a DC transportation current, like in the rotor

of a synchronous machine.

In figure 3.11b, an example of a stack of tapes in the air is presented for the sole purpose of showing non-uniform current density distribution. In particular the ratio $\frac{J}{J_c}$. The distribution of the current density along the tape is evaluated at steady state, under DC operation, after a linear ramp excitation of the transportation current which goes from zero to I_t very quickly. From figure 3.11b, it is possible to see that the ratio $\frac{J}{J_c}$ is not uniform along the tape. Because of the "memorization effect" of the superconductors, anytime there is a time-varying magnetic field, the induced currents want to maintain the initial condition. There are differences in the penetration length of each tape, and this is due to the interaction coming from simulating multiple tapes together. The question at this point is, does this distribution of J change the external distribution of the magnetic flux density with respect to a case in which one would consider an uniform distribution of the current density? Here come the case studies.

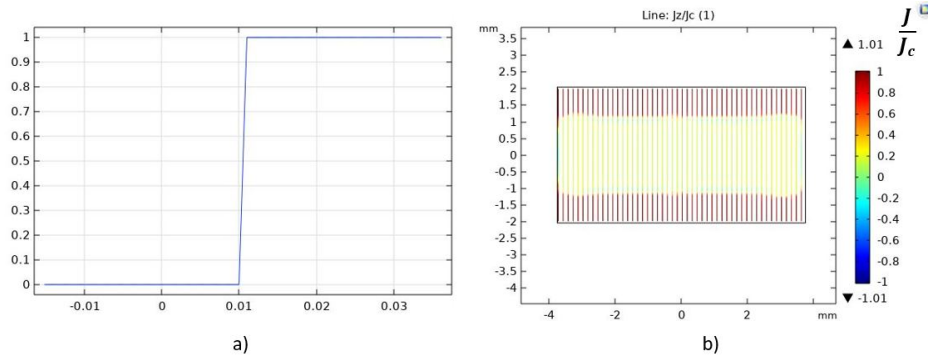


Figure 3.11: Fig.a) Linear ramp of the transportation current Fig.b)Distribution of current density and magnetic field in a stack of tapes in steady-state conditions with T-A Formulation.

3.4.2 Magnetic Circuit

To be sufficiently confident about the results, the general idea was to proceed with small steps starting from the simulation of SC in a simple structure. In this context, a simple magnetic circuit was the perfect choice for starting. For more detail, this case study refers to the HTS motor school: [32].

In this case study 10 HTS tapes carrying 150 A each are employed to magnetize an iron made magnetic circuit. To follow, a comparison between the magnetic flux density map obtained through the different methods is shown. In particular, in figure 3.12 are shown the magnetic flux density map inside the iron and the current density distribution resulting from DC operation after linear ramp excitation, which is not uniform. Moreover, in figure 3.12a, with a red arrow, it is highlighted the line in which the magnetic flux density will be compared for all of the three methods. While the actual comparison is shown in fig.3.15.

In a simplified structure with iron like this, the distribution of J doesn't affect the behavior of the magnetic flux density. This can be concluded looking at figures 3.13, and 3.14, in which, the results from T-A Formulation in terms of magnetic flux density are compared, respectively, with the simulation that employ equivalent line with constant J (3.13) and the simulation which employ an homogenized equivalent bulk with

constant J (3.14).

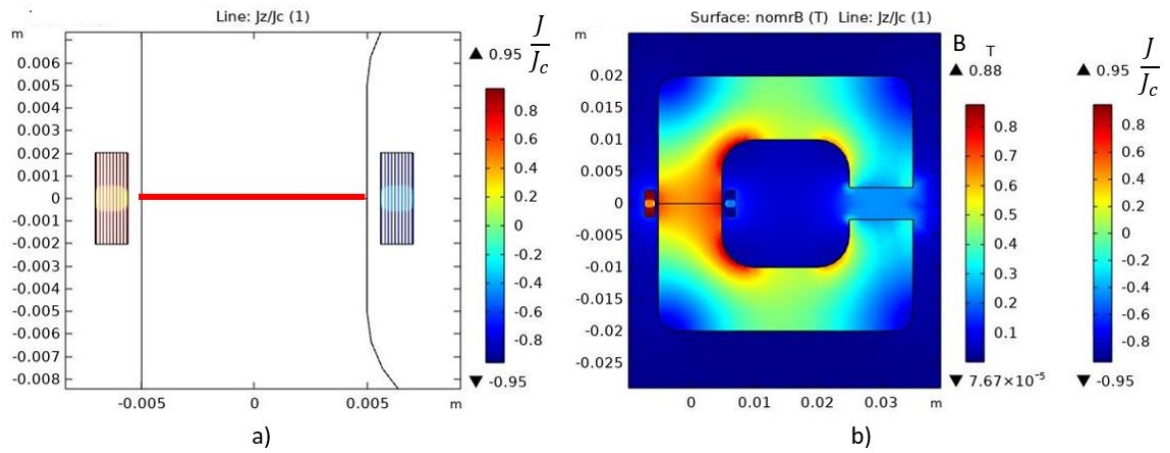


Figure 3.12: Fig.a) Distribution of current density(J/J_c) along the tape with T-A formulation; Fig.b) Magnetic Flux density map with T-A formulation.

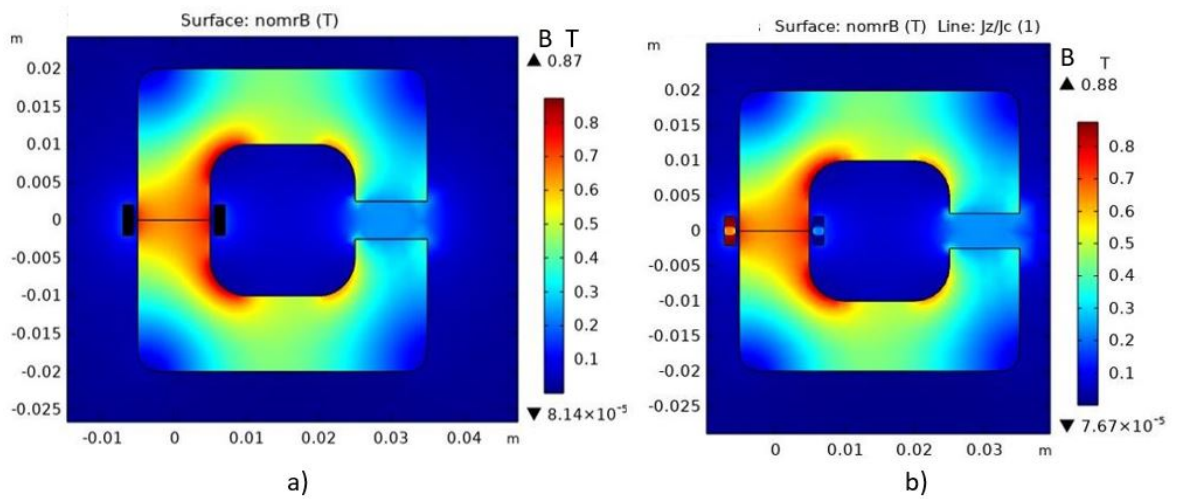


Figure 3.13: Fig.a) Magnetic Flux density with equivalent line and constant J ; Fig.b) Magnetic Flux density map with T-A formulation.

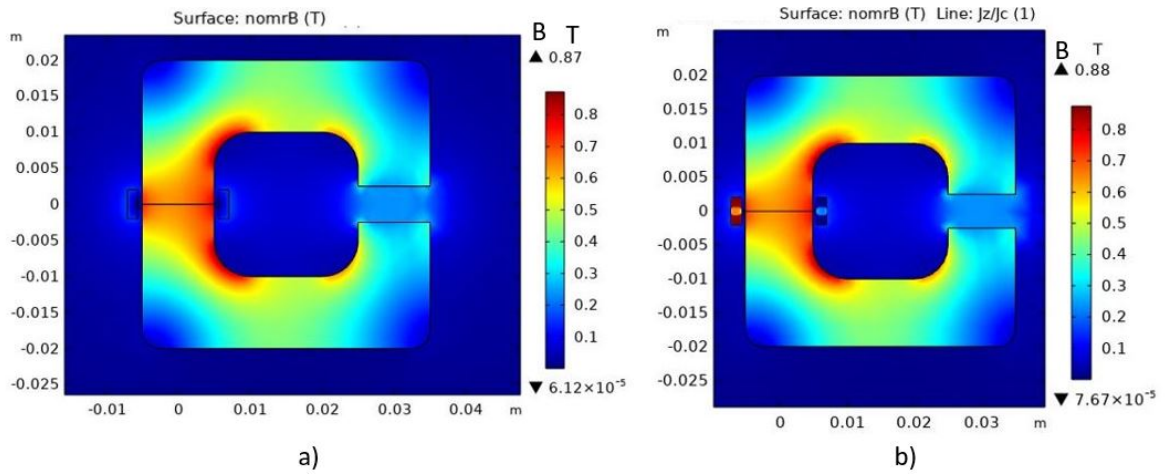


Figure 3.14: Fig.a) Magnetic Flux density with equivalent bulk and constant J ; Fig.b) Magnetic Flux density map with T-A formulation.

Lastly, the detail of the B distribution inside the column, along the line highlighted in fig3.12 is shown in figure 3.15

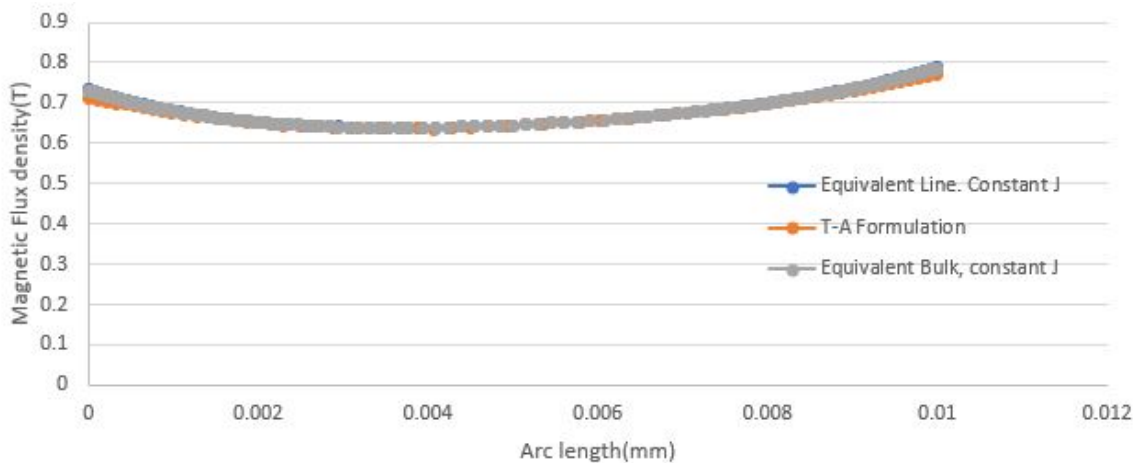


Figure 3.15: Magnetic Flux density comparison with different simulation methods along the column.

From this simple case study, it is possible to understand that, even if in reality the distribution of current is not uniform, with an iron structure that guides the flux lines, there is no difference in terms of magnetic flux density distribution along the column. From figure 3.15, it is possible to see that there is no macroscopic difference in terms of magnetic flux density in the column with the three methods, this is a first indication of the fact that in the simulation of superconductors, it could be useful to implement a uniform current density if one is only interested in the macroscopic effect.

3.4.3 Windings in Air

As stated in chapter 1, the general structure of a superconducting machine has an air-core rotor and slotless armature windings. For this reasons, it was necessary to

proceed with another case study that would allow to better understand how superconducting coils behave in air and whether it was still reasonable to proceed with a uniform current distribution. Superconducting windings made by 100 YBCO tapes in air were used, the procedure of the first case study has been repeated. Below, the comparisons of the magnetic flux density map with T-A formulation, uniform current density with equivalent line (figure 3.17), and between T-A and equivalent bulk (figure 3.18) are shown. Thanks to the YBCO tapes capability to carry up to 500 A at 20 K, it is possible to reach peak value of magnetic flux density of 2 T in air 3.16). With reference to figure 3.16, highlighted in red, the control line over which the magnetic flux density is compared, among all of the three methods, in figure 3.19.

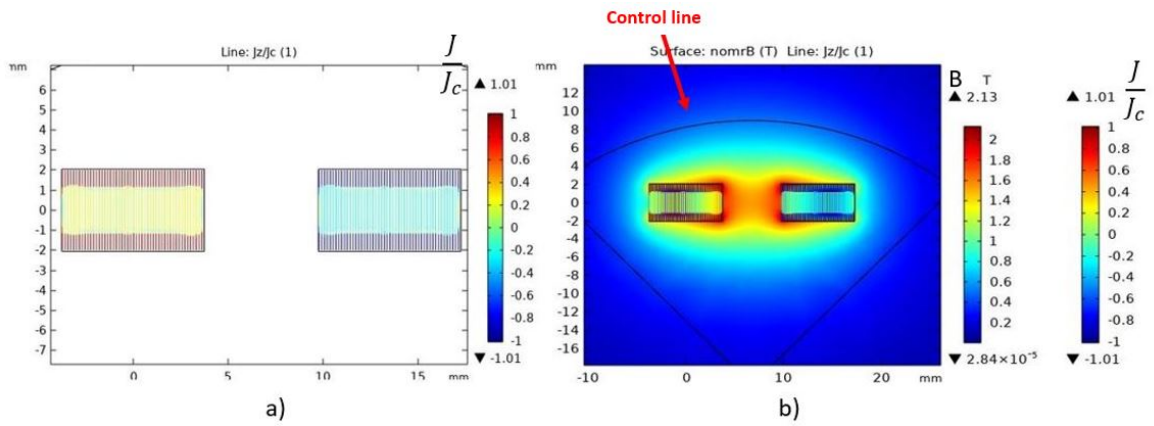


Figure 3.16: Fig.a) Distribution of current density (J/J_c) along the tapes, T-A formulation; Fig.b) Magnetic Flux density map with T-A formulation.

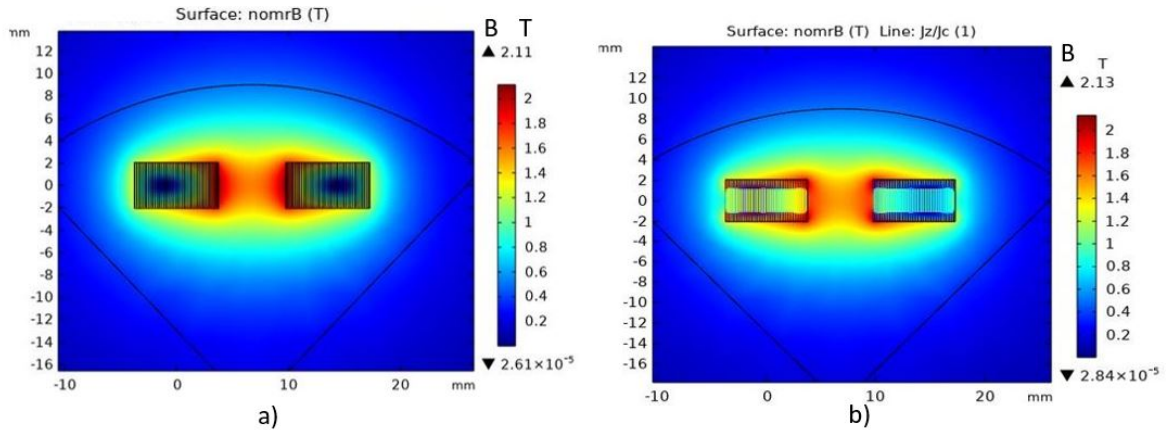


Figure 3.17: Fig.a) Magnetic Flux density with equivalent line and constant J; Fig.b) Magnetic Flux density map with T-A formulation.

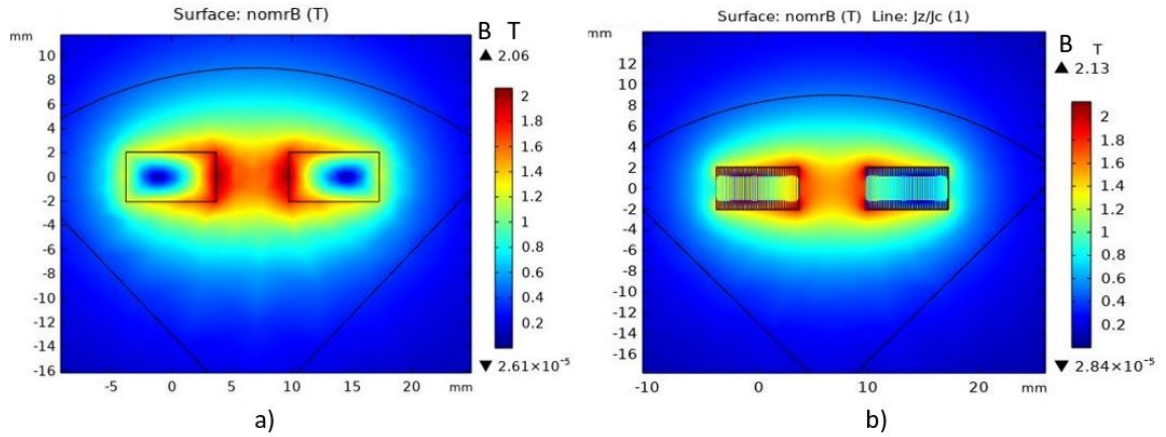


Figure 3.18: Fig.a) Magnetic Flux density with equivalent bulk and constant J ; Fig.b) Magnetic Flux density map with T-A formulation.

Moreover, simulating a superconducting winding in the air has given the chance to acquire a general idea of the distribution of the magnetic flux density along an equivalent air-gap. In particular, in figure 3.19 is shown the distribution of the magnetic flux density along an imaginary air-gap indicated in fig:3.16. From figure 3.19 it is possible to understand that not only the distribution of the magnetic flux density in an equivalent air-gap was similar in the three methods, but also it is similar to a sin-wave, which is very desirable when speaking about electrical machines.

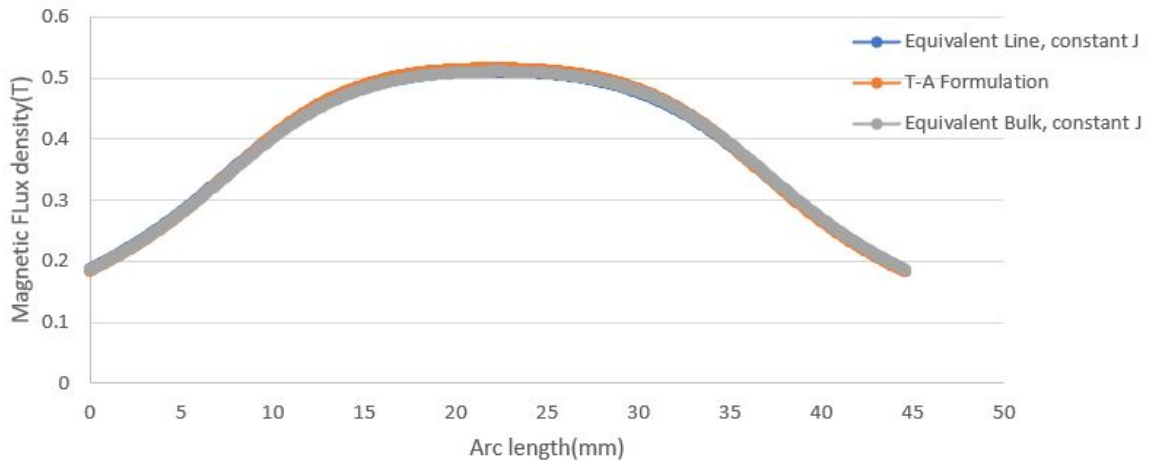


Figure 3.19: T-A implementation in Comsol Multiphysics.

The results from the second case study confirm what was emerged in the first one, there is no difference for the external magnetic field with the three different approaches: Equivalent line with T-A formulation, equivalent line with constant J and equivalent bulk with constant J . This is very useful in the simulation of superconducting electrical machines and in the first stage of the design because it allows to focus only on the electromagnetic aspects and to not take into account the internal features of the superconducting coil, which would increase the calculation times exponentially.

3.4.4 Conclusion from Case Studies

From these two very simple case studies, it is possible to conclude that there are no macroscopic differences in magnetic flux density, along the considered paths, in the case of T-A formulation or with constant current density simulation both using J along a line/equivalent bulk. Therefore, for the simulation of the superconducting windings in chapter 4, an equivalent bulk with a constant current density J , calculated through the homogenization technique was used. However, if the goal is to calculate the Losses in the tapes, accurate modeling of the current density distribution is needed [30].

In conclusion, one good way of simulating superconductors in electrical machines and evaluating the losses in the tapes could be a "multi-scale approach". It consists on performing two separated simulations: The first one concerns the simulation of the performance of the machine in which the superconductors are modeled as homogenized bulk with a constant current density. During this simulation, the magnetic flux density over a "control rectangle" that surrounds the superconducting coils is registered. Subsequently, it is possible to simulate the stack of superconducting tapes alone in another simulation in which the more accurate T-A Formulation is performed. The previously computed magnetic field in the rectangle is used as a boundary condition of the SC coils for calculating the losses in the tapes [30]. It is possible to use this strategy because, as shown in figures 3.21 and 3.22, if the tapes are tightly constrained to each other, the internal distribution of the current in the tapes does not affect the macroscopic effects along edges outside of the superconducting stack [30]. In this way, it is possible to evaluate the electromagnetic response of the machine without taking into consideration the physics of the superconductors. For a more detailed study, applying the right boundary conditions, the operating conditions of the SC in the machine are replied in another simulation in which there are only the SC tapes. The rectangle in which the magnetic field is calculated is shown in figure 3.20a. While in figure 3.20b, it is shown the same rectangle in another simulation with superconductors alone in which the boundary conditions are applied.

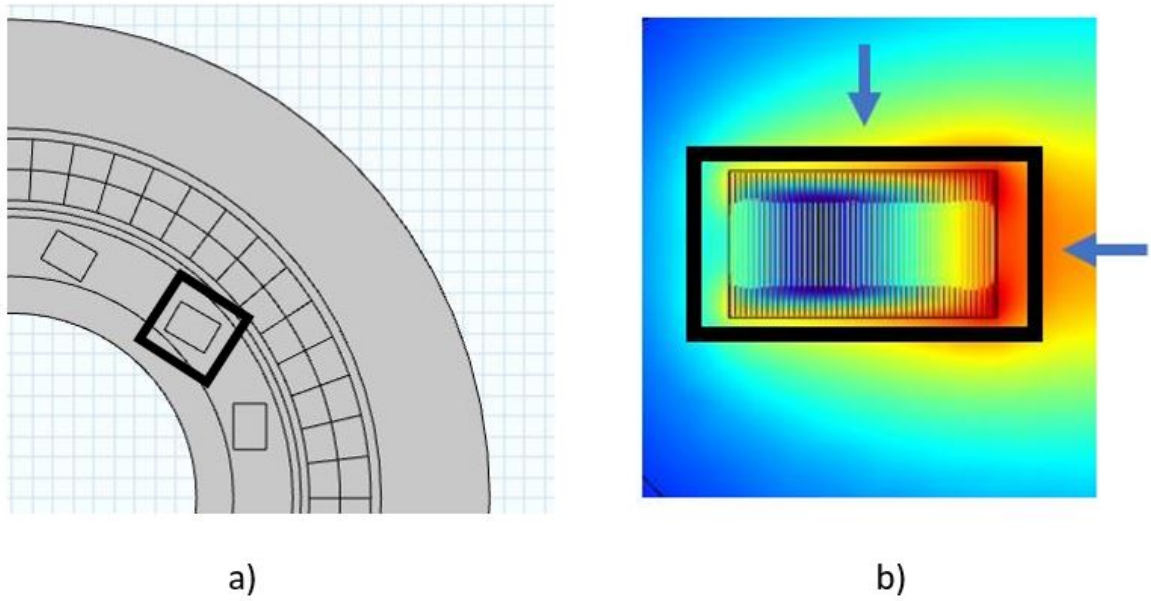


Figure 3.20: Fig.a) Rectangle over which the magnetic flux density is registered during the machine's simulation; Fig.b) Control rectangle in which the magnetic flux density is applied as a Dirichlet boundary condition when simulating Superconducting tapes alone.

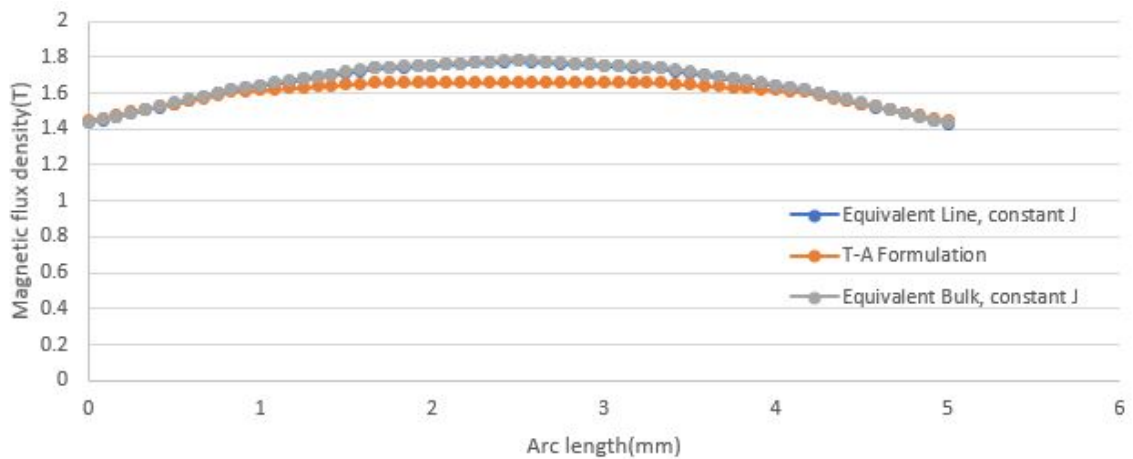


Figure 3.21: Magnetic Flux density along the vertical boundary of the "control rectangle" with the three different methods.

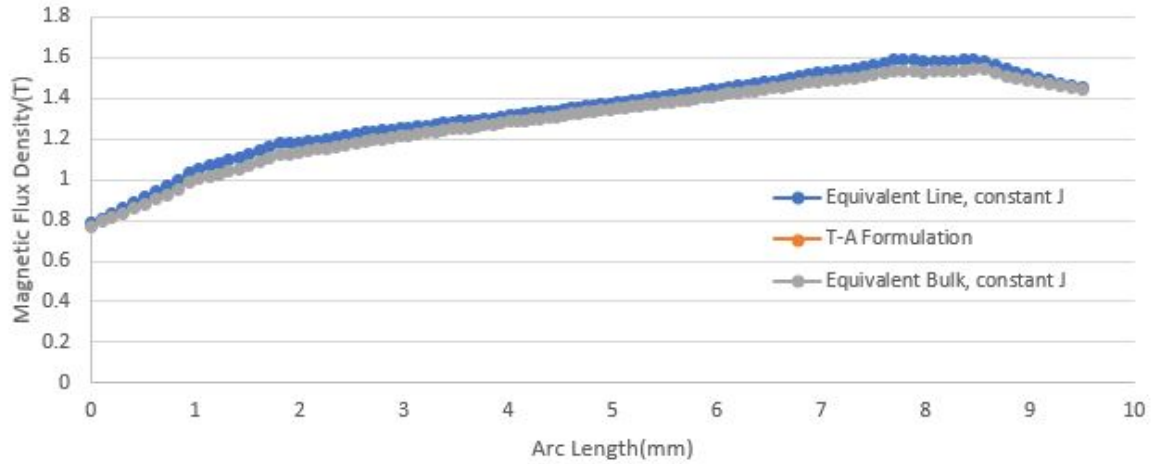


Figure 3.22: Magnetic Flux density along the horizontal boundary of the "control rectangle" with the three different methods.

This is one of the possible correct ways to proceed when simulating superconducting coils in an electrical machine, and this procedure is even more useful in the simulation of a fully superconducting machine that employs ac transportation current in the armature windings.

Since in the rotor of synchronous machine, there is a DC transport current, and since in this thesis work only a preliminary design is pursued, this approach is not employed and an **homogenization technique with constant and uniform current density \mathbf{J}** was used for the simulation of the HTS field windings in chapter 4. On the basis of the results of the case studies, this method has proved to be very accurate as well as very easy to implement in an electrical machine environment.

However, this multi-scale approach could be useful for the future.

Chapter 4

Preliminary Design of an Air-Core Synchronous Machine

In this chapter, the preliminary design of a partially superconducting synchronous machine for aircraft applications will be presented. Before going into detail about the design considerations, a general review of the characteristics of all rotor and stator topologies is done. On the basis of these considerations, an explanation will be given about the choice of the topology that best suits a superconducting electrical machine: the air-core structure. Subsequently, a design approach for air-core machines will be discussed, including the study of the behavior of the magnetic field produced by windings in air. After that, a set of equations that can be useful for a preliminary assessment are treated. Finally, in the last part of the chapter, both the preliminary design and FEM simulation of the machine will be shown. Particular attention will be given to the match between the theoretical and the simulation results. Superconductors will be used as field windings and they will be modeled with a homogenization technique and constant current density.

4.1 From Iron-Core to Air-Core Machines

In chapter 1, the advantages of the adoption of partially superconducting synchronous machines have been discussed. The general trend in the design of superconducting electrical machine is to go towards an air-core structure thanks to its many advantages with respect to the conventional one. However, in this section, the transition from the conventional machine to the air-core configuration is retraced in more detail.

4.1.1 Rotor Topologies

Magnetic-Core Rotor

The iron-core rotor can be used both in conventional and superconducting machines, it has the purpose of reducing the overall reluctance of the machine's magnetic circuit. While its use in the conventional machine is essential, in SC machine is not

mandatory. The advantage of using this type of rotor is the reduction of the required magnetomotive force to achieve the desired value of magnetic flux density. Therefore, if the focus is on minimizing the overall amount of HTS tapes, this is the topology that must be chosen. Another characteristic of a rotor-core machine is the high inertia value, this can be useful, or rather a disadvantage, depending on the application.

Air-Core Rotor

The air-core rotor topology uses a non-magnetic material, for instance, Fiber-Glass [35], for the rotating parts of the machines. This type of construction requires the largest amount of HTS tapes to produce the magnetic flux density. One disadvantage of this topology is the HTS windings support which must be designed to resist the whole torque produced by the machine. However, thanks to the absence of iron for the rotating parts it is possible to exploit most of the benefits of using HTS wire since there are no saturation limits. Lastly, the moment of inertia of air-core rotor is low and this could be an advantage for high-speed applications like aircraft applications.

Rotor Cooling concepts

The rotor-core can be operated both at cryogenic temperature (like HTS windings) and at room temperature. The cooling of only the HTS windings has the advantage of having a reduced mass to be cooled. However, in this case a sophisticated support structure is needed for HTS windings. A representation of this topology is shown in figure 4.1.

On contrary, in case of cold rotor topology, the HTS windings support is easier to build and the rotor and the windings are at the same temperature, in this case a torque transmission element connected to the ambient-temperature shaft is needed. However, cold rotor topology, shown in figure 4.2, has a larger cold mass, so it need more power for maintaining the operating temperature. Moreover, in the magnetic-rotor topology, the iron losses contributes as a heat sources to the energy balance.

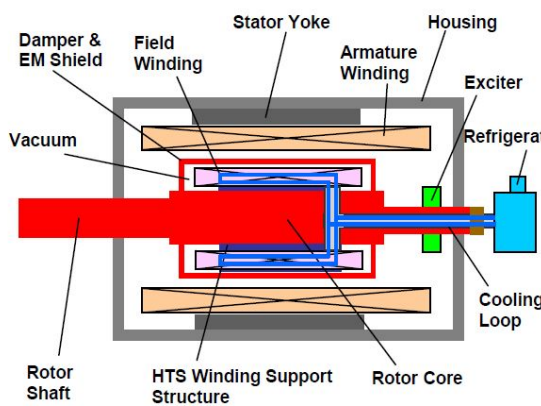


Figure 4.1: HTS Machine with warm rotor core [35].

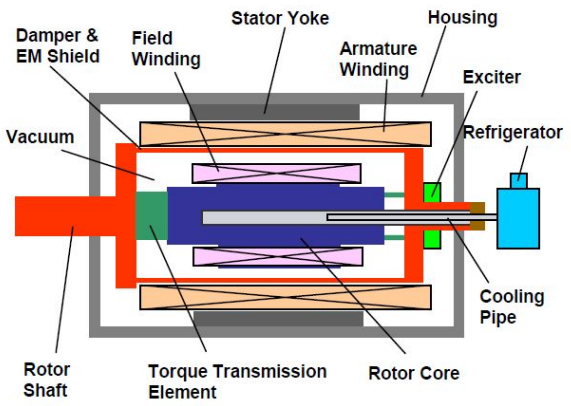


Figure 4.2: HTS Machine with cold rotor core [35].

Cooling method decision is a crucial stage for the design of a superconducting electrical machine. There are several methods to implement these cooling concepts, since this is not the focus of the thesis, the reader is referred to the following work for going into more detail [15].

4.1.2 Stator Topologies

Because of the high ac losses in HTS tapes, the utilization of superconductors in the stator is quite problematic and requires much cooling power[12][1]. Partially superconducting machine that use copper Litz wire in armature windings are a valid alternative. According to [35] HTS machines can have two different stator topologies:

- Conventional Stator;
- Non-Magnetic teeth or Slotless Stator;

Conventional Stator

The advantages of having magnetic teeth are well known in the world of electrical machine [36], the teeth work as a support structure for the copper windings and as a guide for the flux coming from the rotor to the stator yoke (fig.4.3a). The problem of this stator design for a superconducting electrical machine is the limitation given by the saturation of the iron, which would cancel the benefit of using HTS field windings. In this case, the only advantage of employing superconductors in the rotor would be increased efficiency thanks to the zero losses in rotor windings. But considering the cost of HTS and the cooling structure, it may not be worth it. For these reasons, a conventional stator with iron teeth may not be the best choice when speaking about superconducting machines. Indeed, non-magnetic teeth or slotless configuration are the most commonly used configurations for stator design of partially superconducting machine [4].

Non-Magnetic teeth or Slotless Stator

To avoid the limitation of the saturation of the iron, it is possible to design a stator topology that employs non-magnetic teeth with the only purpose of supporting the structure [35]. With this configuration (figure 4.3 b.), higher values of magnetic flux density, and voltage values are achievable. Another important benefit of using non-magnetic teeth is the elimination of the harmonics due to the slot. The only problem with this configuration is that the copper windings are not shielded and there is a proximity effect that must be taken into consideration in the later stages of design. In order to reduce the problems of this effect, and in general, to reduce circulation currents, copper Litz wire can be used in the stators of partially superconducting machines.

There is another stator topology that it is possible to exploit if the concept of non-magnetic teeth is pushed to the limit, the *Slotless* configuration (figure4.3 c.) as explained in [35]. With this stator topology, it is possible to achieve an extremely high value of the electrical loading while maintaining the same level of utilization for the

copper thanks to the greater space available [37]. Of course, a sort of support structure is needed and it needs a very accurate mechanical design because the armature windings are subjected to high electromagnetic force. To notice that in the case of magnetic teeth configuration the electromagnetic force is absorbed by the slot. Again, thermal studies are not the focus of this thesis, however, such structures of the stator open the field for so many considerations, for example:

- To use a greater amount of copper thanks to the available space while maintaining the same utilization, and the same cooling;
- Exploit a greater utilization of the copper thanks to advanced cooling system that can be exploited thanks to the greater available space;

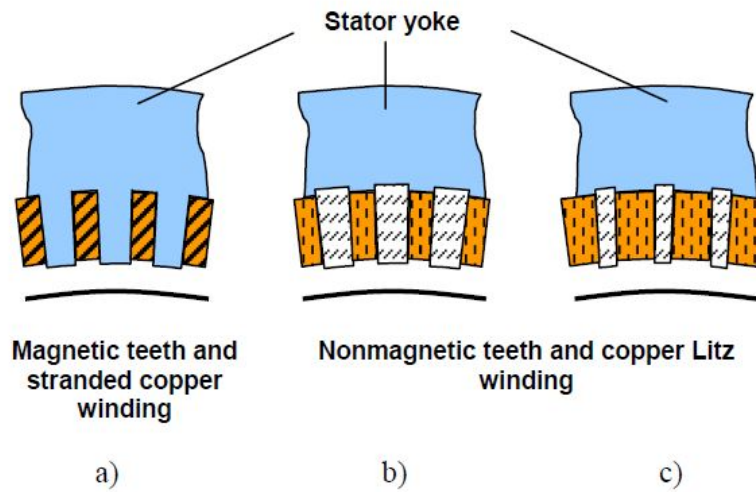


Figure 4.3: Different stator topologies of HTS machines, a) Conventional stator, b) Non-Magnetic teeth, c) Slotless stator.

Thanks to the reduction of the amount of iron in the machines with superconductors, the synchronous Reactance is significantly lower with respect to a conventional Machine. With the massive Magnetomotive force that HTS field windings can produce, it is possible to compensate the greater reluctance of the whole magnetic circuit, and this results in the benefit of having more stability margin and a lower load angle.

4.2 Design Approach for Air-Core Synchronous Machines

Until now, the air-core machines were treated from a general point of view, their benefits, and their critical issues. The aim here is to prove that with the appropriate hypothesis, it is possible to obtain analytical expressions that predict the behavior of the magnetic field produced by windings in air, even in "complicated" structures like electrical machines. Moreover, later in this chapter, it will be explained how these

analytical expressions can be used to design an air-core synchronous machine from an electromagnetic point of view. It is important to mention the following, all that is about to be presented is part of the theory explained in [38] and [39]. Generally speaking, the well-known theory of the conventional iron core machine is based on separate consideration of:

- Field in the air-gap (which define the Electro-Mechanical conversion and the steady state performance of the machine) [38];
- Leakage fields (which are relevant under fault operations) [38];

This approach is justified by the large amount of iron in the conventional machines and their small airgap, indeed, thanks to these two features it is reasonable to assume that the flux lines radially cross the Air-gap surface and links with the stator windings through the iron teeth [38]. On the other hand, the flux lines that cross the slots are called *leakage flux*. These simplified magnetic patterns allow an accurate estimation of the parameters and consequently, a good design of the performance of the machine, like everybody is used in the field of electrical machines. In figure 4.4a, an illustration of this concept is presented.

Unfortunately, this clear division between loss components and "power" factors cannot be exploited in air-core machines because the flux lines are not guided. So, it is necessary to explicit the flux produced by each winding, and how each of them is linked together (so self and mutual inductances between windings). In figure 4.4b, it is possible to see that in air-core machines, with an iron stator yoke that works like an environmental shield, there is not a clear division of the patterns.

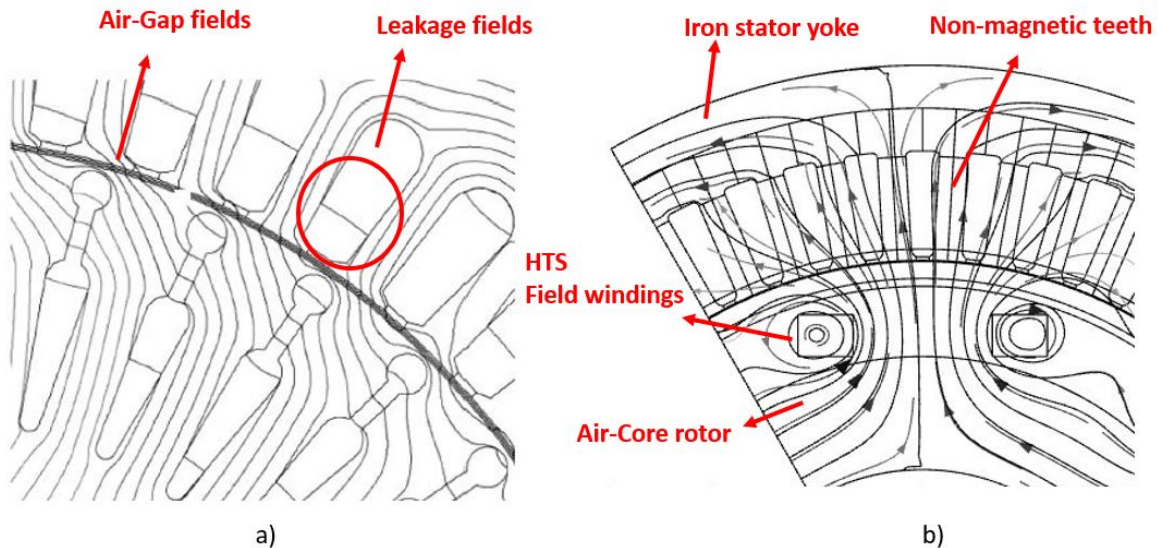


Figure 4.4: Fig.a) Flux lines patterns in a conventional machine with iron-core rotor and magnetic teeth [36]; Fig.b) Distribution of flux lines in an Air-Core machine.

Based on these considerations, when designing an air-core machine **The parameters of capital importance are the radii of the windings and the radii of the iron surfaces** [38], so the position of the stator yoke in this case. This approach

is not very common regarding the design of conventional machines in which the most commonly used dimensions are the air-gap extension and slots size. From this point ahead, all of the parameters that will be exposed will refer to the radii in the middle of the stator and rotor windings [39].

4.2.1 Analysis of field in the Air

To understand the behavior of the magnetic field in air-core machines, the focus is on the mutual between armature windings and rotor, in particular in the magnetic field acting on the stator windings produced by rotor field coils.

It is operated in the following way:

1. A fully air-core machine is considered for evaluating the radial component of magnetic flux density;
2. The effect of the iron stator yoke is simulated later through specific correction factors;

An important thing to underline is that, for the theory to be valid, the thickness of the stator yoke must be significantly less than the diameter of the machine so that its insertion does not modify the air-core nature of the machine[39].

Generalized Machine

With reference to figure 4.5, a winding with a sinusoidal distribution of current with amplitude A (eq. 4.1) is inserted in a generalized machine environment:

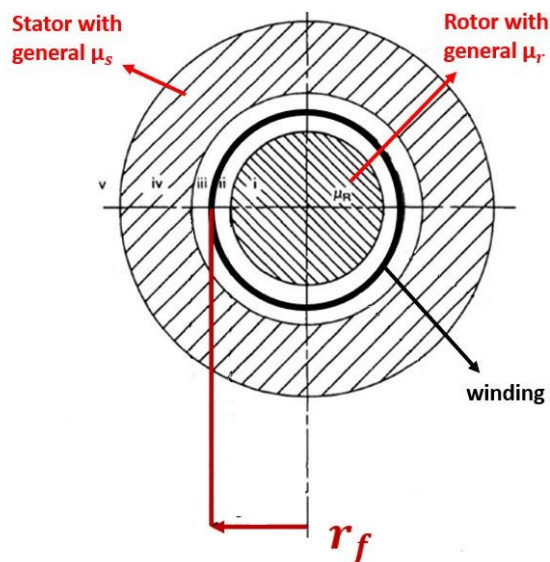


Figure 4.5: Generalized Machine Structure [38].

It is possible to change the nature of this machine by changing the parameters: μ_s & μ_r . According to what has already been said, initially, these values will be assumed

to both equal to 1. So a fully air-core machine configuration is studied. Let's assume that the amplitude of the sinusoidal distribution in the winding is the following:

$$A = \left(\frac{2T_{ph}K_w}{\pi r_f}\right)i \quad (4.1)$$

Solving the Laplace's equations in terms of Vector Potential, the radial component of magnetic flux density is obtained inside and outside the winding [38]:

- Inner region $r < r_f$

$$B_r = \frac{\mu_0 A}{2} \left(\frac{r}{r_f}\right)^{p-1} \cos p\theta \quad (4.2)$$

- Outer region $r > r_f$

$$B_r = \frac{\mu_0 A}{2} \left(\frac{r_f}{r}\right)^{p+1} \cos p\theta \quad (4.3)$$

From a careful analysis of the expressions, an important result can already be noted: The falling of the magnetic flux density is more pronounced when there are more pole pairs [38]. With reference to figure 4.6 the number of pole pairs works as a "constraint" for the flux lines to fall more rapidly:

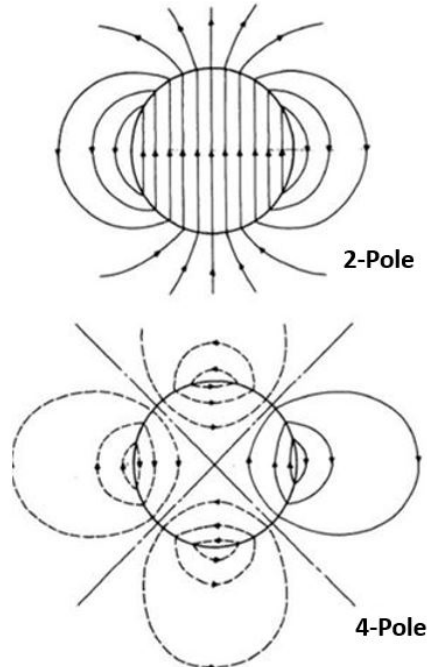


Figure 4.6: Flux lines distribution in air with different pole pairs [38].

The results of the analysis of the distribution of the magnetic field in air is summarized in the following table (easily obtained by substituting the values in expressions 4.3):

Radial position	2 Pole winding	4 Pole winding	6 Pole winding
$r < r_f$	uniform	$\frac{1}{r}$	$\frac{1}{r^2}$
$r > r_f$	$\frac{1}{r^2}$	$\frac{1}{r^3}$	$\frac{1}{r^4}$

Table 4.1: Radial distribution of magnetic flux density with different pole pairs.

At this point, the effect of an iron stator yoke can be simulated imposing the permeability of the stator to be $\mu_s = 1000$.

Its purpose is to contain the flow lines within a closed perimeter, so it acts as an environmental shield. Again with reference to [38], under the hypothesis that the stator yoke is "thin" with respect to the whole radial extension of the machine, the magnetic flux density distribution can be obtained correcting the previous expressions of the radial component of magnetic flux density with two **Iron factors**: η and Λ_s . In this way, it is possible to include the influence of an iron part in an air-core structure.

- Inner region $r < r_f$

$$B_r = \frac{\mu_0 A}{2} \left(\frac{r}{r_f}\right)^{p-1} [1 + \eta \Lambda_s \left(\frac{r_f}{r_{s1}}\right)^{2p}] \cos p\theta \quad (4.4)$$

- Outer region $r > r_f$

$$B_r = \frac{\mu_0 A}{2} \left(\frac{r_f}{r}\right)^{p+1} [1 + \eta \Lambda_s \left(\frac{r}{r_{s1}}\right)^{2p}] \cos p\theta \quad (4.5)$$

Where the iron factors are:

$$\eta = \frac{[1 - \left(\frac{r_{s2}}{r_{s1}}\right)^{2p}]}{[1 - \Lambda_s^2 \left(\frac{r_{s2}}{r_{s1}}\right)^{2p}]} \quad (4.6)$$

$$\Lambda_s = \frac{\mu_s - 1}{\mu_s + 1} \quad (4.7)$$

2 Pole Fully Air-Core Machine

A brief example that explain how this results must be read is presented, in order to help the reader to familiarize with air-core machines.

Let's consider the following 2-pole parameterized machine:

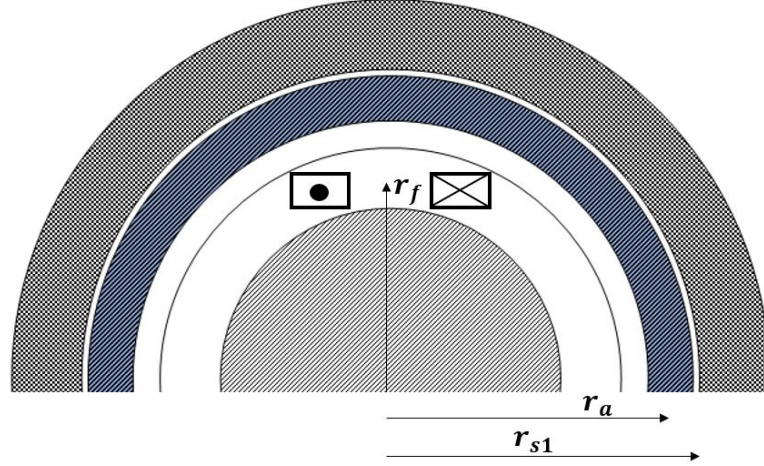


Figure 4.7: Generalization of the 2-pole machine.

Where: r_f is the average radius of the field windings in the rotor, r_a is the average radius of the Armature windings ($D = 2r_a$), r_{s1} is the radius at which the stator yoke start.

The power provided by such machine is governed by the well Known sizing equation applied to the stator windings, so at the radius r_a :

Sizing Equation

$$T_G = \frac{\pi}{2\sqrt{2}} K_w B_{s0} A_s D^2 L \quad (4.8)$$

Where B_{s0} is the peak value of the magnetic flux density at armature winding radius [37], A is the electrical Loading, k_w is the winding factor, D is diameter of the machine at half of the armature windings ($D = 2ra$) and L is the active length of the machine. According to [39] the stator flux density B_{s0} expressed as a function of D , N_f and I_f is the following:

$$B_{s0} = \frac{\mu_0 N_f I_f r_f}{D^2} \quad (4.9)$$

The correct way to read this expression is the following: B_{s0} is The radial component of the magnetic Flux density in the stator windings (at their half) produced by the field windings positioned at radius r_f .

Iron Stator Yoke

Now that the basic concepts of 2 Pole fully air-core machine have been presented, it is possible to take into account the iron stator yoke. Starting from eq.4.5, and considering:

$$\mu_s \approx 1000 \quad (4.10)$$

The iron factors become:

$$\Lambda_s = \frac{\mu_s - 1}{\mu_s + 1} \approx 1 \quad (4.11)$$

$$\eta = \frac{[1 - (\frac{r_{s2}}{r_{s1}})^{2p}]}{[1 - \Lambda_s^2 (\frac{r_{s2}}{r_{s1}})^{2p}]} \approx 1 \quad (4.12)$$

resulting in a final expression of this type:

$$B_{s0} = \frac{\mu_0 N_f I_f r_f}{D^2} [1 + (\frac{r_a}{r_{s1}})^2] \quad (4.13)$$

Which expresses the peak value of magnetic flux density at armature windings produced by rotor field windings, in presence of iron stator yoke [39]. These expressions thus presented in a simple example, allow to have a rough estimation of how much more magnetomotive force is needed in order to achieve a given B_{s0} with respect to an analogous conventional machine.

4.2.2 Design Formulas

Now that all of the theoretical aspects regarding the magnetic field produced by windings in the air has been presented, in this section, the aim is to provide a set of equations that can be used in the first stage of the design for an air-core machine with p pole pairs windings.

HTS Field windings

Let's consider a parametrized machine like the one of figure 4.8

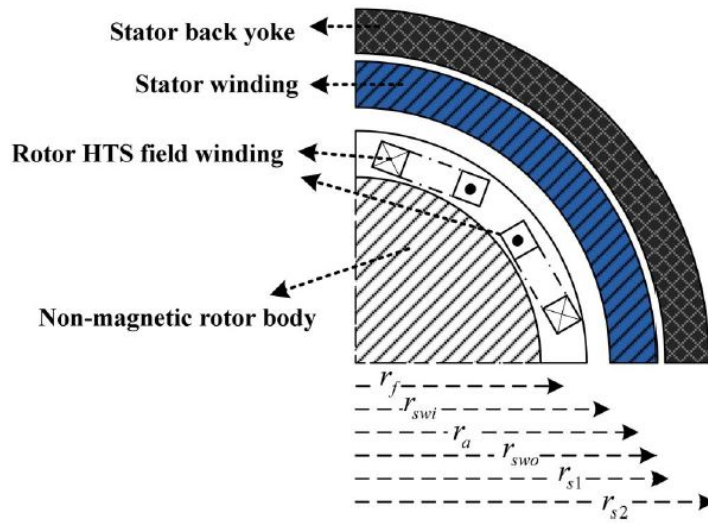


Figure 4.8: Parametrization of a p pole machine.

According to [37], the total magnetomotive force needed for achieving a desired stator magnetic flux density, considering a general value of pole pairs p can be deduced from equation 4.14 derived by [37]:

$$N_f I_f = \frac{\pi r_f B_{s0}}{\mu_0 \left(\frac{r_f}{r_a}\right)^{p+1} \left[1 + \left(\frac{r_a}{r_{s1}}\right)^{2p}\right]} \quad (4.14)$$

Where B_{s0} is the peak value of the fundamental harmonic of the flux density. At this point, the cross section of the HTS coil can be calculated as follow:

$$S_{rs} = \frac{(N_f I_f)_p}{J_f} \quad (4.15)$$

where J_f is the current density of the HTS windings and $(N_f I_f)_p$ is the magnetomotive force for each pole pair. It is obtained dividing the whole Fmm for the number of pole pairs of the machine:

$$(N_f I_f)_p = \frac{(N_f I_f)}{p} \quad (4.16)$$

As explained in section "Analysis of field in air" (4.2.1), according to [38], equation 4.14 was obtained under the hypothesis of windings with sinusoidal distribution of current. Nevertheless, in real superconducting electrical machine applications, HTS field windings are employed under the shape of pancakes. In particular, in figure 4.9a) it is possible to understand how the HTS windings are arranged, one pancakes is made of several turn of HTS tapes, it is possible to use even more than one pancakes simply by placing each of them on top of the other. In figure 4.9b), it is shown the 2D view of the HTS field windings in the Machine.

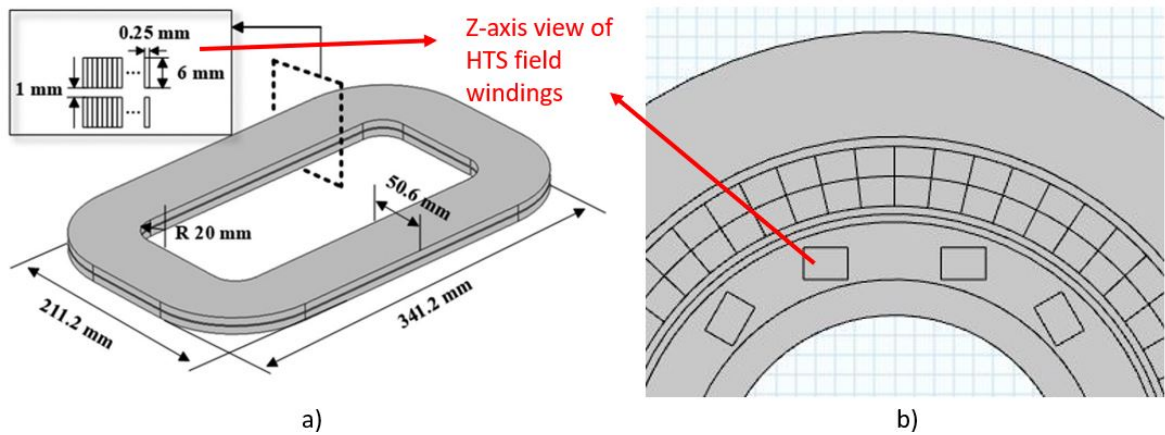


Figure 4.9: Fig.a) General structure of a "pancake" used in HTS field windings [40]; fig.b) 2D view of the HTS field windings modeled as homogenized bulk in the machine.

From this illustration, it is possible to understand that the real distribution of current in the rotor windings is not sinusoidal, but more similar to a trapezoid form. Making the approximation to a square wave distribution of current, since the peak value of the fundamental of a square wave is $\frac{4}{\pi}$, a correction factor to the magnetomotive force needed for the desired value of B_{s0} was implemented. For clarity, in figure 4.10 it is shown the peak value of the square wave to implement, such that its fundamental coincide with the one provided by equation 4.14, which is evaluated under the hypothesis of sinusoidal distribution of current.

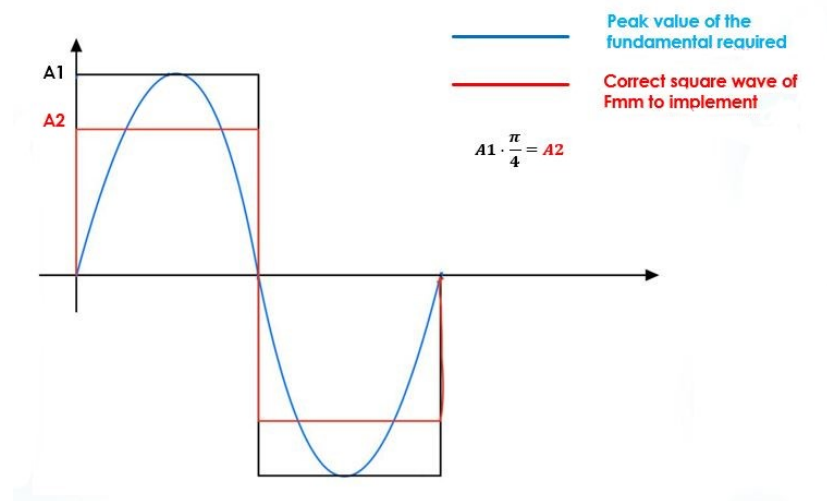


Figure 4.10: Correction Factor for Fmm evaluation.

So, the magnetomotive force density that has been implemented in the software is the following:

$$N_f I_f' = N_f I_f \times \frac{\pi}{4} \quad (4.17)$$

In this way, even the magnetomotive force for each pole pair is reduced by a $\frac{\pi}{4}$ factor like expressed in equation 4.18:

$$(N_f I_f)'_p = \frac{(N_f I_f)'}{p} \quad (4.18)$$

To note that this correction factor it was never mentioned in [37], indeed, this correction factor was introduced to improve accuracy of equation 4.14. In the preliminary design section (4.3.1), a comparison between the results obtained with and without the correction factor will be presented. However, there is another possibility to improve the accuracy of equation 4.14, as expressed in [37], it is possible to change the distance between the HTS field windings in order to reduce the harmonic content of the radial component of the magnetic flux density calculated at the mean armature windings radius. With reference to figure 4.11, h_{HTS} is the height of the HTS coil, while w_{HTS} is the width of the HTS coil. The distance between coils: d_c is a parameter that can be object of future optimization for the machine.

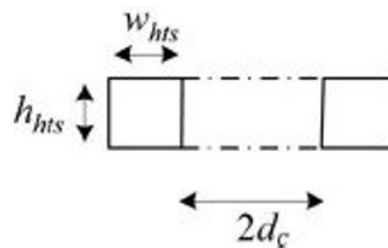


Figure 4.11: Distance between HTS coils.

Stator windings

Let's consider the sizing equation for an air-core synchronous machine applied to the armature windings:

$$T_G = \frac{\pi}{2\sqrt{2}} K_w B_{s0} A_s D^2 L \quad (4.19)$$

According to equation 4.19, once the winding factor k_w is known, the utilization factors B_{s0} , which is the peak value of the fundamental of magnetic flux density calculated at the mean armature windings radius, and the electrical loading, it is possible to obtain the overall volume of the electrical machine ($D^2 L$). It is reasonable to expect that this volume will be significantly lower with respect to a conventional machine of the same rated power and speed thanks to the possibility to significantly increase the magnetic flux density B_{s0} and the electrical loading A_s .

According to [41] the number of conductors per each slot can be calculated as follow:

$$n_c = \frac{\sqrt{2} E_0}{2\pi n_s k_w D B_{s0} L q p / a} \quad (4.20)$$

where E_0 is the RMS value of the no-load phase voltage, n_s is the rotational speed in round per seconds, p is the pole pair of the machine and a are the external stator parallels.

Regarding the dimension of the slot, it must be remembered that employing a slotless configuration of the stator, more space is available for the armature conductors, and this is the reason why it is possible to increase A_s in such machines. However, due to the very large force involved during the operation of the machine, accurate studies of the support structure are needed. Since no mechanical studies have been done in the thesis, it wasn't possible to provide an indication about the dimension of the "virtual slot" in the stator. For this reason, the rated armature current, needed for the performance of the machine was implemented in an equivalent virtual slot. A large margin of safety was taken in the cross-section of the virtual slot in order to avoid inconsistencies. However, on the basis of what has been said so far, it is reasonable to expect that even considering mechanical and thermal constraints, the total utilization of the stator can increase thanks to the more available space with respect to a conventional machine [35].

Stator yoke

The design of the stator yoke is crucial for the achievement of the desired performance of the machine. Since this is the only iron part in the machine, the thickness of the stator yoke must be designed in such a way that the saturation limit is never reached. At the same time, for the theory of fields in the air to be valid, the thickness of the yoke must remain small compared to the radial extension of the entire machine. FeCo iron will be used thanks to its high value of magnetic saturation flux density. According to [42] the thickness of the iron stator yoke can be obtained as follow:

$$t_{yoke} = \frac{B_{s0}}{p B_{sat}} \left(\frac{r_a}{r_{s1}} \right)^{p+1} \frac{2r_a}{\left[1 + \left(\frac{r_a}{r_{s1}} \right)^{2p} \right]} \quad (4.21)$$

where B_{sat} is the maximum acceptable value of magnetic flux density, r_a is the mean armature windings radius, p is the pole pair of the machine and r_{s1} is the inner stator yoke radius shown in figure 4.8.

4.3 Preliminary Design of the machine

At this point, the necessary theoretical basis for understanding how to proceed, in the first stage of an electromagnetic design of an air-core synchronous machine, is assumed to be acquired. To remember, the ultimate goal of this thesis is to make a preliminary design of an air-core partially synchronous machine for aircraft applications, with an iron stator yoke acting as an environmental shield. From an electromagnetic point of view, the general structure of this type of machine is "simple", indeed, the complex structures of the actual conventional machines are due to two fundamental needs: Having sinusoidal distribution of B on the air-gap and avoiding saturation of the iron teeth.

In air-core machines there is no iron teeth and the sinusoidal distribution of B can be easily obtained optimizing the distance between the superconducting coils [37]. Non-ferromagnetic parts can be made by **Fiber-Glass** [35]. The consequence of this, is a simplified, but realistic, electromagnetic model like the one in the following picture [32]:

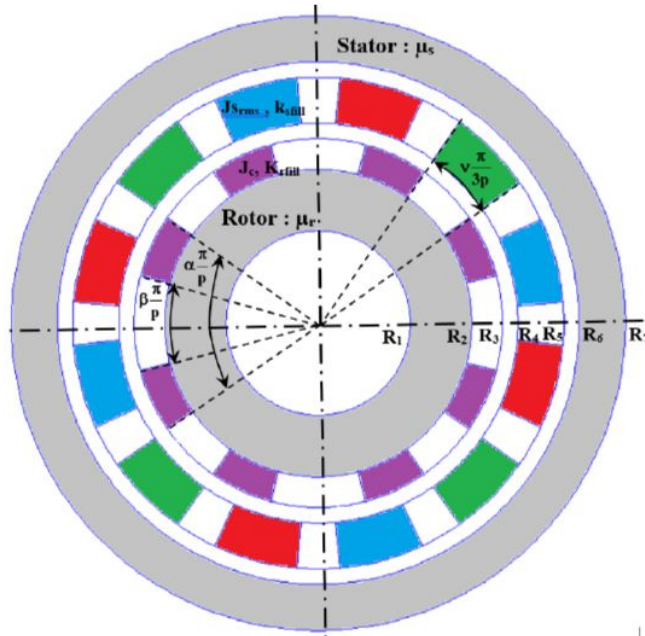


Figure 4.12: Air-core Machine schematization from [32].

The first step in the design, is to attribute the parameter of interest of the machine:

- Field windings mean radius R_3 ;

- Equivalent Air-Gap ($R_4 - R_3$);
- Thickness of the stator yoke ($R_7 - R_6$);

The equivalent air-gap and the distance between the rotor and armature windings, are very important factors which must be decided **as a function of the cooling method**, indeed, this can widely change in case the entire electrical machine is immersed in the cooling bath, or only the rotor. In case only the rotor is immersed, the air-gap must be chosen bigger in order to allow the insertion of the cryostat. However, in the context of this thesis, a safe margin on the dimension of the equivalent air-gap was taken, since optimization is out of the scope of the thesis.

4.3.1 HTS Synchronous Motor Design

According to what has been said so far, the focus is on the design of a partially superconducting machine, which could be used for medium size aircraft [6]. In particular, the machine will be the Synchronous motor indicated by Nasa of the Single-Aisle STARC-ABL [18], partially turbo-electric propulsion with a maximum capacity of 150 PAX. According to [6], the main specifications of the Motor are:

Parameter	Value
Output Power P_M [MW]	2.61
Peak value Line Voltage [kV]	2
Rated shaft speed [rpm]	2500
Supply Frequency [Hz]	125

Table 4.2: Basic Design Parameters of the Synchronous HTS Motor.

Since this machine is in an early stage yet, in [6] only the output power and rated speed are indicated. The other parameters have been decided on the basis of an analysis of the literature. For example, in [1] the problem of the rated line voltage emerged, there is not a commonly accepted value for the voltage, anyway, a value of 2 kV was a starting point for further design and optimization. The pole number, instead, has been decided to be 6, inside the range suggested in [3] for partially superconducting machines. Let's consider a model of the machine, in which all of the geometrical parameters of interest are expressed in a general way:

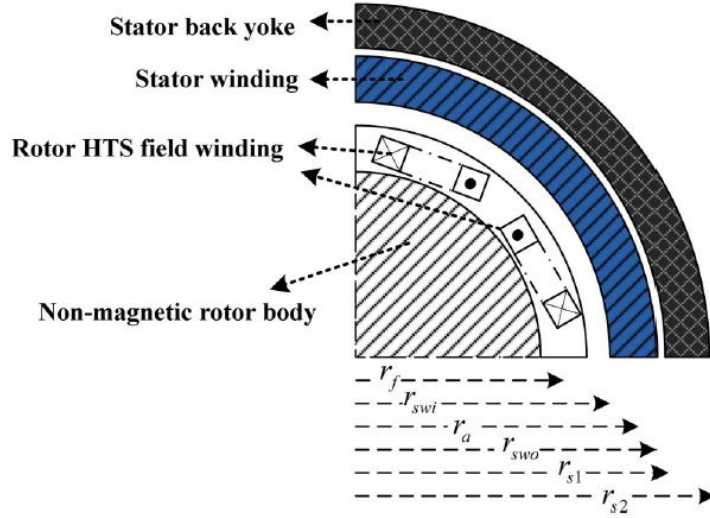


Figure 4.13: Schematic of the Synchronous Motor with HTS field windings [37].

The output power of a superconducting machine of this type is given by [37]:

$$P_G = \frac{\pi^2}{\sqrt{2}} K_w B_{s0} A_s D^2 L n_s \quad (4.22)$$

Where B_{s0} is the fundamental value of the magnetic flux density in the armature windings, for this application, after several attempts to understand the best value of B , a value of 2.3 T has been chosen. This decision was taken after a trade-off between the necessity of increasing the magnetic flux density to increase the performance of the machine and to keep the thickness of the stator yoke "thin", with respect to the diameter at the armature windings. In particular, the FeCo iron is made to work at about 2T, near the knee of its magnetic characteristic as shown in figure 4.18. $B_{s0} = 2.3$ T proved to be the best compromise in these terms; k_w is the fundamental winding factor, given the windings arrangement, was computed to be 0.96. The electrical loading A_s was chosen according to [36], where a value of 250 kA/m is indicated as possible. Depending on the cooling method, with a slotless configuration of the stator, it is possible to increase the electrical loading up to 350 kA/m as proposed in [37]. However, since the focus of this thesis is not to design an optimized machine, it has been decided to remain conservative for the choice of the main parameters.

Finally, n_s is the mechanical speed in round per second $n_s = \frac{2500}{60} = 41.67 rps$.

According to [36], with 3 pole pairs, a ratio between active length of the machine and its diameter (calculated at mean armature windings radius) of 0.5 was chosen:

$$\frac{L}{D} = 0.5 = \chi \quad (4.23)$$

Substituting all of the mentioned values, the value of the Diameter of the machine, intended as $D = 2r_a$, so the diameter of the machine at the armature windings was calculated:

$$D = \sqrt[3]{\frac{\sqrt{2}P_M}{\pi^2 k_w B_{s0} A_s \chi n_s}} = 0.32m \quad (4.24)$$

so an active length of the machine $L = 0.16m$ was deduced.

At this Point, in table 4.3 a summary of the main operation dimensions and characteristics is summarized.

Parameter	Value
Stator Windings Magnetic Flux Density B_{s0} [T]	2.3
Electrical Loading A_s [kA/m]	250
Length of the Motor L [mm]	160
Stator winding Diameter of the Machine D [mm]	320
Number of phases m	3
Pole pair p	3
N of slot per pole per phase q	3

Table 4.3: Operation parameters and dimension chosen for the motor.

According to table 4.3 a number of total "equivalent slot" of 54 was chosen.

With reference to [41], the number of conductors in each slot can be calculated as expressed below:

$$n_c = \frac{\hat{E}_0}{2\pi n_s k_w D B_{s0} L q p / a} = 13 \quad (4.25)$$

where \hat{E}_0 is the peak value of the no-load phase voltage equal to 1155 V, according to table 4.2. While the peak value of the phase current can be evaluated with equation 4.26:

$$\hat{I}_A = \frac{2P_M}{3\hat{E}_0} = 1506.5A \quad (4.26)$$

Where P_M is the rated output power of the motor.

Now it is possible to evaluate the number of turn in series per phase N_1 , exploiting the RMS value of the phase current $\tilde{I}_A = \frac{\hat{I}_A}{\sqrt{2}} = 1065A$:

$$N_1 = \frac{\pi D A}{2m \tilde{I}_A} \approx 40 \quad (4.27)$$

At this point, the main parameters of interest for the stator design were calculated. As it has already been said, since mechanical and thermal studies are not treated, it was decided to implement the armature current in an equivalent cross-section of the virtual slot with a great safe margin. In this way, it is possible to leave room for future insights and to focus on the electromagnetic response of the machine.

4.3.2 HTS Field Winding Design

SuperOx YBCO Tape

For the modeling of the designed electrical machine, new manufactured YBCO tapes from SuperOx were used [26]. According to the manufacturer, a $I_c = 1000A$ was used for each 4 mm wide tape. the thickness of each tape is 0.1 mm according to [26], a thickness of 0.05 mm (h_{insul}) for the insulation between tapes was used, in order to evaluate the total surface of the HTS filed winding (see fig.4.15). The structure of the 2G coated conductors YBCO tape manufactured by SuperOx is shown in figure 4.14:

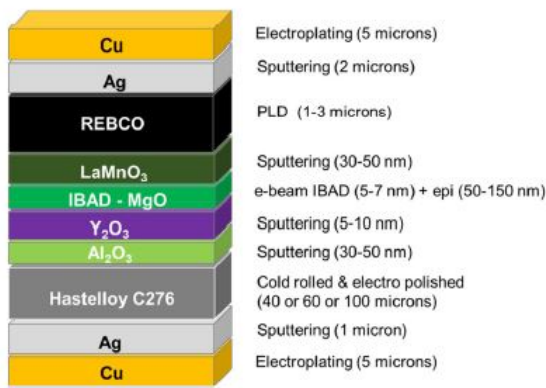


Figure 4.14: YBCO tape composition [26].

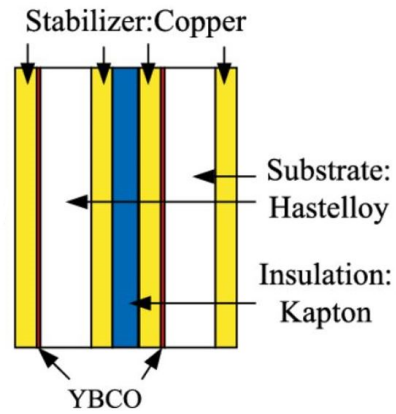


Figure 4.15: Insulation YBCO tape.

It has been decided to exploit this YBCO tape at $I=500 A$ for each 4 mm wide tape, operating at a temperature of 20 K (LH_2). As it is possible to see in figure 4.16 SuperOx YBCO tape present optimal performances even when operating at high magnetic field. In particular, $I = 500A$ was sufficiently below the critical current for all of the operating conditions in the electrical machine.

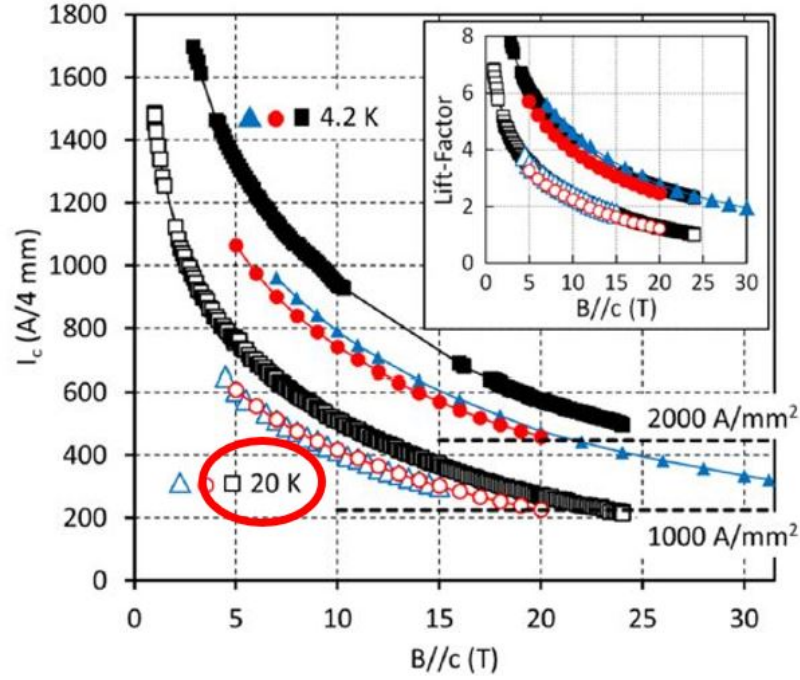


Figure 4.16: Critical Current for a 4 mm wide YBCO Tape as a function of the perpendicular component of the external magnetic flux density [26]. The YBCO tape of interest is the one indicated with a white square.

The total magnetomotive force for producing the desired value of 2.3 T at the stator windings is expressed by equation 4.28, as a function of r_f , r_a , and r_{s1} . $r_a = 160mm$ was calculated from the sizing equation and it is the starting parameter, r_f is the rotor winding mean radius, this value, was chosen to be $130mm$ in order to take a safe margin for the cryostat for the equivalent air gap from the rotor to stator windings, while the stator inner yoke was chosen to be $r_{s1} = 180mm$, considering the dimension of the equivalent virtual slots.

$$N_f I_f = \frac{\pi r_f B_{s0}}{\mu_0 \left(\frac{r_f}{r_a}\right)^{p+1} \left[1 + \left(\frac{r_a}{r_{s1}}\right)^{2p}\right]} \approx 1.14610^6 Am \quad (4.28)$$

The total magnetomotive force $N_f I_f$ is then multiplied for the "correction factor" $\frac{\pi}{4}$. Subsequently, it is divided for the number of pole pair. The correct value of magnetomotive force to implement for each pole is presented in equation 4.29:

$$(N_f I_f)_p = 3 \approx 10^5 Am \quad (4.29)$$

Considering that each tape carries 500 A, the number of total turns is:

$$N_{tot} = \frac{(N_f I_f)_p}{500} = 600 \quad (4.30)$$

It has been decided to use 4 pancake (stacks) with 150 turns each and all connected in series, see figure 4.17:

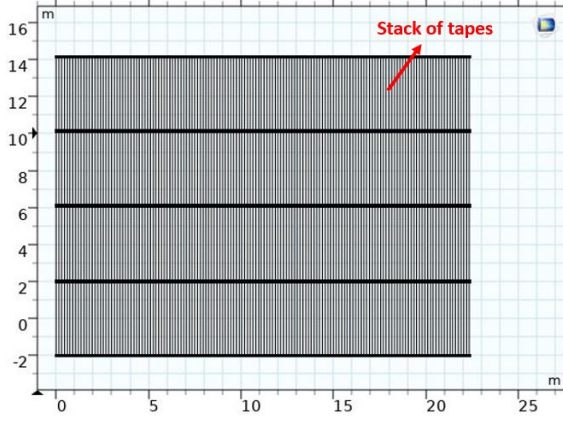


Figure 4.17: Schematization of the HTS tapes in the rotor of the machine.

As already explained, this is not the way that the tapes have been modeled and implemented in Comsol, indeed as stated in chapter 3, an homogenization technique with equivalent bulk was used so, at this point, it is necessary to calculate the total engumbrance of the equivalent bulk that will be implemented. With reference to figure 4.15, each tape has a thickness of 0.1 mm and a width of 4 mm [26]. For evaluating the total engumbrance it is necessary to decide the distance between the tapes, which is given by the insulation:

Parameter	Value	definition
$h_{insul-stack}$	0.05 mm	Vertical distance between stack of tapes
$h_{insul-turns}$	0.05 mm	Horizontal distance between turns of tapes
N_{stack}	4	Number of vertical stacks
N_{turns}	150	Number of turns
h_{tape}	0.1mm	thickness of the tape
w_{tape}	4mm	width of the tape

Table 4.4: YBCO Tapes parameters.

According to the distance between tape, it is now possible to calculate the width and the height of the **equivalent bulk** in which a constant equivalent current density is supplied:

$$w_{bulk} = (h_{tape} \times N_{turns}) + (h_{insul-turn} \times (N_{turns} - 1)) \quad (4.31)$$

$$h_{bulk} = (w_{tape} \times N_{stack}) + (h_{insul-stack} \times (N_{stack} - 1)) \quad (4.32)$$

While the equivalent current density to apply to the bulk is evaluated by:

$$J_{eq} = \frac{(N_f I_f)_p}{(w_{bulk} \times h_{bulk})} \quad (4.33)$$

4.3.3 Stator yoke design

According to equation 4.34 the thickness of the stator yoke is evaluated imposing a maximum value of the magnetic flux density possible. In this case, FeCo iron was chosen. It has been decided to make the most from the iron by making it work around the knee of its characteristic, like shown in figure 4.18.

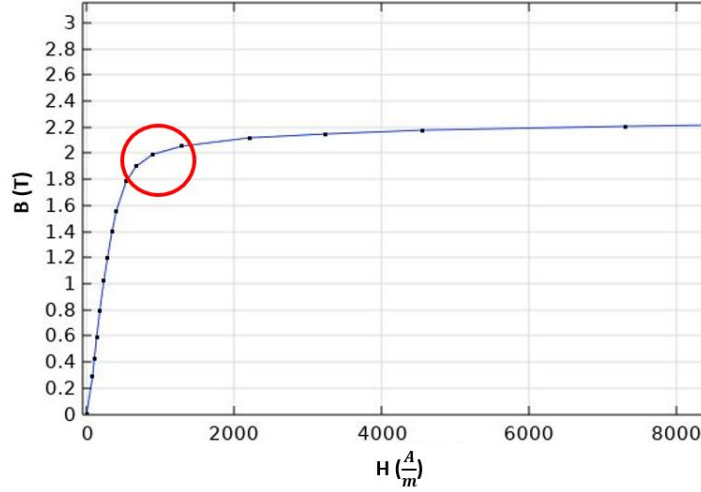


Figure 4.18: Magnetic characteristics of FeCo, in red the operation point.

with reference to equation 4.34, it has been imposed a maximum value of magnetic flux density $B_{sat} = 2T$.

$$t_{yoke} = \frac{B_{s0}}{pB_{sat}} \left(\frac{r_a}{r_{s1}}\right)^{p+1} \frac{2r_a}{\left[1 + \left(\frac{r_a}{r_{s1}}\right)^{2p}\right]} \approx 52mm \quad (4.34)$$

Thus, the finalized geometry of the machine is the one presented in the following picture 4.19:

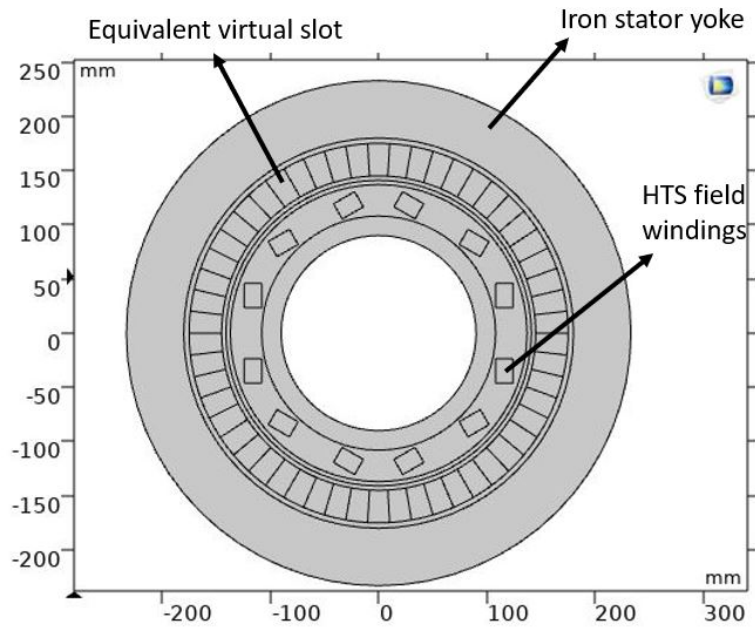


Figure 4.19: 2.61 MW HTS Synchronous motor for Aircraft Application.

Lastly, it must be remembered that the iron is used only in the stator yoke. For the armature winding it has been used Copper, while for the rotor part Fiber Glass has been used.

4.3.4 Validation of the Analytical Design by FEM

Magnetostatics

To start, let's see if the estimated magnetomotive force at the rotor field windings produce the desired value of fundamental of magnetic flux density:

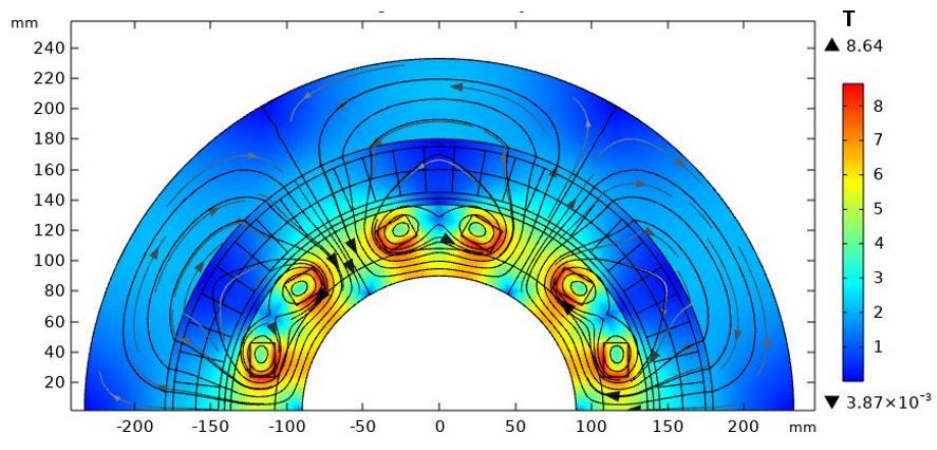


Figure 4.20: Magnetic Flux density map of the 2.61 MW Synchronous motor.

The maximum value of the magnetic flux density in the iron stator yoke is $B = 2.14T$ which can be considered a good result for the equation 4.21.

The magnetic flux density distribution at the armature windings mean radius is shown in figure 4.21. One important thing here, in order to obtain a reduced harmonic content of the magnetic flux density, it is necessary to do an optimization of the distance of the two HTS coil like the one proposed in [37]: With reference to figure 4.11, it has been decided a distance of the coils of $d_c = 92mm$.

Like it is possible to see in figure 4.21, with the analytical approach presented in this thesis, combined with an optimization of the distance of the coil, it is possible to obtain a radial distribution of B in the stator windings which is similar to a sin-wave. A fundamental value $B_{s0} = 2.31T$ was obtained in line with theoretical expectations.

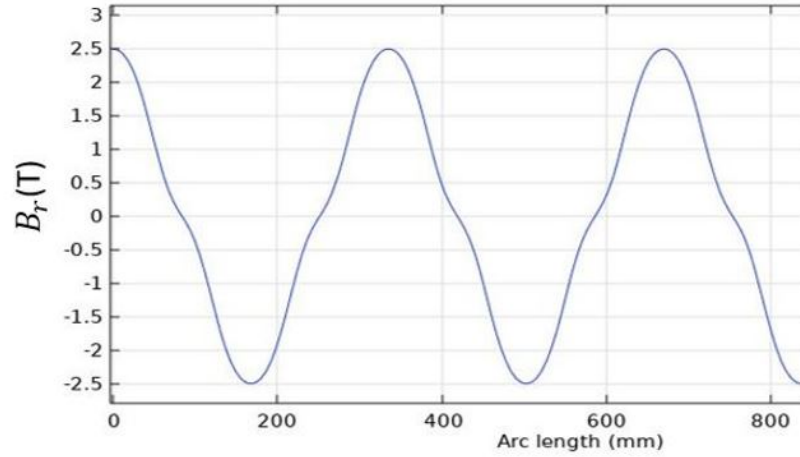


Figure 4.21: Magnetic Flux distribution at mean armature stator windings radius.

The harmonic content of the magnetic flux density at the mean armature stator windings is summarized in table 4.5. As it is shown, the only relevant contribution over the fundamental is given by the third and the fifth harmonic.

fundamental [T]	3rd harmonic [T]	5th harmonic [T]
2.31	0.28	0.9

Table 4.5: Fast Fourier Transform of the stator magnetic flux density

The fast Fourier transform is very important in the design of air-core synchronous machines, indeed, it is necessary to verify the optimization process through the variation of the distance d_c between the coils.

At this point, it is interesting to compare the results of the magnetic flux density at the armature mean windings radius obtained through this process and without the correction factor $\frac{\pi}{4}$. Starting from equation 4.29, without the correction factor, $(N_f I_f)_p$ would have been:

$$(N_f I_f)'_p = 3 \times 10^5 \frac{4}{\pi} \approx 3.82 \times 10^5 Am \quad (4.35)$$

repeating the same procedure for the evaluation of the number of tapes and their size, and implementing this magnetomotive force at the HTS field windings for each pole pair, it is possible to obtain the magnetic flux density distribution shown in figure 4.22

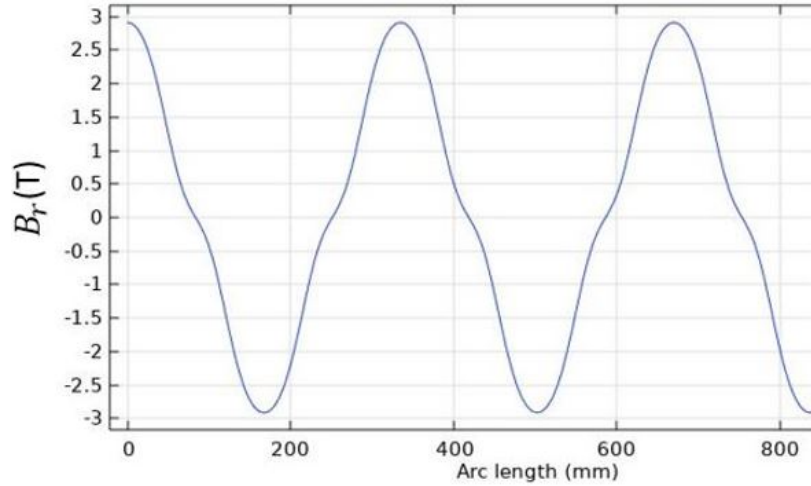


Figure 4.22: Magnetic Flux distribution at mean armature stator windings radius without correction factor.

The harmonic content is summarized of the stator magnetic flux density in this case is summarized in table 4.6

fundamental [T]	3rd harmonic [T]	5th harmonic [T]
2.67	0.335	0.1

Table 4.6: Fast Fourier Transform of the stator magnetic flux density

According to the expectations, the value of B_{s0} is greater because without the correction factor, the magnetomotive force implemented is the one calculated under the hypothesis of sinusoidal distribution of current, which does not correspond to reality.

No-Load Simulation

At this point, implementing the rotational speed of the rotor, it is possible to run a no-load simulation. This simulation was necessary to verify the value of the induced EMF given by equation 4.25 and the effective voltage in the machine:

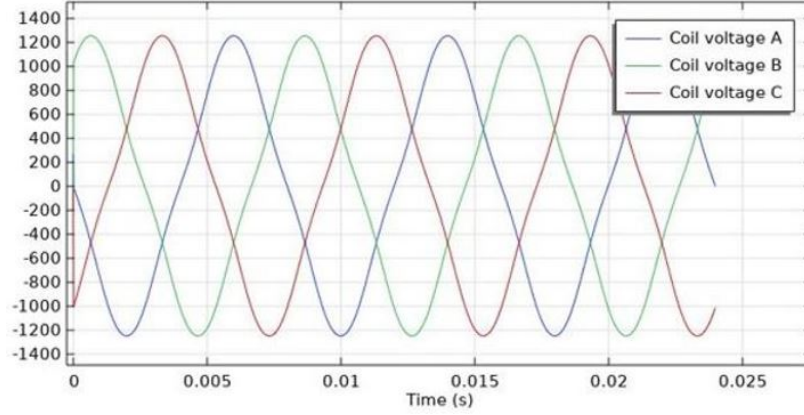


Figure 4.23: No-Load Phase voltage of the HTS Synchronous motor.

A value of $E_0 = 1162$ V for the first harmonic was calculated while a value of 1155 V was expected, so an excellent match.

Load Simulation

Lastly, a simulation at load is proposed, in figure 4.24 it is possible to appreciate the magnetic flux density map of the 2.61 MW motor HTS synchronous motor.

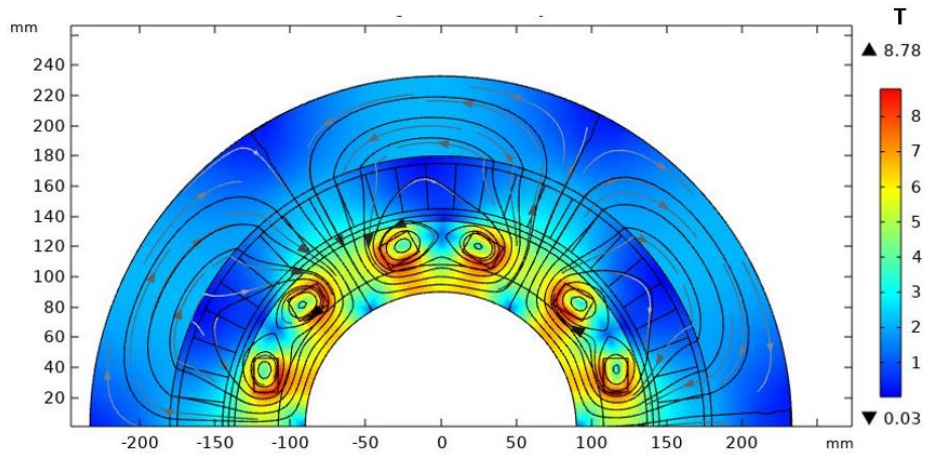


Figure 4.24: Magnetic flux density map at load.

One last check for the preliminary design is necessary: The Electromagnetic Torque. The theoretical torque that is expected is calculated through the sizing equation 4.36. on the other hand, the torque is evaluated from Comsol selecting the rotor and the HTS field windings as shown in appendix in figure B.5.

$$T_M = \frac{\pi}{2\sqrt{2}} K_w B_{s0} A_s D^2 L = 10.045 kNm \quad (4.36)$$

While the torque calculated by Comsol is the following:

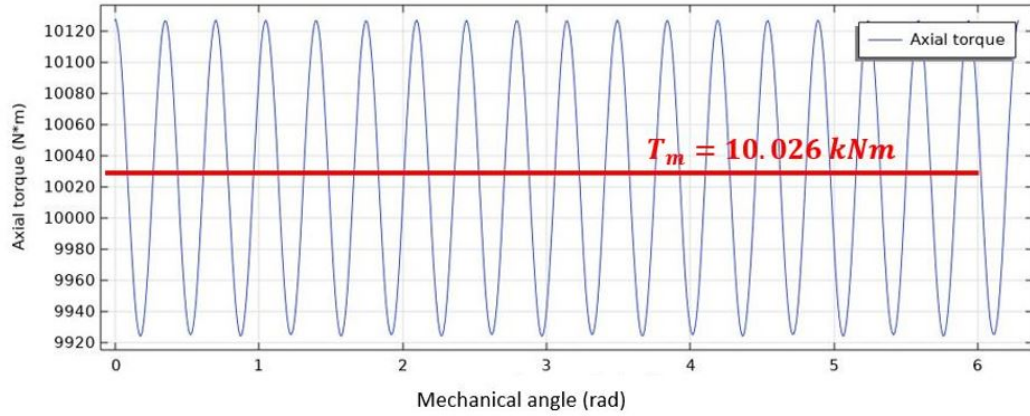


Figure 4.25: Electromagnetic Torque as a function of the mechanical angle.

The mean torque obtained by consol was:

$$T_m = 10.026kNm \quad (4.37)$$

This can be considered a very good match between the analytical formulas and the FEM simulation. Moreover, the ripple of the torque is limited to 2%.

In conclusion, it is possible to state that there is an optimal match between the theoretical calculation and the results obtained through FEM simulation of this partially superconducting synchronous machine for aircraft applications.

After this preliminary design, it is more clear that significant increases of the magnetic flux density B and the electrical loading A_s are feasible with an air-core structure .

All of these characteristics lead to reduced volume and mass of the machine with respect to a conventional one of the same output power. Furthermore, thanks to the slotless configuration, it is possible to reduce the harmonic content of the phase voltage which significantly reduces the torque ripple of the machine.

Chapter 5

Conclusions and Future Works

5.1 Conclusions

There is a real possibility to see in the near future hybrid-electric propulsion system architecture. It is reasonable to think the emergence of these systems will be a slow process, with significant changes in 2035 when it will be possible to see at least the medium size aircraft concept capable of transporting up to 150 passengers. Generally speaking, the future growth of the electric aviation industry depends on the possibility to build very efficient and lightweight electrical machines with values of specific power compatible with the needs of the aeronautical sector.

Although there is still a long way to go, superconductivity is one of the most promising technology for seeing electric aircraft in the future. Despite the complexity linked to the functioning of superconductors, it is possible to simulate their macroscopic electromagnetic behavior in a simple way. An homogenization technique with constant current density was implemented. This is possible because it has been proved that there are no differences, in terms of macroscopic effects, with the more accurate modeling method T-A formulation, which has been used as a benchmark. As regards the preliminary design of an air-core synchronous machine, this thesis has collected all of the information in the literature in order to propose a design approach that proved to be consistent with the FEM simulation results provided by COMSOL. Moreover, the results obtained through the design have confirmed some of the advantages that are on the basis of the drive to develop these types of machine and that it is possible to pursue a preliminary electromagnetic design of an air-core synchronous machine quite simply.

In the case in which a more accurate estimation of the operating conditions of the superconducting tapes is needed, as mentioned in chapter 3 it is possible to use a "multi-scale" approach [30], that allow studying the effective operating conditions of the superconductors without involving the simulation of the electrical machine, this is useful because it allows reducing the overall computational time.

5.2 Future Works

Given the nature of this thesis to be a starting point for the design of an emerging type of electrical machine, the studies to do are many. Whereby, in this section, only general indications and some guidelines will be provided. In particular, the further necessary studies can include:

1. Experimental validation of the superconducting tapes simulated in this thesis;
2. Thermal studies both for rotor and stator part;
3. Mechanical studies for HTS windings and for armature windings;

5.2.1 Experimental validation of Superconducting tapes

Experimental results are needed in order to understand the real consequences of operating YBCO tapes at the conditions indicated in the thesis, 500 A at 20 K. Indeed, the problem could be in maintaining the correct temperature in the tapes. Subsequently, it is necessary to understand how to shield the HTS field windings from the ac fields that are produced in an electrical machine environment in order to avoid uncontrolled growth of losses.

5.2.2 Thermal studies

Thermal studies are needed both for the stator and the rotor. In the stator, it could be very useful to understand how it is possible to achieve a value of the electrical loading up to $350kA/m$ as suggested in [37]. The extra space made available by the slotless configuration can be used in two ways: The first is to implement a more efficient cooling system which allows utilization of the copper armature windings up to $25A/mm^2$ like indicated in [1], the second is simply to keep the same utilization factor of a conventional machine, for instance, $6A/mm^2$, but inserting a greater amount of copper in the stator.

However, when dealing with superconducting machines, one of the most important theme is to decide which cooling method for superconductors is easier to implement and also more effective, or rather, to decide if to cool down only the HTS field windings or the rotor as a whole. Cooling bath, so the complete immersion of the machine in liquid hydrogen, seems to be one of the most commonly used up to now, but also the thermosiphon cooling has good chance to emerge as explained in [15]. This decision could have an effect on the equivalent airgap of the partially superconducting machine, because as already mentioned, in case only the rotor is immersed, this would require more space for the cryostat and increase the distance $(r_a - r_f)$, which is the length of the equivalent air-gap, with a consequent increase of the amount of HTS windings required.

All these aspects need to be investigated in order to build an optimized machine.

5.2.3 Mechanical studies

Due to the high torque that it is possible to achieve with the superconducting machines, and due to the lack of teeth in the stator, the development of light and resistant mechanical support is crucial for the correct functioning and structural integrity of the machine. Moreover, it is very important to check for the mechanical feasibility of the HTS windings.

Lastly, thanks to the growing power of computers, it is now possible to carry out multiphysics simulations that couple electromagnetic, thermal, and mechanical aspects together. This is made possible by software like Comsol. They use Joule losses and iron losses as inputs to study the resulting thermal behavior of the machine. Again, this thermal expansion are used as inputs for the onset of mechanical stresses. The possibility to exploit such simulations will allow the development of very accurate models that can predict the machine performance in almost all operating conditions. Because of their high production cost, this possibility is very desirable in the design of superconducting electrical machines.

Appendix A

Comsol Modeling of an Electrical Machine

In this chapter, the goal is to simulate the wound field synchronous machine explained in [43]. Basically, the goal was to gain experience in electrical machine simulation through the FEM software Comsol Multiphysics. For the validation of the simulation, it has been simulated an electrical machine of which are known both the experimental results and the simulated results with another software: Flux 2D. At the end of the simulation set up, a comparison with the experimental and Flux's results is done.

A.1 Available data of the Machine

Most of the available data can be found in the Ph.D. thesis [44] and Master thesis [43]. It must be remembered that this machine is only an example of which are available experimental results, it is not the machine that has been designed in this thesis work in chapter 4.

As reported in [44] the machine is a three-phase synchronous machine with 3 pole-pairs which specifications are shown in the following table:

Parameter	Value
Maximum Power P_{max}	130 kW
Maximum Torque T_{max}	240 Nm
Maximum Speed w_{max}	12000 rpm

Table A.1: Specifications of the Machine.

While the basic geometry information needed for the simulation set up is the following:

Parameter	Value
Number of pole	6
Number of phases	3
Axial length	123 mm
Stator inner Diameter	165mm
Stator outer diameter	240mm
Shaft diameter	85 mm
Air Gap	0.5 mm

Table A.2: Geometry dimensions of the Machine.

For both stator and rotor has been used an M270-35A iron, whose magnetization curve was experimentally measured in [44].

Final considerations must be made for the windings characteristics of the stator and the rotor, according to [43] the arrangement of the windings are summarized in the following table:

Parameter	Value
Number of Stator Slot	54
Number of turn in series per phase	21
Number of external parallel	3
Stator filling factor	0.5
Number of turns per pole (rotor)	843
rotor filling factor	0.45

Table A.3: Stator and rotor windings characteristics.

A.2 Simulation Set Up

A.2.1 Comsol Interface

Importing the finalized geometry as provided in ([43],[44]) the machine that will be used for the validation is shown in figureA.1.

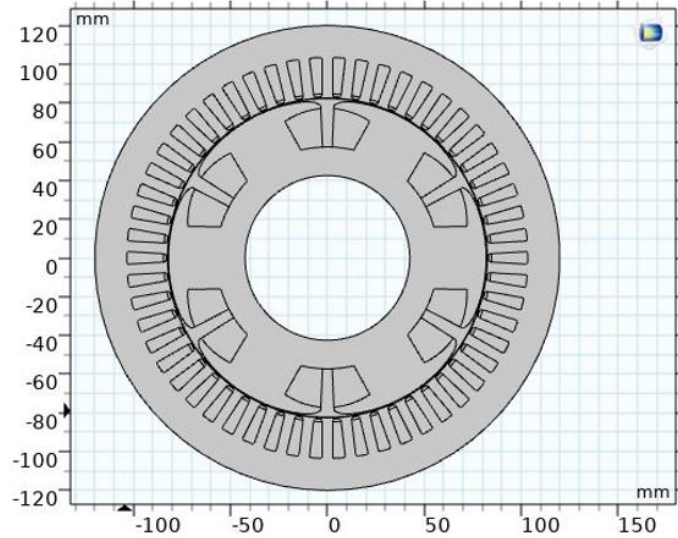


Figure A.1: Finalized geometry of the Machine.

Once imported the geometry, through the physics section it is possible to implement all of the operating conditions of the machine. In particular, for pursuing simulation at load it is necessary to add two different physics environments in comsol. The first one is the rotating machinery, magnetic "rmm", in which it is possible to attribute each phase to the right armature slot, according to the sequence of the phases of the armature windings that have been decided (figure A.2). This armature windings sequence is very important because it is the same used in chapter 4.

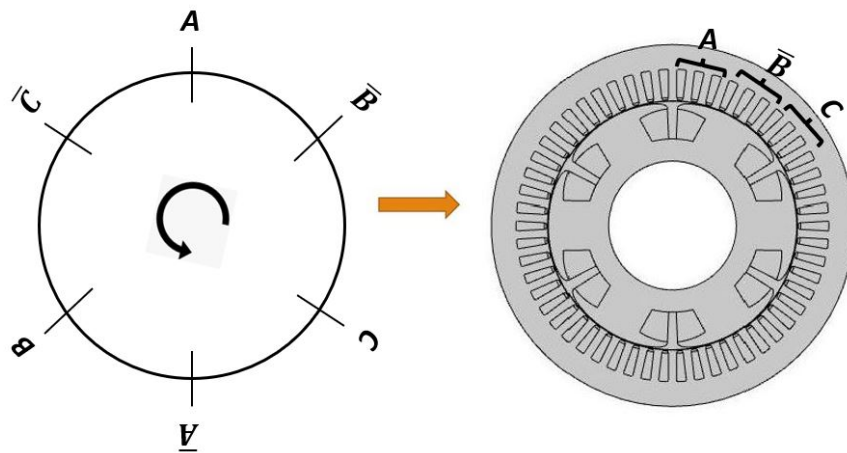


Figure A.2: Winding sequence for a pole pair of machine.

The second physics section is related to the electrical circuit, in which each component is added to build an equivalent electric circuit that represents the arrangements of the windings in the machine. The EC used for the simulation of the synchronous machine is shown in figure A.3. It must be remembered that the machine is a 6 pole with 3 external parallel, so every pole pair of the machine is in parallel and is subjected to the same voltage. Lastly, the current generator of " I_c " is not inserted to avoid numerical problems.

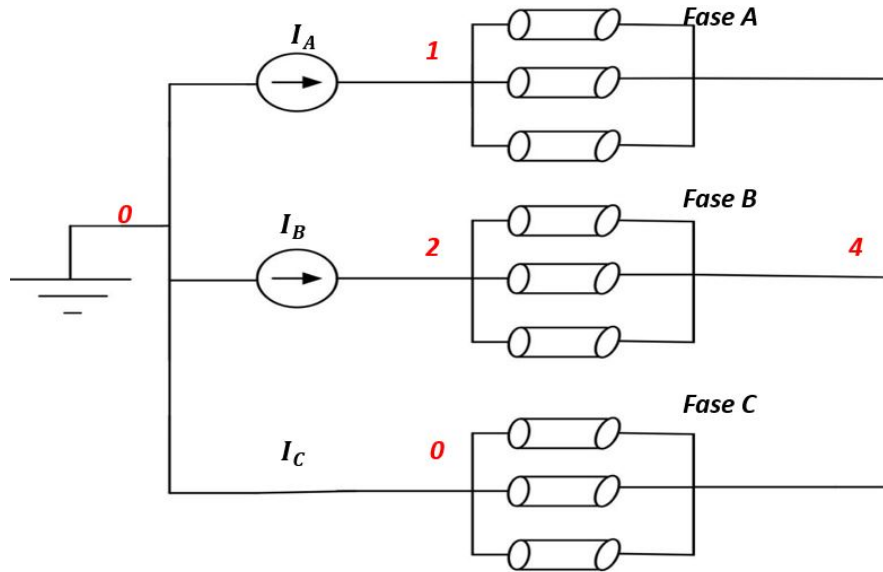


Figure A.3: Electrical circuit implemented in Comsol.

The accuracy that can be obtained from any FEM model is strongly related to the mesh that is used. The mesh is used to subdivide the CAD model into smaller domains called elements over which a set of equations are solved. The refinement process is an important **Trade-Off** between the accuracy of the finite element model, and the computational time required for having the solution. There are several possibilities for reducing the computational time while keeping an acceptable accuracy, all discussed in [36].

In the following pictures (A.4, A.5) a sketch of the used mesh is presented:

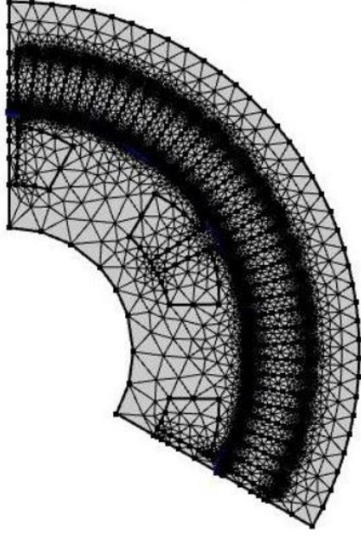


Figure A.4: Mesh on one pole pair of the machine.

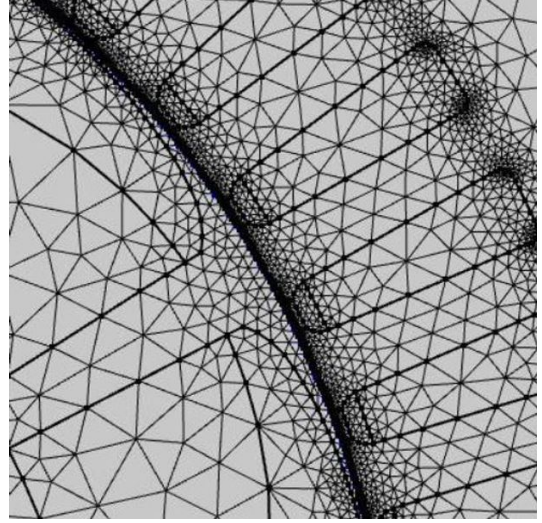


Figure A.5: Detail of the mesh in the air-gap.

A.3 Results Validation

To be sure about the simulation of the machine, a comparison between the results obtained through Comsol and the results from the software Flux was necessary, indeed as already mentioned, the thesis work [43] has already demonstrated the validity of the Flux results concerning the experimental ones provided by the company. In this section, the match will be pursued regarding the following parameters:

- Magnetic flux density distribution to the air-gap;
- No-load characteristics;
- Average electromagnetic torque;

Before showing the results, it must be known that the simulation is validated when at least three working points are checked. In the following table the point of interest are shown:

	Wp1	Wp2	Wp3
$I_d[A]$	0	0	0
$I_q[A]$	246	636	636
$I_{exc}[A]$	1	2	3.5
$T_{average}$	110	225	350

Table A.4: Working points suggested by the company to calibrate the FEM model [43].

A.3.1 No-Load Simulation

To start, a magnetostatic simulation is performed, with an excitation current of 1 A, 843 turns in the rotor. The magnetic flux density map in comsol is the following:

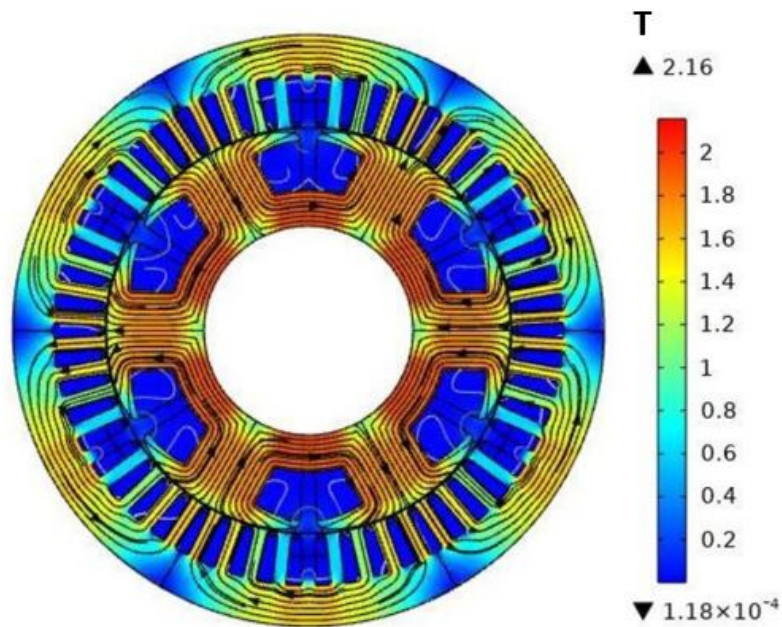


Figure A.6: Magnetic Flux Density Map from Comsol.

The searched magnetic flux density at the air-gap was 1.1 T as a peak value and 0.9 T as 1° harmonic, in the following graph, a comparison between the results obtained from the different software with different levels of discretization is shown. As seen in figure A.7 there is an optimal match between the two software, moreover, in this initial stage, the difference with linear and quadratic discretization is not significant.

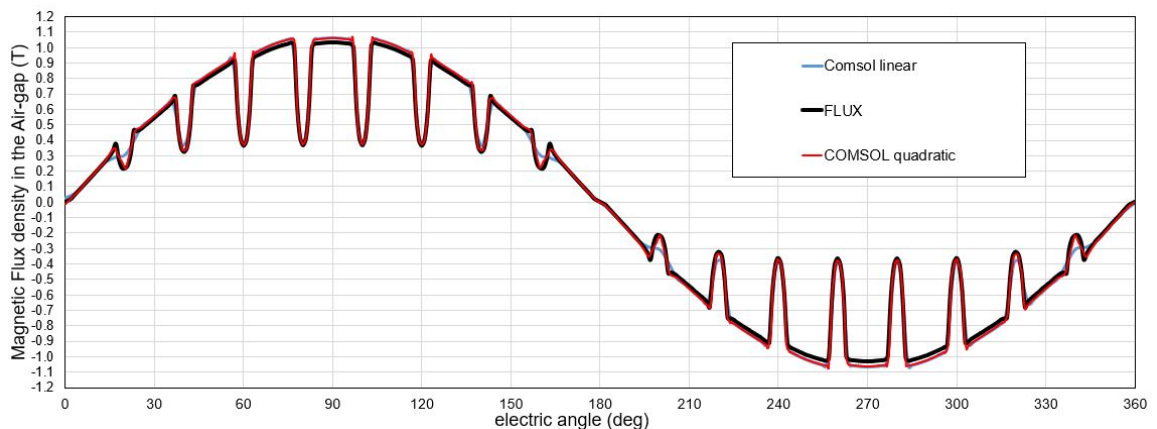


Figure A.7: Comparison between Magnetic Flux Density distribution to the Air-Gap

The next step on the validation is to check the no-load phase voltage with a rotational speed of 2000 rpm.

For a complete check of the no-load simulation, a parametric sweep in Comsol is performed. The field excitation current is changed in a range from 0 to 1.6 A with a step of 0.1 A. For each value of excitation current, the peak value of the voltage is registered and compared with the reference value provided by the company. In this way, it is possible to build the *No-Load Characteristics* of the machine.

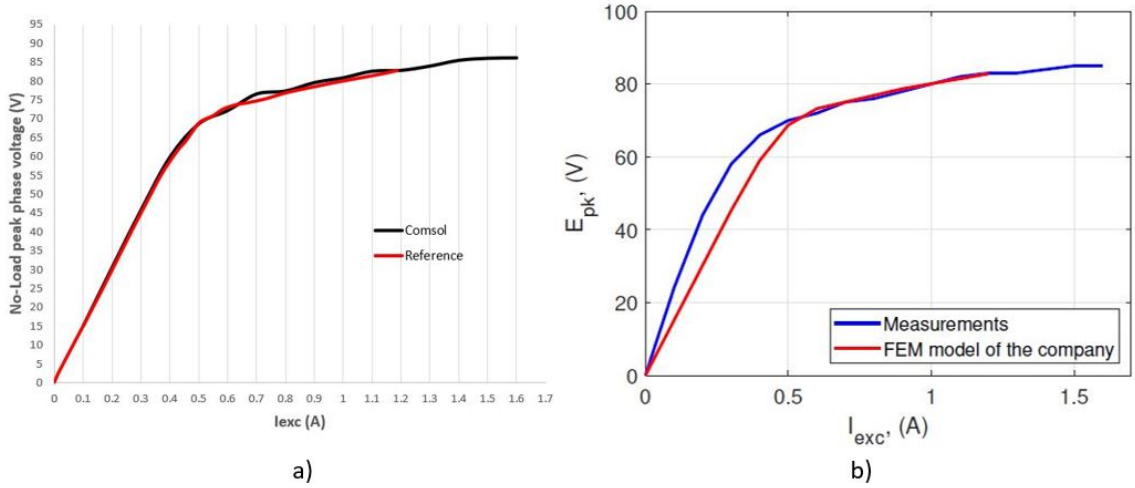


Figure A.8: Fig.a) No-Load characteristics comparison between Comsol and flux; Fig.b) No-Load Characteristics comparison between Flux and experimental results [44].

where E_{pk} is the peak value of the no-load voltage measured with different excitation currents.

A.3.2 Simulation at Load

For the simulation at load, it is necessary to explain in detail which is the working point in which the results are registered and compared.

The compared working point are three, they are provided by the company and they are all with a value of the current in the direct axis equals to zero, as shown in figure A.9

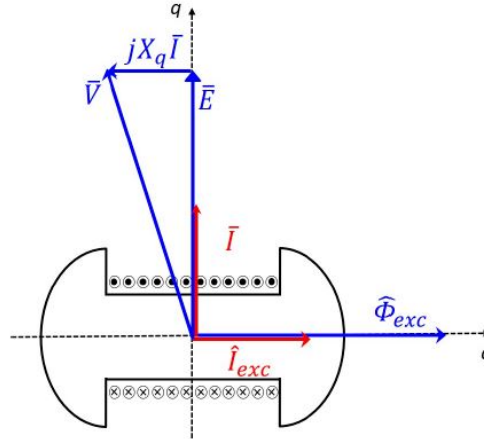


Figure A.9: Electrical circuit implemented in Comsol [43].

The same operating conditions ($I_d = 0$) are repeated for the three working point. To remember:

	Wp1	Wp2	Wp3
$I_d[A]$	0	0	0
$I_q[A]$	246	636	636
$I_{exc}[A]$	1	2	3.5
$T_{average}$	110	225	350

Table A.5: Working points suggested by the company to calibrate the FEM model [43].

Where $T_{average}$ is the average torque over a mechanical period, I_{ecc} is the excitation current for each winding in the rotor, and $(I_d; I_q)$ are respectively the direct and quadratic axis current.

In the simulation at load, the matches of interest are the magnetic flux density map and the mean electromagnetic torque over a mechanical period.

In figures A.10 a comparison of the magnetic flux density map for the WP2 is presented:

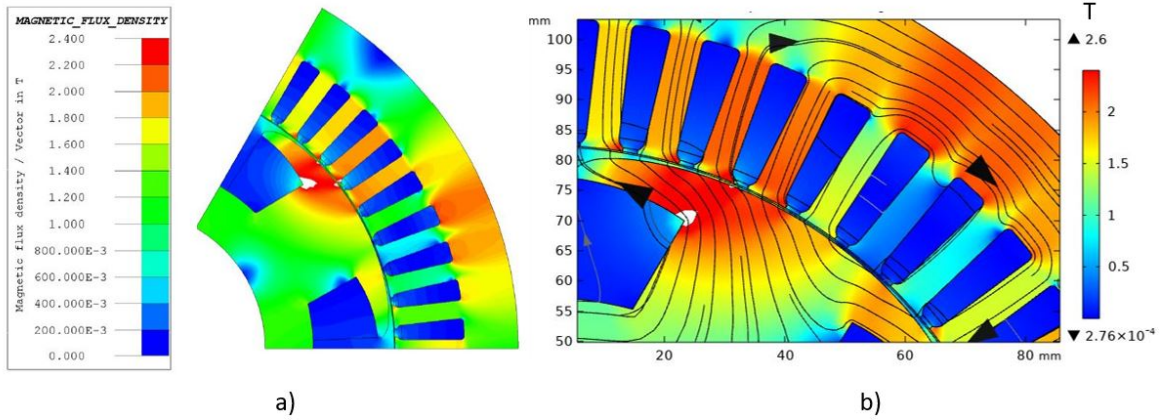


Figure A.10: Fig. a) Magnetic Flux Density Map for WP2 simulated with flux [43]; Fig. b) Magnetic Flux Density Map for WP2 simulated with Comsol.

From the picture "b" above it is possible to note a general truth in EM simulation, the flux lines through the rotor are "distorted" in the direction of the rotational speed (anticlockwise), this means that the synchronous machine is working as a motor, accordingly to the theory [44].

Lastly, let's take a look at the electromagnetic torque. The different curves of the electromagnetic torque of figure A.11 are related to different types of the mesh in Comsol, and the one from Flux:

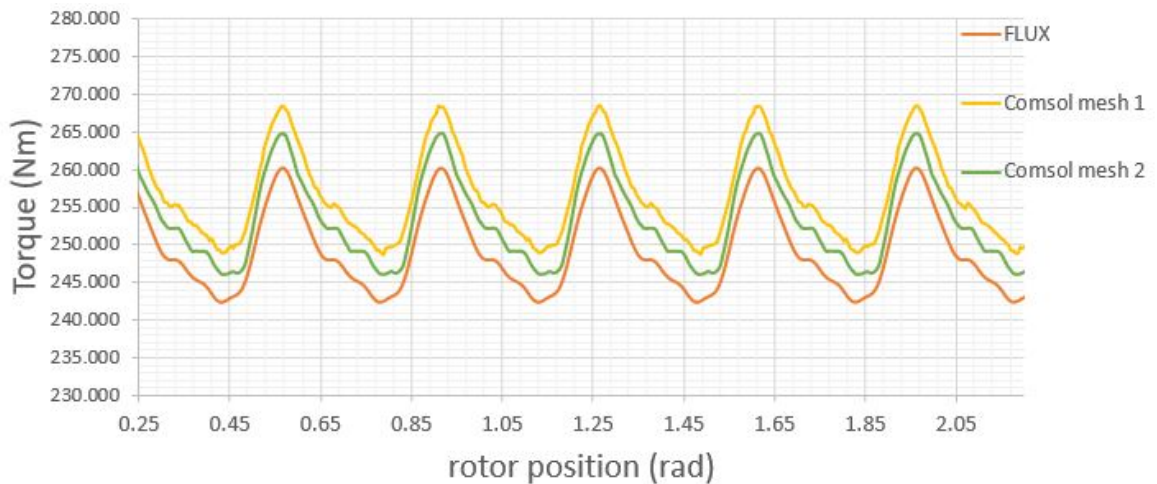


Figure A.11: Torque comparison between Flux and Comsol with different size and discretization of the mesh.

The same situation repeat itself with the other two working point, summarized in table A.6:

I_{ecc} [A]	Iq [A]	T_{ref}	T_{FLux}	T_{Comsol}
1	246	110	112.4	110.53
2	636	225	253.6	250.1
3.5	636	350	367.9	372.64

Table A.6: Torque Comparison between Comsol, Flux and experimental results.

Where T_{ref} is the reference torque provided by the company, T_{Flux} is the reference value from flux simulation [43], and T_{Comsol} is the average torque obtained from Comsol.

In light of these results, the validation of the Comsol simulation of an EM is completed. This was a crucial point for this thesis work, it allows us to feel confident about the values obtained from further simulations. Therefore, the validity of the results provided by software simulation will be assumed.

Appendix B

10 MW Wind Turbine HTS Generator

The aim of this section is to replicate the results and the simulations of the design of a 10 MW wind turbine generator from [37], in order to prove the validity of the design approach proposed in chapter 4, and to check the match between the theoretical formulas and the results from the Comsol simulation. According to [37], in the following tables, the main specifications and geometrical characteristics of the generator are shown:

Parameter	Value
Output Power [MW]	10
pole number	8
Rated Line Voltage [kV]	3.3
Rated Shaft speed [rpm]	10

Table B.1: Basic Design parameters of HTS Wind-Turbine Synchronous Generator [37].

The main geometrical dimensions and arrangements parameters are:

Parameter	Value
Stator windings Magnetic Flux density [T]	3
Electrical Loading [kA/m]	350
Winding factor	0.9531
External Parallel	2
Stator slot number per pole per phase	3.5
Stator lot number per phase	36
N°of stator windings turn per phase	252
Stator mean winding radius[mm]	1094
Stator back yoke inner radius[mm]	1250
Rotor field windings radius[mm]	897
Generator Lengthmm	1800
Total HTS winding FMM [Am]	13.523×10^6

Table B.2: Physical Dimensions and design parameters [37].

B.1 Magnetostatics

In fig B.1 is shown the comparison between the magnetic flux density map obtained through the utilization of the design formulas in section 4.2.2 and the one shown in [37]. As it is possible to see, there is a good match between the two maps. These results confirm that the method explained in chapter 4, is actually the same used in [37].

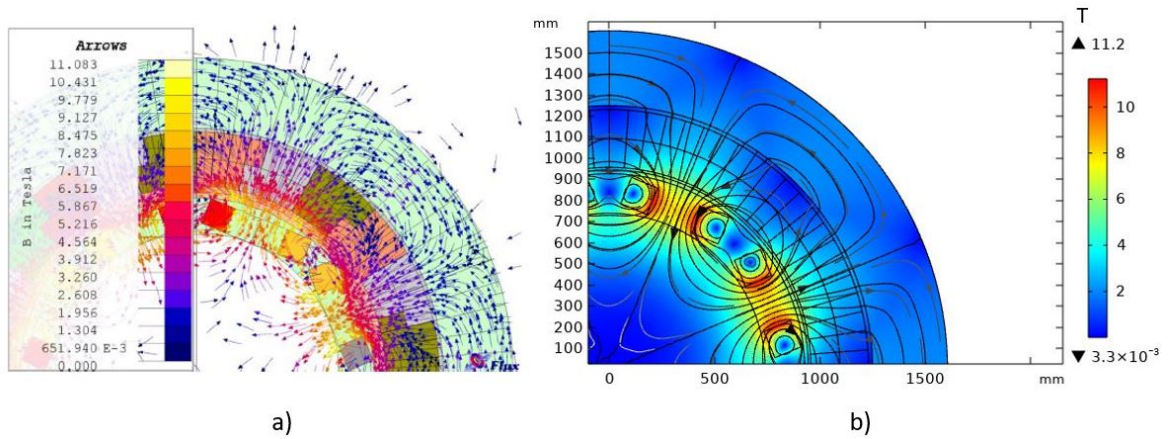


Figure B.1: Fig. a) Magnetic flux density distribution from [37] ; Fig. b) Magnetic Flux density distribution obtained through design formulas 4.2.2

However, the most important comparison for the magnetostatic, is the magnetic flux density distribution at armature stator windings and the value of its fundamental. In figure 4.21 a comparison between the radial component of the magnetic flux density at the stator windings is shown:

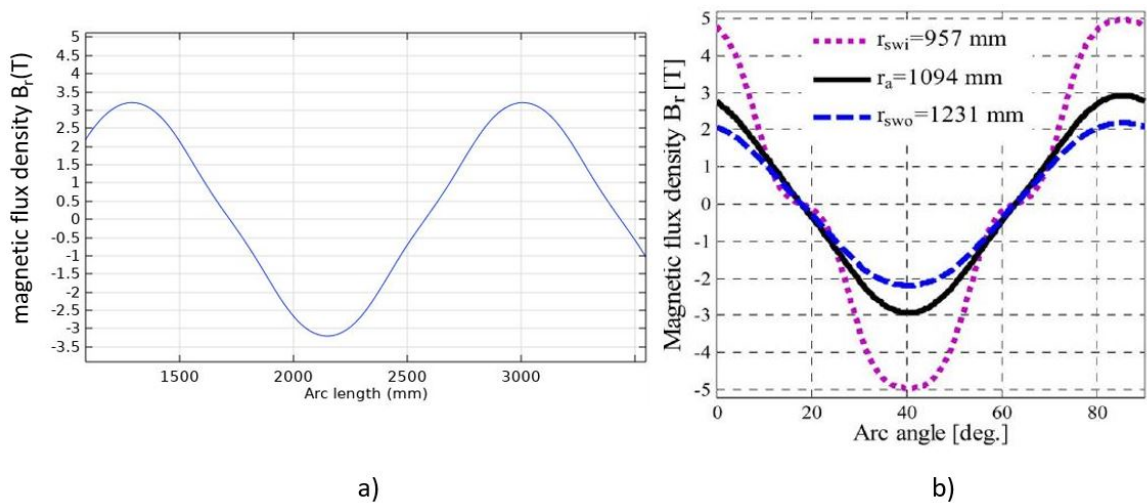


Figure B.2: Fig. a) Magnetic Flux distribution at mean armature stator windings radius from Comsol; Fig. b) Magnetic FLux density distribution from [37].

The fundamental value obtained from Comsol in B.2 a is 3.01 T while a value of 2.8209 T was indicated in [37], so in figure B.2 b). A difference of 6% was considered very good in terms of both goodness of the results given by the formulas and for the match with their design in [37]. Moreover, there is to note the excellent match between the desired value of magnetic flux density, and the one obtained through equation 4.14, expressed below to remember:

$$N_f I_f = \frac{\pi r_f B_{s0}}{\mu_0 \left(\frac{r_f}{r_a}\right)^{p+1} \left[1 + \left(\frac{r_a}{r_{s1}}\right)^{2p}\right]} \quad (\text{B.1})$$

B.2 No-Load phase voltage

The same procedure can be applied with the no-load phase voltage. A rotational speed of 10 rpm was implemented and, according to the equation B.2:

$$\sqrt{2}E_0 = n_c 2\pi n_s k_w D B_{s0} L q p / a = 3040V \quad (\text{B.2})$$

A fundamental value of 3178 was obtained applying FFT to figure B.3. A good match with their value of voltage was obtained, and a difference from the theoretical indication and the simulated one lower than 10% was consider very good for the purpose.

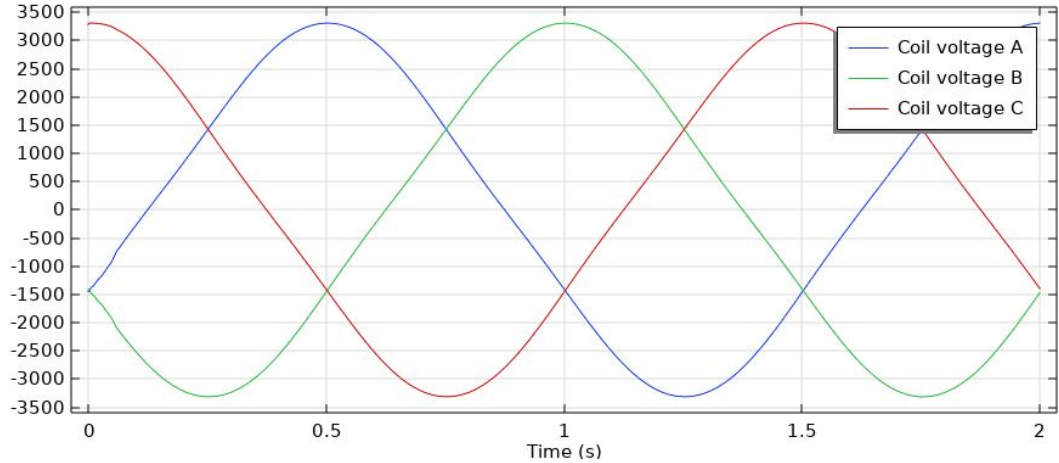


Figure B.3: No-Load phase Induced Voltage obtained with Comsol Multiphysics 4.2.2.

B.3 Load Simulation

At this point, the check with the wind turbine results proposed in [37] is assumed to be completed. One last check is needed, or rather the match between the torque indicated by comsol, and the one obtained through the Sizing equation. This point is crucial, indeed, one of the most important differences between air-core and the conventional machine is the place where the electromagnetic conversion takes place. In a conventional machine, this place is the air gap, and it is very well defined by the layer of air between the stator and rotor part, but in the air-core type, this place is not very well defined. On the basis of the results obtained, and according to [39], it

is possible to predict the value of the electromagnetic torque applying the theoretical Sizing equation on the mean radius of the armature windings.

The armature current to implement in consol in order to replicate the same operating condition of the wind turbine is obtained through the electromagnetic power formula:

$$\hat{I}_A = \frac{2P_G}{3\hat{E}_{0f}} = 2100A \quad (\text{B.3})$$

Implementing this current, a mean torque of $T_m = -9.554719 \times 10^6$ (figure B.4) was obtained, this is consistent with the fact that the machine is working as a generator.

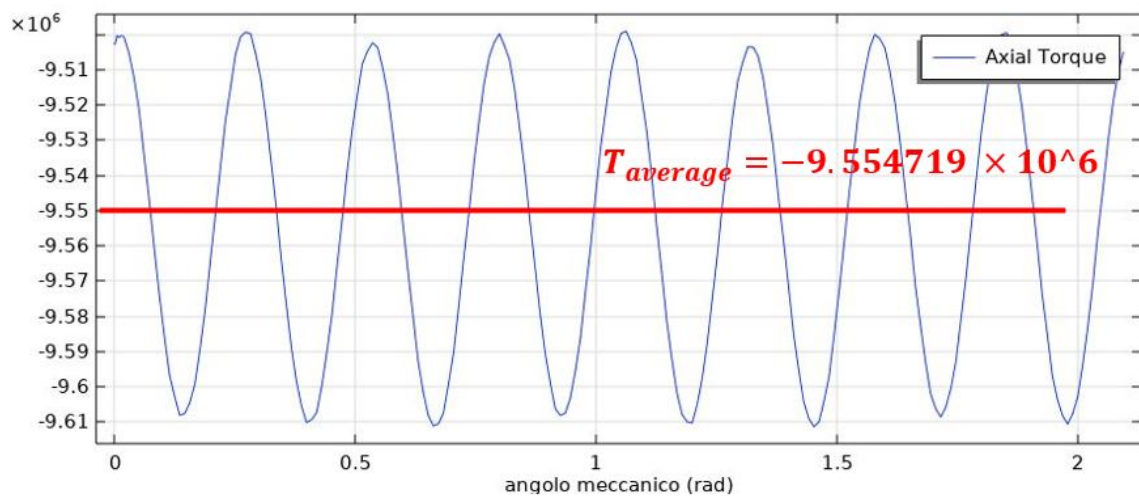


Figure B.4: Electromagnetic torque evaluated from Comsol

It should be noted that this average torque value was obtained by selecting the rotor as the surface on which to calculate the torque through the node "Force calculation" in Comsol, as shown in figure B.5:

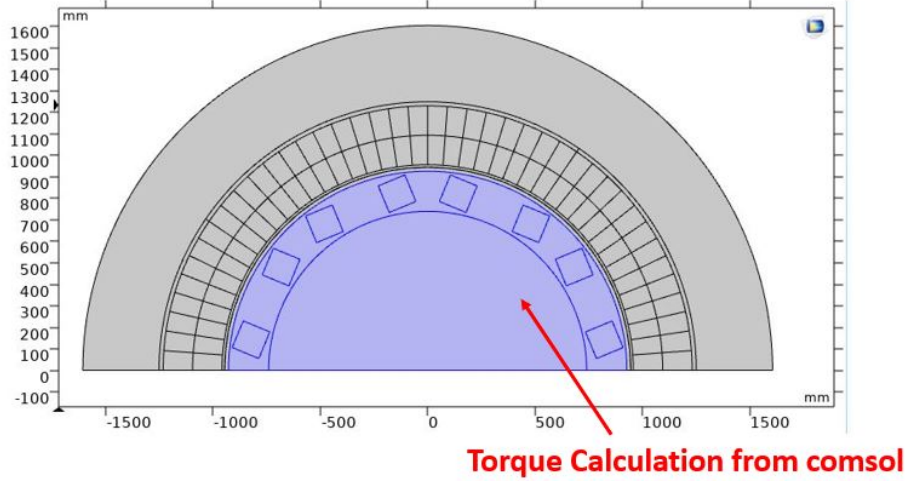


Figure B.5: Rotor Surface that has been selected for the Torque evaluation.

Lastly, the torque evaluated from the Sizing equation applied to the mean armature windings radius is:

$$T_G = \frac{\pi}{2\sqrt{2}} K_w B_{s0} A_s D^2 L = 9.857855 \times 10^6 Nm \quad (B.4)$$

In table (B.3), a summary of the theoretical torque and the one calculated through Comsol is presented:

Theoretical Torque [Nm]	Comsol Torque [Nm]	Percentage error %
-9.857855×10^6	-9.554719×10^6	3

Table B.3: Torque Comparison obtained through Comsol and from theoretical Sizing equation.

In conclusion, with this brief comparison, the goodness of the match between design formulas and the Comsol results was completed, in particular, an error of 3% between the theoretical value and the one calculated with Comsol was obtained. Moreover, thanks to the reduced harmonic content of the air-core machine, a ripple of $\approx 2\%$ was deduced from figure B.4. Thanks to this procedure, the design approach can be considered validated.

Bibliography

- [1] Mykhaylo Filipenko et al. “Concept design of a high power superconducting generator for future hybrid-electric aircraft”. In: *Superconductor Science and Technology* 33.5 (Mar. 2020), p. 054002. DOI: 10.1088/1361-6668/ab695a. URL: <https://doi.org/10.1088/1361-6668/ab695a>.
- [2] Commissione europea, Direzione generale della Mobilità e dei trasporti, and Direzione generale della Ricerca e dell’innovazione. *Flightpath 2050 : Europe’s vision for aviation : maintaining global leadership and serving society’s needs*. Publications Office, 2012. DOI: doi/10.2777/15458.
- [3] Matthias Corduan et al. “Topology Comparison of Superconducting AC Machines for Hybrid Electric Aircraft”. In: *IEEE Transactions on Applied Superconductivity* 30.2 (2020), pp. 1–10. DOI: 10.1109/TASC.2019.2963396.
- [4] Konstantin Kovalev, Julia Nekrasova, Nickolay Ivanov, and Sergey Zhurzhevlev. “Design of All-Superconducting Electrical Motor for Full Electric Aircraft”. In: *2019 International Conference on Electrotechnical Complexes and Systems (ICOECS)*. 2019, pp. 1–5. DOI: 10.1109/ICOECS46375.2019.8949952.
- [5] Nateri Madavan, R Del Rosario, and A Jankovsky. “Hybrid-electric and distributed propulsion technologies for large commercial air transports: a NASA perspective”. In: *Special Session on Future Electric Aircraft-Systems IEEE ECCE (2015)*, pp. 20–24.
- [6] Amy Jankovsky, Cheryl Bowman, and Ralph Jansen. “Building blocks for transport-class hybrid and turboelectric vehicles”. In: *Electric & Hybrid Aerospace Technology Symposium, Cologne, Germany (November 2016)*. 2016.
- [7] Clinton Rodrigo. *Basic Comparison of Three Aircraft Concepts: Classic Jet Propulsion, Turbo-Electric Propulsion and Turbo-Hydraulic Propulsion*. Version V1. 2020. DOI: 10.7910/DVN/K5FLHR. URL: <https://doi.org/10.7910/DVN/K5FLHR>.
- [8] Marco Biasion, João F. P. Fernandes, Silvio Vaschetto, Andrea Cavagnino, and Alberto Tenconi. “Superconductivity and its Application in the Field of Electrical Machines”. In: *2021 IEEE International Electric Machines Drives Conference (IEMDC)*. 2021, pp. 1–7. DOI: 10.1109/IEMDC47953.2021.9449545.
- [9] Jacek Gieras. “Superconducting Electrical Machines State of the Art”. In: *Przegląd Elektrotechniczny* 85 (Dec. 2009), pp. 1–19.
- [10] Bruce Gamble, Greg Snitchler, and Tim MacDonald. “Full Power Test of a 36.5 MW HTS Propulsion Motor”. In: *IEEE Transactions on Applied Superconductivity* 21.3 (2011), pp. 1083–1088. DOI: 10.1109/TASC.2010.2093854.

BIBLIOGRAPHY

- [11] Ehab Sayed et al. “Review of Electric Machines in More-/Hybrid-/Turbo-Electric Aircraft”. In: *IEEE Transactions on Transportation Electrification* 7.4 (2021), pp. 2976–3005. DOI: 10.1109/TTE.2021.3089605.
- [12] S. Fukui et al. “Analysis of AC loss characteristics of high temperature superconducting coil”. In: *IEEE Transactions on Applied Superconductivity* 15.2 (2005), pp. 1566–1569. DOI: 10.1109/TASC.2005.849173.
- [13] G. Snitchler, B. Gamble, and S.S. Kalsi. “The performance of a 5 MW high temperature superconductor ship propulsion motor”. In: *IEEE Transactions on Applied Superconductivity* 15.2 (2005), pp. 2206–2209. DOI: 10.1109/TASC.2005.849613.
- [14] Swarn Kalsi. *Applications of High Temperature Superconductors to Electric Power Equipment*. Apr. 2011. ISBN: 978-0-470-16768-7. DOI: 10.1002/9780470877890.ch11.
- [15] Jules Edward Pienkos. *Cooling, thermal design, and stability of a superconducting motor*. The Florida State University, 2009.
- [16] K. Sivasubramaniam et al. “Development of a High Speed HTS Generator for Airborne Applications”. In: *IEEE Transactions on Applied Superconductivity* 19.3 (2009), pp. 1656–1661. DOI: 10.1109/TASC.2009.2017758.
- [17] A Colle, Thierry Lubin, Sabrina Ayat, O. Gosselin, and Jean L ev eque. “Test of a Flux Modulation Superconducting Machine for Aircraft”. In: *Journal of Physics: Conference Series* 1590 (July 2020), p. 012052. DOI: 10.1088/1742-6596/1590/1/012052.
- [18] Sydney L. Schnulo et al. “Assessment of the Impact of an Advanced Power System on a Turboelectric Single-Aisle Concept Aircraft”. In: *2020 AIAA/IEEE Electric Aircraft Technologies Symposium (EATS)*. 2020, pp. 1–18.
- [19] David C. Jiles. “Introduction to Magnetism and Magnetic Materials”. In: 2015.
- [20] Liangliang Wei, Taketsune Nakamura, Masaaki Yoshikawa, Yoshitaka Itoh, and Toshihisa Terazawa. “Comparison of Different Stator Winding Configurations of Fully High-Temperature Superconducting Induction/Synchronous Motor”. In: *IEEE Transactions on Applied Superconductivity* 30.4 (2020), pp. 1–4. DOI: 10.1109/TASC.2020.2985687.
- [21] T. Coombs. “4 - Bulk high temperature superconductor (HTS) materials”. In: *High Temperature Superconductors (HTS) for Energy Applications*. Ed. by Ziad Melhem. Woodhead Publishing Series in Energy. Woodhead Publishing, 2012, pp. 101–139. ISBN: 978-0-85709-012-6. DOI: <https://doi.org/10.1533/9780857095299.1.101>. URL: <https://www.sciencedirect.com/science/article/pii/B9780857090126500042>.
- [22] Fangjing Weng. “Fully high temperature superconducting (HTS) machine for future electric aircraft”. PhD thesis. University of Strathclyde, 2021.
- [23] Valeria Braccini, Davide Nardelli, Roberto Penco, and Giovanni Grasso. “Development of ex situ processed MgB2 wires and their applications to magnets”. In: *Physica C: Superconductivity* 456.1-2 (2007), pp. 209–217.

BIBLIOGRAPHY

- [24] L.J. Masur, J. Kellers, Feng Li, S. Fleshler, and E.R. Podtburg. “Industrial high temperature superconductors: perspectives and milestones”. In: *IEEE Transactions on Applied Superconductivity* 12.1 (2002), pp. 1145–1150. DOI: 10.1109/TASC.2002.1018604.
- [25] Seung-Kyu Baik and Gwan-Soo Park. “Load Test Analysis of High-Temperature Superconducting Synchronous Motors”. In: *IEEE Transactions on Applied Superconductivity* 26.4 (2016), pp. 1–4. DOI: 10.1109/TASC.2016.2530662.
- [26] A. Molodyk et al. “Development and large volume production of extremely high current density YBa₂Cu₃O₇ superconducting wires for fusion”. In: *Scientific Reports* 11 (Jan. 2021). DOI: 10.1038/s41598-021-81559-z.
- [27] *ASG Superconductors index*. <https://www.asgsuperconductors.com/>.
- [28] Frédéric Sirois, Francesco Grilli, and Antonio Morandi. “Comparison of Constitutive Laws for Modeling High-Temperature Superconductors”. In: *IEEE Transactions on Applied Superconductivity* 29.1 (2019), pp. 1–10. DOI: 10.1109/TASC.2018.2848219.
- [29] Roberto Brambilla, Francesco Grilli, Luciano Martini, Marco Bocchi, and Giuliano Angeli. “A Finite-Element Method Framework for Modeling Rotating Machines With Superconducting Windings”. In: *IEEE Transactions on Applied Superconductivity* 28.5 (2018), pp. 1–11. DOI: 10.1109/TASC.2018.2812884.
- [30] Francesco Grilli. “Numerical Modeling of HTS Applications”. In: *IEEE Transactions on Applied Superconductivity* 26.3 (2016), pp. 1–8. DOI: 10.1109/TASC.2016.2520083.
- [31] Yufan Yan, Timing Qu, and Francesco Grilli. “Numerical Modeling of AC Loss in HTS Coated Conductors and Roebel Cable Using T-A Formulation and Comparison With H Formulation”. In: *IEEE Access* 9 (2021), pp. 49649–49659. DOI: 10.1109/ACCESS.2021.3067037.
- [32] *HTS Motor School*. [https://htsmotors.sciencesconf.org/..](https://htsmotors.sciencesconf.org/)
- [33] Edgar Berrospe-Juarez, Victor M R Zermeño, Frederic Trillaud, and Francesco Grilli. “Real-time simulation of large-scale HTS systems: multi-scale and homogeneous models using the T–A formulation”. In: *Superconductor Science and Technology* 32.6 (Apr. 2019), p. 065003. DOI: 10.1088/1361-6668/ab0d66. URL: <https://doi.org/10.1088/1361-6668/ab0d66>.
- [34] Yawei Wang, Hongyu Bai, Jianwei Li, Min Zhang, and weijia Yuan. “Electromagnetic modeling using T-A formulation for high temperature superconductor (RE)Ba₂Cu₃O_x high field magnets”. In: *High Voltage* 5 (Jan. 2020). DOI: 10.1049/hve.2019.0120.
- [35] Gunar Klaus, Markus Wilke, Joachim Fraunhofer, Wolfgang Nick, and Heinz-Werner Neumuller. “Design Challenges and Benefits of HTS Synchronous Machines”. In: *2007 IEEE Power Engineering Society General Meeting*. 2007, pp. 1–8. DOI: 10.1109/PES.2007.385756.
- [36] Juha Pyrhonen, Tapani Jokinen, and Valeria Hrabovcova. *Design of rotating electrical machines*. John Wiley & Sons, 2013.

BIBLIOGRAPHY

- [37] Rouhollah Shafaie and Mohsen Kalantar. “Design of a 10-MW-Class Wind Turbine HTS Synchronous Generator With Optimized Field Winding”. In: *IEEE Transactions on Applied Superconductivity* 23.4 (2013), pp. 5202307–5202307. DOI: 10.1109/TASC.2013.2256421.
- [38] A. Hughes and T. J. E. Miller. “Analysis of fields and inductances in air-cored and iron-cored synchronous machines”. In: *Proceedings of the Institution of Electrical Engineers* 124.2 (1977), pp. 121–126.
- [39] T. Miller and A. Hughes. “Comparative design and performance analysis of air-cored and iron-cored synchronous machines”. In: *Proceedings of The Institution of Electrical Engineers* 124 (Feb. 1977). DOI: 10.1049/piee.1977.0022.
- [40] Luning Hao, Zhen Huang, Fangliang Dong, Derong Qiu, and Zuquan Jin. “Performance Comparison and Applicability Analysis of Different Armature Structures for a Small-Scale HTS Linear Synchronous Motor”. In: *IEEE Transactions on Applied Superconductivity* PP (Nov. 2018), pp. 1–1. DOI: 10.1109/TASC.2018.2881673.
- [41] Satoshi Fukui et al. “Study of 10 MW-Class Wind Turbine Synchronous Generators With HTS Field Windings”. In: *IEEE Transactions on Applied Superconductivity* 21.3 (2011), pp. 1151–1154. DOI: 10.1109/TASC.2010.2090115.
- [42] Rouhollah Shafaie, Fatemeh Amirkhanloo, and Mohsen Kalantar. “Toward an Optimum Design of Large-Scale HTS Synchronous Generator for Wind Turbine Applications”. In: *IEEE Transactions on Applied Superconductivity* 26.2 (2016), pp. 1–8. DOI: 10.1109/TASC.2016.2519416.
- [43] Federica GRAFFEO, Silvio VASHETTO, Andrea CAVAGNINO, Edson Da Costa BORTONI, and Marco COSSALE. “Design and analysis of different rotor configurations for wound field synchronous machines”. In: ().
- [44] Enzo Michele Illiano. “Design of a highly efficient brushless current excited synchronous motor for automotive purposes”. PhD thesis. ETH Zurich, 2014.